High-Order Resonant Power Converters for Battery Charger Applications

by

Navid Shafiei

B.Sc., Kashan University, Iran, 2005
M.Sc., Islamic Azad University, NajafAbad Branch, Iran, 2011

A THESIS SUBMITTED IN PARTIAL FULFILLMENT OF
THE REQUIREMENTS FOR THE DEGREE OF

DOCTOR OF PHILOSOPHY

in

The Faculty of Graduate and Postdoctoral Studies

(Electrical & Computer Engineering)

THE UNIVERSITY OF BRITISH COLUMBIA

(Vancouver)

April 2017

Abstract

The demand for electric vehicles has expanded rapidly for both industrial and transportation applications. In parallel, new battery technologies have been introduced which are capable of deep-discharge and powering electric vehicles for long periods of time. Due to the increasing complexity of charging algorithms, battery chargers are exposed to demanding operating requirements. In battery charger applications, power converters should not only regulate the battery voltage and power over a wide range, all the way from complete discharge up to the charged floating voltage, but also respond to the input voltage variation period. It is also important to work at high efficiency and with low switching noise and charging current ripple.

This work studies different problems regarding DC-DC power converters with wide voltage regulation as battery chargers, and investigates the application of novel high-order resonant power converters (fourth and fifth-order) and modulation strategies at various power levels. As a solution for high power applications, this work first introduces a modified full bridge LLC resonant power converter driven by both variable frequency and phase shift modulation. The proposed modulation strategy along with the modified resonant circuit exhibits excellent performance for a $3kW$ resonant power converter, without taking advantage of burst mode strategy. The second part of this work introduces a novel fifth-order $L3C2$ resonant converter for medium power level applications, that can regulate the battery voltage from near zero output voltage, zero output current to maximum output power. A $950W$ design example demonstrates a wide output voltage regulation with maximum efficiency of 96%. Finally,

a fourth order $L3C$ resonant converter is proposed for electric vehicles with roof-top solar photovoltaic panels, which can not only regulate the battery voltage in a wide range, but also track the input voltage variation for extracting the maximum available power from the PV panel. All results from this work have been confirmed experimentally, which highlight the exceptional regulation capability of the proposed resonant power converters and modulation techniques.

Preface

This work is based on research performed at the Department of Electrical and Computer Engineering of the University of British Columbia by Navid Shafiei, under the supervision of Dr. Martin Ordonez.

Chapter 1 contains modified portions of text from all below-listed publications.

Portions of Chapter 2 have been published at the IEEE Energy Conversion Congress and Expo (ECCE) and in the IEEE Transactions on Power Electronics [1, 2]:

- N. Shafiei, M. Ordonez, M. Craciun, M. Edington, and C. Botting, "High power *LLC* battery charger: wide regulation using phase-shift for recovery mode," in *IEEE Energy Conversion Congress and Exposition (ECCE)*, 2014, pp. 2037-2042.

- N. Shafiei, M. Ordonez, M. Craciun, C. Botting, and M. Edington, "Burst mode elimination in high-power *LLC* resonant battery charger for electric vehicles," *IEEE Transactions on Power Electronics*, vol. 31, no. 2, pp. 1173-1188, Feb. 2016.

Portions of Chapter 3 have been published at the IEEE Applied Power Electronics Conference and Exposition (APEC) and in the IEEE Transactions on Power Electronics [3, 4]:

- N. Shafiei, M. Ordonez, W. Eberle, "Output rectifier analysis in parallel and series-parallel resonant converters with pure capacitive output filter," in *IEEE Applied Power Electronics Conference and Exposition (APEC)*, 2014, pp. 9-13.

- N. Shafiei, M. Ordonez, "Improving the regulation range of EV battery chargers with *L3C2* resonant converters," *IEEE Transactions on Power Electronics*, vol. 30, no. 6,

pp. 3166-3184, June 2015.

Portions of Chapter 4 have been published at the IEEE Applied Power Electronics Conference and Exposition (APEC) [5]:

- N. Shafiei, M. Ordonez, C. Botting, M. Craciun, and M. Edington, "Fourth order *L3C* resonant converter for wide output voltage regulation," in *IEEE Applied Power Electronics Conference and Exposition (APEC)*, 2015, pp. 1467-1471.

Two papers related to work in progress, described in Chapter 5 have been published at IEEE Energy Conversion Congress and Expo (ECCE) and IEEE Applied Power Electronics Conference and Exposition (APEC) [6, 7]:

- N. Shafiei, M. Ordonez, S. R. Cove, M. Craciun, and C. Botting, "Accurate modeling and design of *LLC* resonant converter with planar transformers," in *IEEE Energy Conversion Congress and Expo (ECCE)*, 2015, pp. 5468-5473.

- N. Shafiei; S. A. Arefifar, M. A. Saket, and M. Ordonez, "High efficiency *LLC* converter design for universal battery chargers," in *IEEE Applied Power Electronics Conference and Exposition (APEC)*, 2016, pp. 2561-2566.

As first author of the above-mentioned publications, the author of this thesis developed the theoretical concepts and wrote the manuscripts, developed simulation and experimental platforms, and received advice and technical support from Dr. Martin Ordonez and his research team, in particular from Dr. Samuel Robert Cove who contributed to the specific optimization algorithm for resonant power converter design. Also, the author received advice and technical support for the practical side of Power Electronics Development (prototyping) from Delta-Q Technologies engineers (Marian Craciun, Chris Botting, and Murray Edington).

Table of Contents

List of Tables

List of Figures

Nomenclature

C_j	Diode junction capacitance (F).
C_n	Resonant capacitance ratio ($C_n = C_t/C_s$).
C_p	Parallel resonant capacitance (F).
C_s	Series resonant capacitance (F).
C_t	Equivalent parallel resonant capacitance (F).
$C_{w,s}$	Winding capacitance of the transformer secondary side (F).
f_0	Resonant frequency (Hz).
f_r	Resonant frequency for specific loading condition (Hz).
$f_{r,oc}$	Open circuit resonant frequency (Hz).
$f_{r,oc1}$	First open circuit resonant frequency (Hz).
$f_{r,oc2}$	Second open circuit resonant frequency (Hz).
$f_{r,sc}$	Short circuit resonant frequency (Hz).
f_s	Switching frequency (Hz).
G	Solar irradiation at the ambient temperature (kW/m^2).
$I_{L_{s_1}}$	Peak current of the first series resonant inductance (A).
$I_{L_{s_2}}$	Peak current of the second series resonant inductance (A).
I_{bat}	DC output current (A).
k	Boltzmann constant ($k = 1.3806503 \times 10^{23} J/K$).
L_{ext}	External series inductance (H).
$L_{lk,p}$	Transformer primary leakage inductance (H).

$L_{lk,s}$	Transformer secondary leakage inductance (H).
L_m	Transformer magnetizing inductance (H).
L_n	Resonant inductance ratio ($L_n = L_{s1}/L_p$).
L_p	Parallel resonant inductance (H).
L_s	Series resonant inductance ratio ($L_s = L_{s1}/L_{s2}$).
L_{s_1}	First series resonant inductance (H).
L_{s_2}	Second series resonant inductance (H).
M_{V_r}	AC-AC voltage transfer function due to the 1st harmonic.
M_{V_R}	AC-DC voltage transfer function of the current driven rectifier.
M_{V_s}	DC-AC voltage transfer function of the full bridge inverter.
n	Transformer turns ratio ($n = N_p/N_s$).
q	Electronic charge ($q = 1.602 \times 10^{-19} C$)
Q_L	Loaded quality factor.
R'_{bat}	Battery equivalent resistance (Ω).
R_L	Load resistance (Ω).
T	Photovoltaic panel cell temperature (Kelvin).
V_{AB_1}	1^{st} harmonic of the full bridge inverter.
$V_{R_{eq}}$	Output voltage amplitude of the LLC resonant inverter.
V_{in}	DC input voltage (V).
V_{bat}	DC output voltage (V).
V_{Req}	Output voltage amplitude of the LLC resonant inverter.
Z_0	Series characteristic impedance (Ω).

Acknowledgements

I would like to sincerely thank my supervisor Dr. Martin Ordonez for accepting me as part of his research team. His support, dedication and technical advice during my program is greatly appreciated.

I would also like to acknowledge our research team, for graciously sharing their experience and knowledge with me, and for making these years a series of enjoyable experiences. Special thanks go to Dr. Samuel Robert Cove for developing Design of Experiment Methodology (DoE) in resonant power converters optimization.

A special thank-you is extended to Delta-Q Technologies for their collaboration with UBC, which allowed me to further develop my research ideas while experiencing the practical side of electronics development.

Finally, it is my pleasure to be able to thank my wife, Marjan, for her incredible patience, constant understanding, and unwavering support throughout the entirety of this process.

Chapter 1

Introduction[1]

1.1 Motivation

In the past decade, the use of electric vehicles (EVs) has increased rapidly, creating a tangible alternative to offset greenhouse gas emissions. Also, mounting photovoltaic (PV) panels on the roofs of electric vehicles (EVs) is an exciting new opportunity to extend the range and reduce the charge time of EVs during daylight [8–16]. EVs are propelled by electric motors, which are powered by rechargeable batteries as the source of energy. Fig. 1.1(a) presents a pure EV with a power cord and roof-top PV panel as possible input energy sources. Also, Fig. 1.1(b) shows the general power conditioning block diagram of the pure EV, which includes a Power Factor Correction (PFC) along with an isolated DC-DC power converter from a universal AC input source to the battery pack, and another isolated DC-DC power converter from the PV source to the battery pack. DC-DC Power converters are among the most important parts of EVs, which need to get the power from input DC buses (either PFC circuit, or PV panel output) , and store it in a rechargeable battery pack. There are different types of rechargeable battery packs on the market (Li-Ion, Lead-Acid, NiMH, etc.) which are used for energy storage in EVs [17–23]. Using batteries for energy storage imposes challenging design constraints for chargers, due to the different operating modes of the battery, including constant current, constant voltage, constant power, no-load condition,

[1]Portions of this chapter have been modified from [1–7]

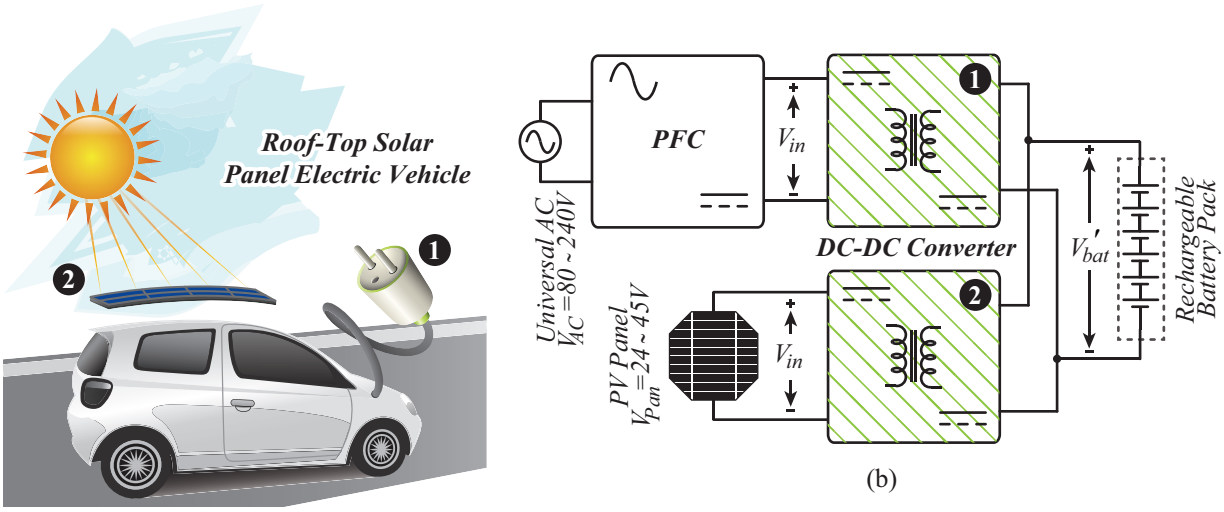

Figure 1.1: (a) Pure Electric Vehicle with roof-top PV panel with possible input sources (① indicates the main input source of EV from AC source outlet, and ② indicates the power from a solar PV panel, which can provide up to several hundred watts (e.g. $400W$) power.), (b) the general block diagram of battery chargers, which are employed to transfer the power from two input sources to a rechargeable battery pack in a pure EV with a roof-top PV panel.

and revitalization. According to Fig. 1.2(a), the Lead-Acid battery charging profile includes three main phases: Bulk (max charging current), Absorption (constant voltage), and Finish (a limited current to offset the internal soft discharge). During the Bulk phase, the battery is less than fully charged and the maximum charging current is provided while monitoring the battery voltage. In the Absorption mode, the charger increases the battery voltage to Absorption voltage, which is typically specified by the battery manufacturer. At this point, the battery has been charged to between 70% and 90% of its capacity and the remainder is filled with the slower topping charge that occurs during Absorption phase. Under certain circumstances, voltage cells in a battery pack can be different (out of balance). In this case, an overcharge mode is performed to equalize the voltage of the cells in a battery pack. According to Fig. 1.2(a), the most difficult charging cycle occurs when the battery pack has

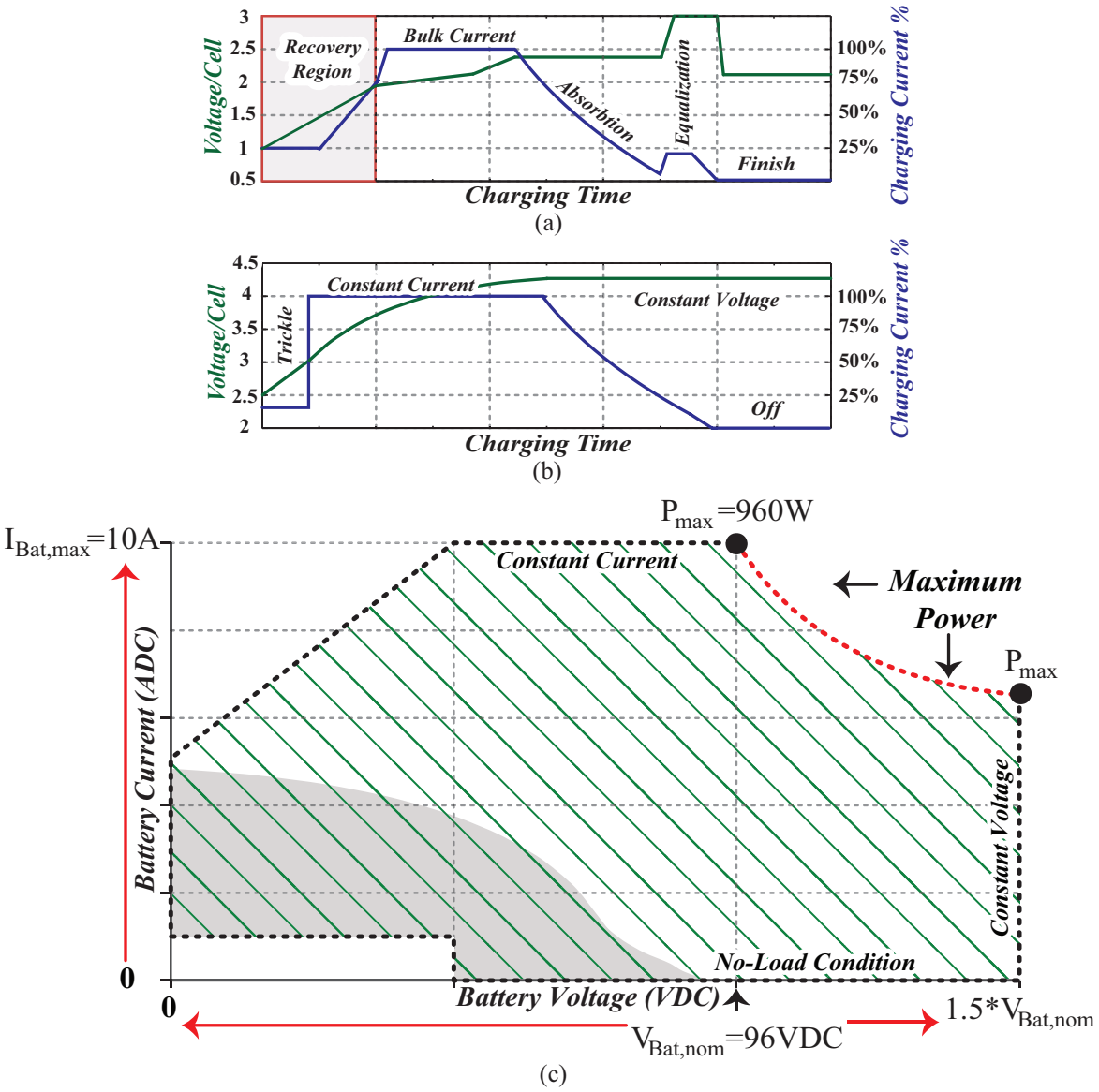

Figure 1.2: (a) Charging cycle profile for a single Lead-Acid battery including Recovery Region, (b) Charging cycle profile for a single Lithium-Ion battery cell, (c) Desired V-I plane for a universal battery charger (e.g. $960W$ battery charger). The gray area highlights V-I plane regulation issues of current state-of-the art technologies.

been discharged completely owing to either over-discharging or extended storage time. In this situation, the voltage of the battery pack drops into the dead-zone, close to zero volts per cell (Recovery Region) [21, 24–26]. Fig. 1.2(b) shows that the Li-Ion battery has two different modes in its charging profile, which are constant current and constant voltage mode. During

constant current operation, the voltage of each cell is near its maximum (around 4V/cell) and therefore the battery charger is working around its maximum output power. In the constant voltage stage, the cell voltage are maintained at the maximum until the charging current gradually declines below a set threshold of the maximum current. Moreover, a trickle charging stage before the constant current stage is necessary for deeply depleted cells [27–30]. For the industrial-grade charger manufacturing, it is preferable to design and fabricate universal battery chargers to support different types of batteries. Combining the charging profiles presented in Fig. 1.2(a) and (b) leads to a general V-I plane, presented in Fig. 1.2(c) that is essential to consider in a universal battery charger design [31, 32]. According to Fig. 1.2(c), the battery charger should not only work in different load conditions, from absolutely zero to maximum output current, but also regulate the output voltage from near zero up to 1.5 times the nominal voltage. Moreover, the DC-DC stage related to the PV panel needs to track the input voltage variation to get maximum power from the PV panel.

This work will review critical problems for extreme regulation that have been observed in existing battery chargers. For an extreme regulation, chargers should not only work under different loading conditions (from absolutely zero to maximum output current) but also regulate a wide output voltage range (from near zero to 1.5 times nominal voltage). Fig. 1.2(c) presents an example of output voltage-current plane, which has to be supported by a battery charger. According to Fig. 1.2(c), the nominal output voltage and current are $96VDC$ and $10ADC$, and depending on the state of charge, the charger has to regulate the battery voltage from near zero to 144VDC (far beyond its normal operating condition). In this work, different problems regarding the current state-of-the art topologies for DC-DC power converters are studied in detail, including soft switching (defined in Appendix B) restriction in the PWM full bridge topology, the parasitic capacitance drawback on the voltage gain of the LLC resonant converter, and burst mode modulation issues for the extreme regulation. The current state-of-the art topologies are not able to regulate the output in a low voltage

and current range (represented by the gray area in Fig. 1.2(c)) in the continuous conduction mode so the burst mode strategy is applied for extreme regulation, which leads to a high ripple charging current. Fig. 1.3 illustrates the principle operation of the burst mode along with main waveforms of the full bridge converter. According to Fig. 1.3, in burst mode, the gate signals are turned on and off periodically with an intermittent cycle much lower than the converter switching frequency(several kHz as the burst frequency in comparison with several hundred kHz for the power converter). In fact, the converter operates in discontinuous conduction mode and transfers pockets of energy to the output side.

The contribution of this work is based on novel DC-DC resonant converter topologies and

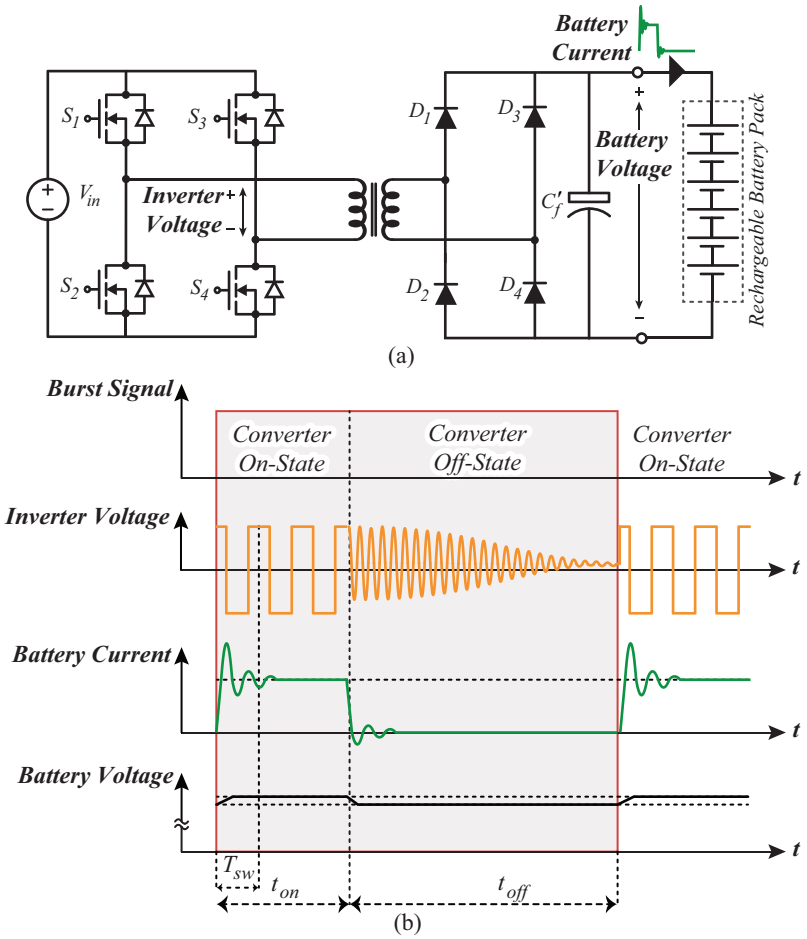

Figure 1.3: (a)The full bridge converter, and (b) the burst mode principle of operation.

modulation methods that are capable of extreme regulation and responding to various states of battery charge (all points in the V-I plane presented in Fig. 1.2(c)). The objective is to propose new battery charger topologies (including modified LLC, $L3C2$, $L3C$) that operate with high efficiency, high power density and smooth charging current, while transferring energy from fixed or variable DC sources to different battery technologies (e.g. Li-Ion, Lead-Acid, NiMH). This work proposes a modified fourth-order resonant power converter with new modulation strategies and a novel fifth order resonant converter as new resonant circuit topologies, applicable for battery chargers at high and medium power level applications with fixed DC input voltage (indicated by ① in Fig. 1.1(b)). Also, a fourth order resonant converter is introduced as a solution for variable input voltage to battery packs, used for EVs with a roof-top solar PV panel (indicated by ② in Fig. 1.1(b)). The proposed solutions will be investigated theoretically and implemented experimentally in order to prove the accuracy of the analysis and their performance in battery charger applications.

1.2 Literature Review

There has been interesting research into improving the performance of EVs battery chargers, and it is an active topic in power electronics research today. Common research goals include how to modify different power converter topologies for wide regulation, or using new modulation strategies at extreme output regulation with the best achievable efficiency. The following cited work has been performed in the field of DC-DC power conversion for battery charging and PV applications, organized by fixed and variable input voltage.

1.2.1 Fixed Input Voltage DC-DC Power Converter

According to Fig. 1.1(b), there are two different power converters from a universal input source ($v_{AC} = 80 - 240VRMS$) to battery pack, including a Power Factor Correction (PFC)

circuit and a DC-DC power converter. The PFC circuit is a vital part in the architecture of a power conditioning circuit, since it gets a sinusoidal current from the main and eliminates low frequency DC voltage ripple without using a bulky capacitor filter, and produces an almost fixed DC bus voltage (e.g. $V_{in} = 400VDC$) [33–36]. The DC-DC power converter is the next stage, which is responsible for regulating the battery voltage over a wide range and responding to various states of battery charge. The combination of PFC and DC-DC power converter is used as the main path for charging the battery pack, when an AC power source is available (① in Fig. 1.1(b)). What follows is a list of relevant literature organized by topology type (PWM and resonant converters) and type of regulation strategy (Burst Mode) for wide regulation.

Pulse Width Modulation DC-DC Power Converters

Among Pulse Width Modulation topologies, Phase Shift Full Bridge (PSFB) power converters have attracted more attention than other topologies (e.g. half bridge, push pull, forward) for battery charger applications, due to their capability to provide soft switching conditions for semiconductor devices over a wide range of loading conditions. Also, due to the fixed frequency operation of PSFB power converters, the design procedure is straight forward without any complications. The main reported concerns about the PSFB topology have been ensuring soft-switching operation at light and no-load condition, rectifier voltage peak reduction, and output voltage regulation extension. The conventional PSFB can regulate the output voltage widely by increasing the phase shift between two legs (leading and lagging legs), but a PSFB loses the Zero Voltage Switching (ZVS) condition at light loads and wide output voltage regulation [37–42]. Several approaches for the PSFB, including symmetric passive auxiliary circuit, hybrid converters, fixed-variable duty cycle, and self-sustained oscillating control, have been studied in order to extend the output voltage regulation, while provide soft switching condition for semi-conductor elements [43–45]. However, extreme regulation

(regulating the output voltage from zero to 1.5 times of its nominal), which is essential for battery recovery has not yet been studied for PSFB. Voltage peaks across the output rectifier diodes is another problem encountered by the conventional PSFB converter and as a result, diodes with higher blocking voltage have to be selected which leads to more conduction losses and lower efficiency. Different techniques such as L-C circuits, RCD networks, and active rectifiers have been presented for the PSFB in order to eliminate the voltage peak across the output rectifier diodes, but resolving the negative impact on the efficiency and reducing the number of active and passive circuits still remain as research opportunities [28, 46, 47]. Generally, soft commutation of the output rectifier leads to better selection of the rectifier diodes, higher efficiency, lower EMI, and higher switching frequency operation.

Resonant Power Converters with Variable Frequency

Resonant power converters are candidates for the design of battery chargers, due to their capability to produce variable voltage gains in different operating frequencies [48–51]. Also, resonant topologies offer the potential of achieving soft switching for semiconductor devices and the possibility of increasing the switching frequency, which leads to a smaller, lighter, and less costly system. The concept of the soft switching in resonant converters is presented in Appendix C. Resonant power converters can be employed from low to high power level applications. Among resonant converter topologies, the *LLC* topology has become a popular resonant converter featuring many advantages such as Zero Voltage and Zero Current Switching (ZVZCS), and the absorption of the transformer parasitics (leakage and magnetizing inductances) as resonant elements [52, 52–63]. Theoretically, it is possible to decrease the output voltage of the *LLC* resonant converter by increasing the switching frequency in the inductive region (higher than short circuit resonant frequency). However, the existence of parasitic capacitances (diode junction, transformer secondary side, and PCB layers) leads to an undesired oscillation in the secondary side of the transformer and a second resonant

frequency occurs in the voltage gain curves, which is far from the short circuit resonant frequency [4, 25, 26, 64]. As a result, it is not possible to decrease the output voltage by increasing the switching frequency and, therefore, a maximum switching frequency is assigned for the converter. After the maximum switching frequency, the voltage gain at no-load or light-load conditions increases as the switching frequency increases, causing reverse polarity of the feedback signal and turning negative feedback into positive feedback. This problem is usually dealt with using a dummy load in the output of the converter. However, in battery charger applications, employing dummy loads in the output leads to lower efficiency and battery discharge, which is not acceptable.

Employing Burst Mode Strategy for Wide Regulation

In order to expand the output voltage regulation for battery charger applications, a discontinuous charging mode called burst mode is applied either in PWM or resonant converters. In this method, the switching driver signals are turned on and off periodically at an intermittent cycle much lower than the converter switching frequency (several kHz in comparison with several hundred kHz). Generally, burst mode strategy is employed in light and no-load conditions in order to improve the efficiency and provide extreme voltage regulation and has proven successful for LED applications [65, 66]. There are several issues as a result of using this strategy for battery charger applications, such as losing soft switching conditions, introducing high frequency voltage oscillations, and causing battery current ripple and spikes. Based on the continuous conduction mode (CCM) and burst mode operation technique (combined variable frequency, $150-450kHz$, fixed on time and fixed frequency variable on time), an LLC resonant converter was designed and implemented as a Lead-Acid battery charger [31, 32]. Although employing burst mode leads to better regulation, the interaction between parasitics capacitances (including MOSFET Drain-Source and diodes junction) and the resonant circuit elements leads to high frequency oscillation during converter off-state and

produces high EMI noise, which has a negative effect on the Battery Management System (responsible to provide output voltage and current set points according to battery state of charge), and leads to an unwanted tripping in recovery mode, interfering with the sensing and feedback circuit. Moreover, burst current ripple and ripple in general can affect the battery life cycle. In other words, the cleaner the charging current, the longer the battery's lifespan.

1.2.2 Variable Input Voltage DC-DC Power Converter

As shown in Fig. 1.1(a), considering a single panel on the rooftop of an EV, the maximum power capacity is up to several hundred watts, and depending on the solar irradiance and temperature variation, the Maximum Power Point (MPP) voltage range will change in a wide range. In this case, on top of wide output voltage regulation and battery state-of-charge response, the input voltage variation needs to be tracked to get maximum power from the PV panel. In the following, a list of related literature for low power PV applications (e.g. $400W$) is presented and organized by non-isolated and isolated topology type.

Non-Isolated DC-DC Power Converters for PV Applications

Recently, different studies have been dedicated to developing reliable and efficient non-isolated power converters for PV applications. Different topologies including buck and boost converter, Cockcraft-Walton multiplier, coupled inductors, switched inductors-capacitors and Z-converter with capability of high voltage gain have been introduced as the DC-DC systems for PV to grid applications (boosts a low, variable input voltage of $30 - 50VDC$ to a high, fixed output voltage of $380VDC$) [67–76]. Realizing a high voltage gain along with soft switching are the most important criteria for PV applications. The main considerations of the mentioned non-isolated boost converters are how to boost the input voltage for PV applications and realizing soft-switching for semiconductor devices. Other important requirements include current ripple reduction and voltage stress elimination. Although non-isolated

power converters can boost the PV voltage and reach high performance, they are not recommended for automotive applications due to a lack of galvanic isolation. According to safety standards No. $UL60950$ and $UL1741$, in order to prevent any high voltage shock path from battery pack to PV panel, one of the key features of power converters used in automotive applications is to have at least $4kV$ galvanic isolation between PV panel and high voltage battery pack, which dictates using an isolated transformer in the battery charger [77, 78].

Isolated DC-DC Power Converters for PV applications

Among isolated PWM power converter topologies, the most attention has been attracted by the following converter topologies: flyback, current fed push-pull, z-source converter, and full-bridge converters. These converters can achieve a high step-up gain from large transformer turn ratios while tracking the input voltage variation by changing the effective duty cycle [79–84]. Different improvements such as interleaving and active clamp circuit have been presented in order to decrease the input current ripple and transfer the maximum input power to the output with soft switching across the main switches [85–88]. These interesting converters described above target fixed output voltage, rather than the extreme regulation scenario of variable PV input voltage and variable battery output voltage. In particular, storage applications with new battery technologies (e.g., Li-ion) pushes the charger regulation requirement of the PV converter to unprecedented limits. Insightful research on resonant converters has been presented in the literature as a single stage or as a part of double stage approaches for either single-phase chargers or PV applications with fixed output voltage [52–55, 89–92]. Although all mentioned single stage or double stage resonant power converters can regulate the output voltage in a wide range or provide maximum power point tracking for PV applications, their applications for extreme regulation for both input and output sides still remain as research opportunities. The particular application addressed in this thesis involves the challenging scenario of extreme input and output voltage regulation from low

voltage PV ($V_{pv} = 24 - 45VDC$) to high variable charging voltage needed in battery packs ($V_{bat} = 230 - 430VDC$).

1.3 Contributions of the Work

The goal of this work is to introduce novel resonant power topologies and modulation strategies for battery charger applications. Three novel resonant power converters are proposed (modified LLC, $L3C2$, and $L3C$) with extreme output voltage capability which can not only respond to various states of battery charge (all points in the V-I plane presented in Fig. 1.2(c)), but also can operate in soft switching conditions which leads to a smaller, lighter, and less costly system. The proposed novel and original resonant power converters for battery charger applications are as follows:

- A modified full bridge LLC resonant converter is proposed for high power applications, which is a successful solution to achieve all the regulation requirements for battery charging in different states of charge. The proposed solution can eliminate the negative impact of burst mode on the Battery Management System, provide a ripple-free charging current for batteries in different states of charge, reduce the switching frequency variation, and facilitate the EMI filter and magnetic components designs procedure.

- Due to the popularity of employing half bridge inverters for medium power applications (cost effective in comparison with full bridge inverters), a multi-resonant $L3C2$ resonant converter is proposed that can cover nearly all of the regions in the battery V-I plane without employing the burst mode strategy. The topology is able to extend the operating frequency beyond the LLC topology and achieve significant regulation improvements. Near ripple-free charging current for battery charging is achieved in different states of charge, effectively increasing the battery life cycle. In addition, soft

transitions are obtained for all the switches (MOSFETs and diodes) resulting in high efficiency, reliability, power density, and low-noise operation of the charger.

- Because of extremely wide regulation requirements in solar battery charger applications, an original fourth-order $L3C$ resonant converter is proposed for EVs with roof-top PV panels which can not only regulate the output voltage in a wide range, but also track the input voltage variation for extracting the maximum available power from PV panels using switching frequency modulation. The proposed isolated $L3C$ resonant converter can provide soft transitions for all switches (MOSFETs and diodes). Moreover, due to the high-amplitude, high-frequency current in the primary side of the transformer, the elimination of the series resonant capacitor in the proposed topology facilitates the design and component selection.

In the area of DC-DC power converters for battery charger applications, this work makes great steps through the proposed high order resonant power topologies and modulation strategies for battery charger applications.

1.4 Dissertation Outline

This work is organized in the following manner:

- In Chapter 2, primary and secondary leakage inductances of the high frequency transformer are considered separately in order to examine the effect of secondary leakage inductance on the output voltage regulation of the LLC resonant converter. Next, a fixed-frequency Phase Shift (PS) approach is applied to a high power full-bridge topology, while the soft switching condition is studied. Using modified steady state equations, a $3kW$ power converter is designed and implemented for battery charger applications. The experimental results extracted from the power platform prove that

the proposed LLC tank and modulation strategy can effectively increase the range of output voltage regulation from no-load to full-load conditions without employing detrimental burst mode.

- In Chapter 3, a detailed analysis is presented to study and compare the $L3C2$ and LCC topology. The complete analysis of the $L3C2$ resonant converter with consideration of transformer primary and secondary leakage inductances, transformer secondary winding capacitance, and output rectifier junction capacitances is obtained. Using the analytical equations extracted from $L3C2$ and LLC resonant circuits, two power converters are designed, simulated, implemented, and compared as a $96VDC, 950W$ battery charger. The results prove the $L3C2$ resonant converter covers almost all regions in the V-I plane and can be employed as a wide voltage regulator for battery charger applications.

- In Chapter 4, the general equations for solar PV panels will be extracted and employed to determine the variation of power-voltage characteristics of a specific PV module versus irradiance and temperature variations. Then, the complete analysis of the $L3C$ resonant converter is obtained. Using the analytical equations extracted for fourth-order $L3C$ resonant circuits, a $350W$ DC-DC power converter is designed and implemented. Finally, experimental results are presented to demonstrate the circuit performance and to prove the feasibility of the converter. The results show the $L3C$ resonant converter can respond to all MPP, while regulating the output voltage in a wide range.

- Chapter 5 contains the relevant conclusions, contributions, and planned areas of future work. The work contributed significantly to the resonant power converter topologies for battery charger applications, which is highlighted in nine relevant publications in IEEE Transactions journals and international conferences papers.

Chapter 2

Burst Mode Elimination in High Power LLC Resonant Battery Chargers[2]

The softly-switched LLC resonant converter is one of the resonant topologies that has recently been employed for charger applications due to its ability to handle high power and produce variable voltage gains in different operating frequencies while providing soft switching for all semiconductor devices [27, 29, 55, 56, 66, 93–97]. Theoretically, this topology allows the output voltage to be decreased by increasing the switching frequency. However, the existence of parasitic capacitances (diode junction, transformer secondary side, and PCB layers) leads to undesired oscillation in the secondary side of the transformer and limits the maximum switching frequency [4, 25, 26, 64]. Fig. 2.1(a) presents the full bridge inverter based on MOSFET switches and the LLC resonant circuit schematic along with parasitic elements. Fig. 2.1(b) shows the normalized voltage gains of the LLC resonant converter compared to frequency, with and without consideration of the parasitic capacitance effect on the transformer secondary side. According to this figure, the capacitive effects on the secondary side of the transformer (diode junction, transformer secondary side, and PCB layers), are generally small so their impact is only observed in light and no-load conditions.

[2]Portions of this chapter have been published in [1, 2]

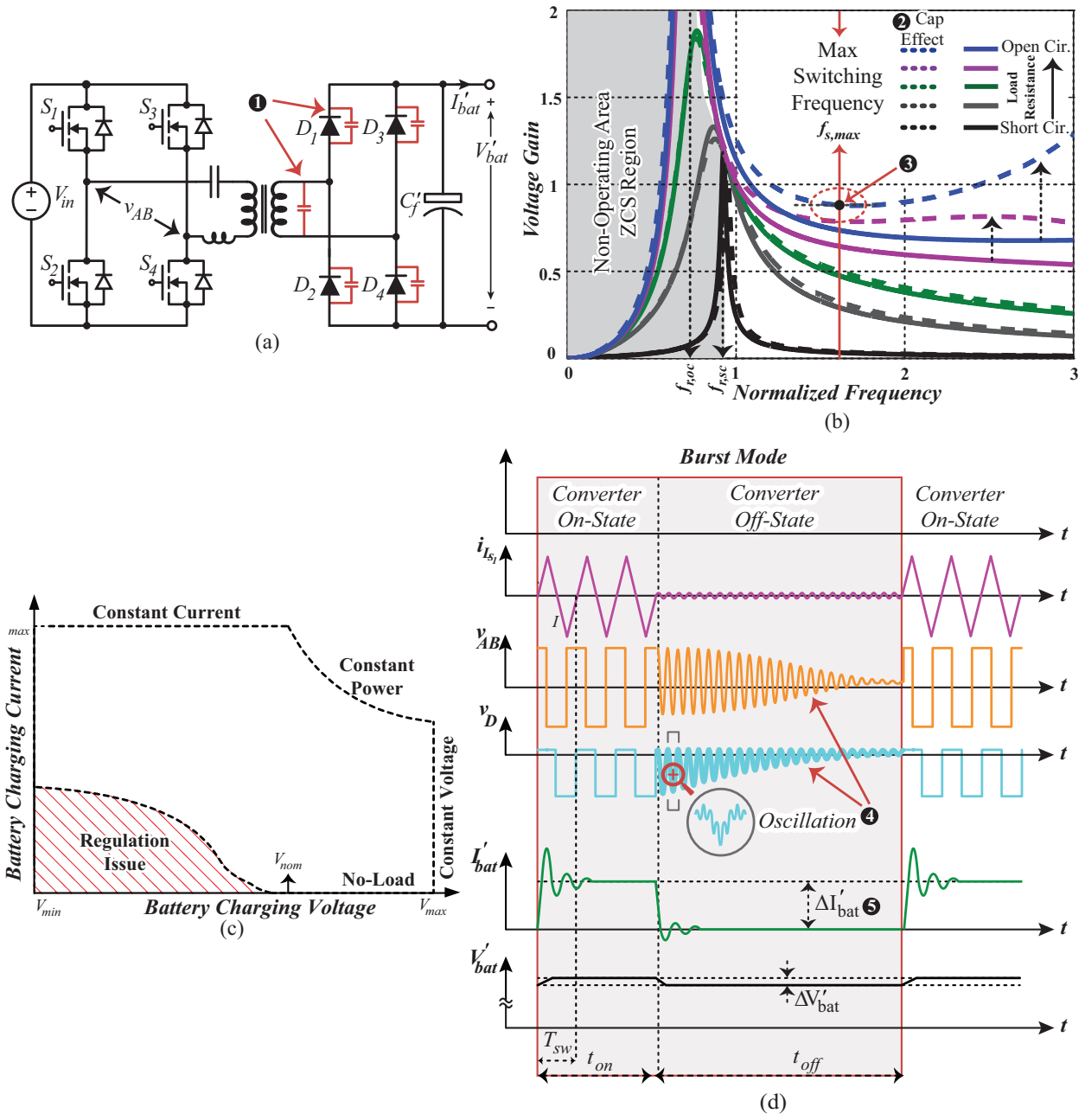

Figure 2.1: (a) Full bridge *LLC* resonant converter schematic and the parasitic capacitances ①, (b) The effect of the parasitics capacitors on the voltage gain curves ②, *LLC* voltage gain issues ③, (c) *LLC* V-I plane highlighting regulation issues, and (d) burst mode and its issues: High frequency oscillation due to the interaction between parasitic capacitances (MOSFET Drain-Source and diodes junction) and the resonant circuit ④, battery charging current ripple ⑤.

These parasitic capacitances lead to a second resonant frequency in the voltage gain curves, which is far from the short circuit resonant frequency ($f_{r,sc}$). In an ideal case, it is desirable to have the voltage gain presented by solid lines in Fig. 2.1(b), which leads to a negative slope for all voltage gains versus frequency (increasing the switching frequency leads to decreasing the output voltage); but, in the practice, after the maximum switching frequency, the voltage gain at no-load or light-load conditions (e.g. blue and purple curves) increases as the switching frequency increases, causing reverse polarity of the feedback signal and turning negative feedback into positive feedback. It means that after the maximum switching frequency labeled as $f_{s,max}$, the voltage gain at light-load and no-load conditions starts to increase. This problem is usually dealt with using a dummy load in the output of the converter. However, in battery charger applications, employing dummy loads in the output leads to the battery slowly discharging, which is not acceptable. Fig. 2.1(c) illustrates the maximum VI-plane coverage of the *LLC* resonant converter in continuous conduction mode [26]. The red dashed region in Fig. 2.1(c) indicates the unobtainable area in the V-I plane, where the switching frequency restriction leads to the regulation issue for the LLC resonant converter. In order to cover the red dashed region presented in Fig. 2.1(c), the burst mode strategy can be employed [65, 66]. Generally, a burst mode strategy is employed in light and no-load conditions in order to provide wide output voltage regulation and has proven successful for LED applications. Fig. 2.1(d) illustrates the principle operation of burst mode along with resonant converter waveforms. According to this figure, in burst mode, the gate signals are turned-on and off periodically with an intermittent cycle much lower than the converter switching frequency. In fact, the converter operates in discontinuous conduction mode, and transfers pockets of energy to the output side. Although employing burst mode leads to better regulation, the interaction between parasitics capacitances (including MOSFET Drain-Source and diodes junction) and the resonant circuit elements leads to high frequency oscillations during converter off-state and produces high EMI noise, which has a negative effect on Battery Management Systems

and leads to unwanted tripping in recovery mode, interfering with the sensing and feedback circuit. Moreover, burst current ripple and ripple in general can affect the battery life cycle. In other words, the cleaner the charging current, the longer the battery's lifespan [25]. Fig. 2.1(d) shows the ripple and ringing issues introduced by burst operating mode in battery chargers.

In this chapter, a modified *LLC* resonant converter is investigated for extreme regulation. This resonant circuit driven by both Variable Frequency (VF) and Phase Shift (PS) proves to be a successful solution to achieve all the regulation requirements for high power battery charger applications (from recovery, bulk, equalization, to finish). In particular, the performance in the recovery region allows the elimination of burst mode, resulting in a significant practical advancement for high efficiency battery chargers. The proposed *LLC* tank and modulation strategy is applied to a high power full-bridge topology, which is able to regulate the output voltage from close to zero to 1.5 times the nominal output voltage under different output load conditions. The ability of the full bridge *LLC* resonant converter to operate with soft-switching transitions (in all operating regions) without employing burst mode operation, provides a noise free environment for all auxiliary circuits, and effectively increases the performance of the battery charger (providing charging current without any ripple or spike). Moreover, this converter provides almost ripple-free charging current in order to charge batteries in different states of charge, which can increase battery lifespan. Furthermore, the proposed modulation strategy leads to a limited switching frequency variation of the *LLC* resonant converter; as a result the selection of magnetic parts (including high frequency transformers, and resonant inductors), control circuit, and semiconductor devices are facilitated. In this chapter, the complete analysis of the *LLC* resonant converter with consideration of transformer primary and secondary leakage inductances is obtained. Next, Design of Experiment (DoE) is employed in order to optimize the design procedure of the battery charger [98]. Later, a complete set of simulation and experimental results, extracted

from a 3kW resonant converter is presented in order to show that the proposed LLC tank and modulation strategy can effectively increase the range of output voltage regulation from no-load to full-load conditions without employing detrimental burst mode.

2.1 Secondary Leakage Inductance Effect on Wide Regulation

The principle and operation modes of the LLC resonant converter with a non-ideal transformer have been discussed in many papers. Typically, the literature replaces the high frequency transformer with a second order model, which incorporates effective leakage inductance along with magnetizing inductance, and employs an AC equivalent circuit for steady state analysis [48, 99–102]. Due to the existence of leakage inductance not only in the primary side, but also in the secondary side, a virtual voltage gain should be introduced, which presents the effect of secondary leakage inductance on the LLC voltage gain [103, 104]. However, failing to consider the leakage inductance in the transformer's secondary side in the equivalent AC circuits, results in incorrect steady state equations for the input impedance phase and input resonant circuit current, which are essential for wide regulation, soft switching, and high efficiency power converter design procedure. In the following, primary and secondary leakage inductances of the transformer are considered separately in order to examine the effect of secondary leakage inductance on the output voltage regulation and obtain a more accurate steady-state analysis.

The complete schematic of the LLC resonant converter with a non-ideal transformer has been presented in Fig. 2.2. According to this figure, the non-ideal transformer has been replaced by a fourth order model equivalent circuit [105, 106]. The secondary leakage inductance and the magnetizing inductance of the transformer are considered L_{s_2} and L_p,

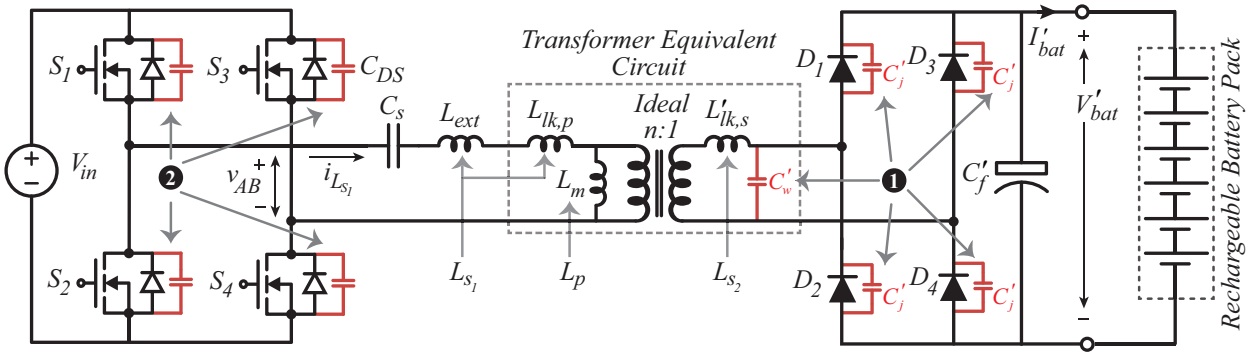

Figure 2.2: Full bridge *LLC* resonant converter schematic along with parasitic elements (including MOSFET Drain-Source capacitances, transformer elements, and output rectifier diodes junction capacitances). ① indicates that the parasitic capacitances in the secondary side of the circuit causes unwanted oscillation and the regulation issue for the *LLC* resonant converter. ② indicates MOSFETs Drain-Source effective capacitances that should be discharged completely during dead time intervals.

respectively. The primary leakage inductance is absorbed by the external resonant inductor and is a part of L_{s_1}. In this work the equivalent capacitor on the secondary side of the transformer (including diode junction, transformer secondary side, and PCB layers) has been estimated and measured to be around $300pF$ after selecting the output rectifier diodes and fabricating the transformer. For the output rectifier diodes, the capacitance is extracted from the data sheet, but for the transformer and PCB it is necessary to use the impedance analyzer and the RLC meter respectively. According to Fig. 2.1(b), this amount of equivalent parasitic capacitances can make a difference just in light and no-load conditions. Due to the designing the *LLC* resonant converter in nominal operating point (nominal output voltage and maximum output current), the effect of this parasitic capacitances is negligible and considering this parasitic capacitances in the steady state procedure just results in too complicated equations without any advantage. Also, the MOSFETs Drain-Source capacitances can only affect the inverter transient behaviour and does not participate in the resonant circuit steady state analysis. Fig. 2.3(a) demonstrates three main parts of the *LLC* resonant converter, namely, the full bridge inverter, resonant circuit, and output rectifier.

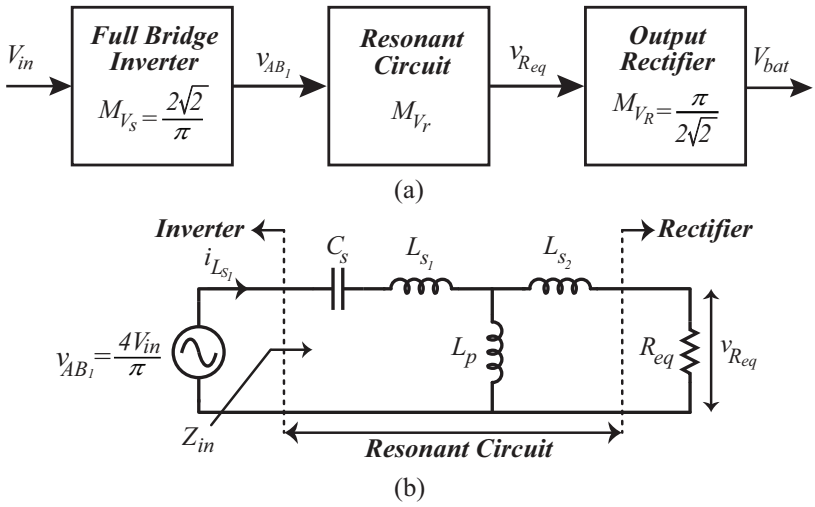

Figure 2.3: (a) The block diagram of the LLC Resonant converter with capacitive output filter, and (b) AC equivalent circuit of the modified LLC resonant converter.

Fig. 2.3(b) shows the AC equivalent circuit of the modified LLC resonant converter with separated primary and secondary leakage inductances. Note that other parasitic inductances in both primary and secondary side of the transformer are integrated in L_{s_1} and L_{s_2} (e.g. PCB traces, transformer connection, diodes pins). In this figure, the variables and elements are transferred to the primary side of the transformer (without an apostrophe). The steady-state analysis of the resonant converter can be carried out by using this AC equivalent circuit and First Harmonic Approximation (FHA) analysis [48]. According to Fig. 2.3(b), the input impedance of the resonant circuit is obtained as follows:

$$\mathbf{Z_{in}}(j\omega_s) = \frac{1}{j\omega_s C_s} + j\omega_s L_{s_1} + (j\omega_s L_p)||(j\omega_s L_{s_2} + R_{eq}) \tag{2.1}$$

The following normalized parameters are introduced for the resonant circuit.

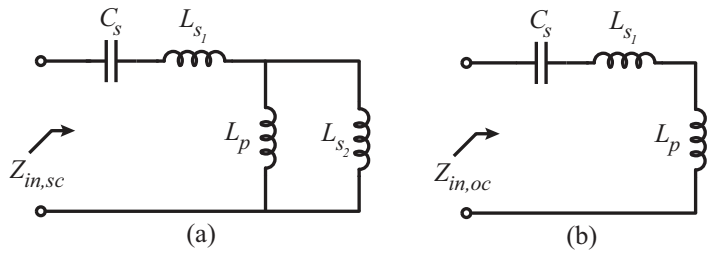

Figure 2.4: (a) The AC equivalent circuit in short circuit condition, (b) The AC equivalent circuit in open circuit condition.

$$\begin{aligned} &Q_L = \frac{R_L}{Z_0}, Z_0 = \sqrt{\frac{L_{s_1}}{C_s}}, \omega_0 = \frac{1}{\sqrt{L_{s_1} C_s}}, \\ &\omega_n = \frac{\omega_s}{\omega_0}, L_s = \frac{L_{s_1}}{L_{s_2}}, L_n = \frac{L_{s_1}}{L_p} \end{aligned} \tag{2.2}$$

Considering (2.1) and (2.2), the normalized input impedance can be expressed as:

$$\frac{\mathbf{Z_{in}}(j\omega_n)}{Z_0} = (j\omega_n + \frac{1}{j\omega_n}) + \frac{\frac{j\omega_n}{L_n}(\frac{j\omega_n}{L_s} + Q_L)}{\frac{j\omega_n}{L_n} + \frac{j\omega_n}{L_s} + Q_L} = \left| \frac{\mathbf{Z_{in}}(j\omega_n)}{Z_0} \right| e^{j\varphi} \tag{2.3}$$

In the above equation, φ indicates the phase of the input impedance and should be positive in all operating conditions to provide turn on Zero Voltage Switching (ZVS) conditions for power MOSFETs. Operation in this mode is recommended for practical applications [48]. In the LLC resonant converter with selected L_n and L_s, there is a resonant frequency f_r for each constant value of Q_L which is defined as the boundary condition between capacitive and inductive regions and occurs at the peak of the voltage gain curves. The minimum and maximum range of f_r versus Q_L variation is located between open circuit and short circuit resonant frequency respectively. Fig. 2.4(a) and 2.4(b) shows the AC equivalent circuit of the LLC resonant converter in output short circuit and open circuit conditions respectively. The normalized input impedance and resonant frequency in the conditions described are calculated as follows:

$$\frac{Z_{in,sc}(j\omega_n)}{Z_0} = \frac{1-(1+\frac{1}{L_n+L_s})\omega_n^2}{j(\frac{1}{L_n}+\frac{1}{L_s})\omega_n},\ \omega_{n,sc} = \frac{1}{\sqrt{1+\frac{1}{L_n+L_s}}} \tag{2.4}$$

$$\frac{Z_{in,oc}(j\omega_n)}{Z_0} = \frac{1}{j\omega_n} + j\omega_n(1+\frac{1}{L_n}),\ \omega_{n,oc} = \frac{1}{\sqrt{1+\frac{1}{L_n}}} \tag{2.5}$$

According to (2.4), short circuit resonant frequency depends on L_s, and for a non-ideal transformer with a secondary leakage inductance the short circuit resonant frequency is always less than unity. By setting the input impedance phase equal to zero, the normalized resonant frequency can be obtained, which is presented in (2.6).

$$\begin{aligned}
&\frac{\omega_r}{\omega_0} = \sqrt{\frac{A+\sqrt{B}}{C}},\\
&A = (L_n+L_s)^2 + (1+L_n)L_nL_s^2Q_L^2,\\
&B = (-(L_n+L_s)^2 + (1+L_n)L_nL_s^2Q_L^2)^2 + 4L_n^2L_s^2Q_L^2((L_n+L_s)^2+L_n+L_s),\\
&C = 2((L_n+L_s)^2+L_n+L_s)
\end{aligned} \tag{2.6}$$

Fig. 2.5 shows $\frac{\omega_r}{\omega_0}$ versus loaded quality factor for $L_n = 1$ and different constant values of L_s. According to Fig. 2.5, a low value of L_s (existence of the secondary leakage inductance) leads to a narrow range of resonant frequency variation, when loaded quality factor variation is between zero (short circuit) and infinite (no-load condition). The existence of the secondary leakage inductance in the LLC resonant converter puts the short circuit and open circuit resonant frequency close to each other, which leads to steeper voltage gain curves (higher negative slope) and better output voltage regulation with less switching frequency variation. By increasing the switching frequency, the voltage gain curves decrease faster when the

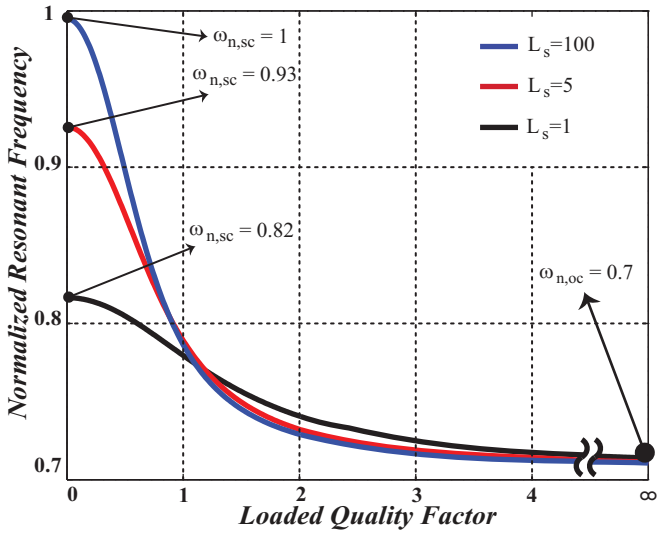

Figure 2.5: Normalized resonant frequency as a function of loaded quality factor for different constant values of L_s and $L_n = 1$

secondary leakage inductance exists. This finding is particularly important to achieve extreme regulation for battery charger applications while keeping a limited frequency range.

In order to figure out the voltage transfer function, it is necessary to calculate the voltage gain of each part of the LLC resonant converter. According to Fig. 2.3(a), the voltage transfer function of the LLC resonant converter is a product of three parts of the block diagram. In the VF method, the fundamental component of full bridge output voltage can be expressed as:

$$v_{AB_1}(t) = \frac{4V_{in}}{\pi} sin\omega_s t \tag{2.7}$$

Also the voltage transfer function and AC equivalent resistance of the current-driven rectifier in continuous conduction mode of the output rectifier is obtained as:

$$M_{v_R} = \frac{\pi}{2\sqrt{2}} \; and \; R_{eq} = \frac{8n^2}{\pi^2} R'_L \tag{2.8}$$

By using KVL and KCL rules and (2.2), the voltage transfer function of the resonant

circuit is:

$$M_{v_r} = \left| \frac{j\omega_n Q_L L_s}{Q_L L_n L_s + j\omega_n (L_n + L_s)} \right| \frac{1}{|\mathbf{Z_{in}}(j\omega_n)|} \tag{2.9}$$

and finally, the voltage transfer function of the full bridge LLC resonant converter is:

$$M_v = \frac{V_{out}}{V_{in}} = M_{v_s}.M_{v_r}.M_{v_R} = \frac{2\sqrt{2}}{\pi}.M_{v_r}.\frac{\pi}{2\sqrt{2}} = M_{v_r} \tag{2.10}$$

The amplitude of the input resonant circuit current (switches current) in VF mode is obtained using (2.3) and (2.7) is:

$$|I_{L_{s_1}}| = \frac{4V_{in}}{\pi |Z_{in}(j\omega_n)|} \tag{2.11}$$

Equations (2.3), (2.7), (2.9), and (2.11) will be used in order to design a high power LLC resonant converter with wide output voltage regulation.

2.2 Soft Switching in Fixed Frequency Phase Shift Approach

In order to provide a low-noise environment for the control circuits, it is vital to achieve soft switching conditions for all semi-conductor elements in different output load conditions. In VF mode, the LLC resonant converter should be designed in the inductive region, while in Fixed Frequency Phase Shift (FFPS) approach, not only the zero crossings of the resonant current must be within the full-bridge output voltage pulse, but also the resonant current should charge and discharge the MOSFETs Drain-Source capacitances [107, 108]. This means the energy stored in the resonant circuit should be enough to charge and discharge the Drain-Source effective capacitances within the dead time interval (Fig. 2.2). In this section, the

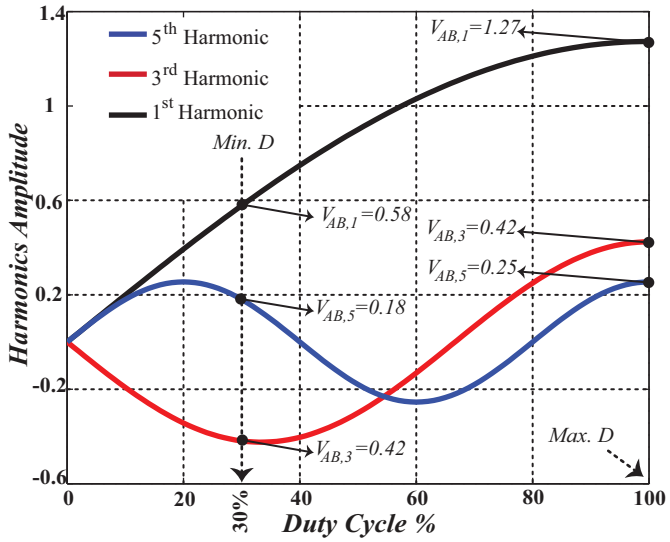

Figure 2.6: The amplitude of square waveform harmonics as a function of duty cycle.

minimum essential circulating current for achieving soft switching conditions in maximum phase shift will be obtained. In the FHA technique, the resonant circuit is considered a low pass filter with nearly sinusoidal current waveforms in its input port. This means the power is transferred from the high frequency inverter to the load via fundamental harmonic of $v_{AB}(t)$, which is correct when the switching frequency is tuned too close to the circuit resonant frequency. But this assumption is not valid when the switching frequency is far from the resonant frequency. Moreover, the phase shift strategy, which happens in the maximum switching frequency for wide regulation, leads to amplitude variations of the square waveform harmonics. The Fourier series expansion of the square waveform with the amplitude of $\pm V_{in}$ and variable duty cycle D is expressed as:

$$v_{AB}(t) = \frac{V_{in}}{\pi} \sum_{n=1}^{\infty} \frac{1-(-1)^n}{n} (cosn\pi(\frac{1-D}{2}) - cosn\pi(\frac{1+D}{2}))sin(n\omega t) \tag{2.12}$$

According to (2.12), the square waveform consists only of components of odd-integer

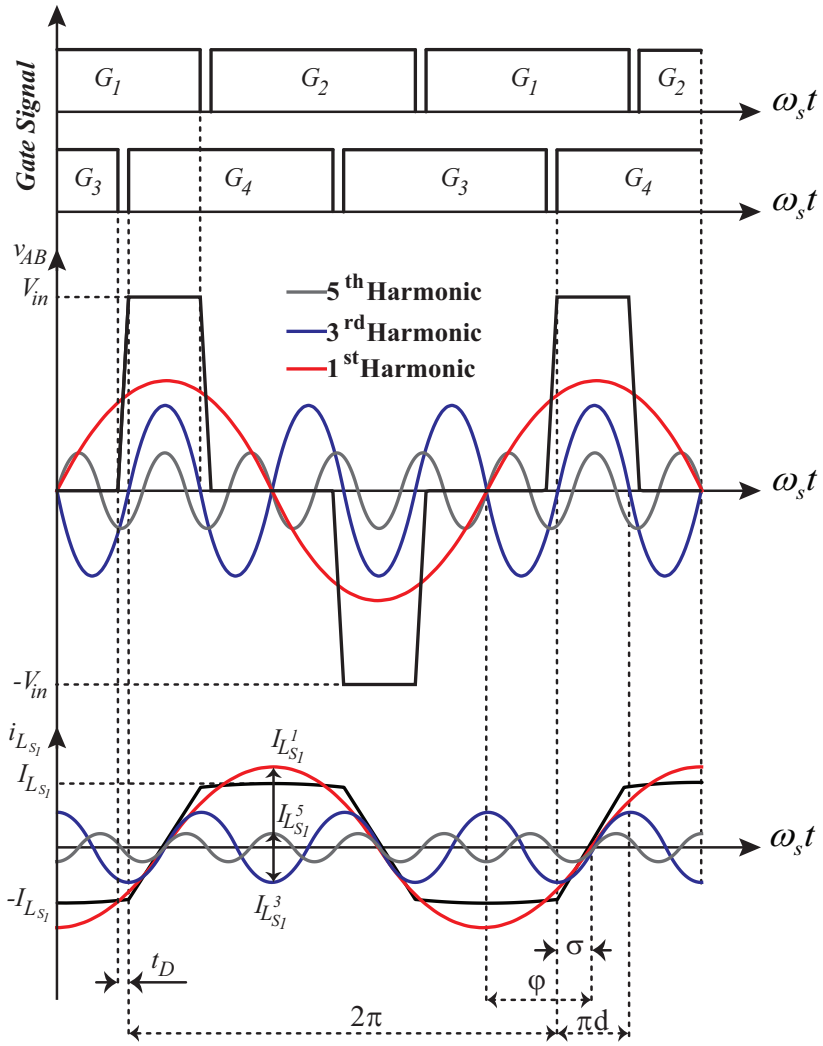

Figure 2.7: Main waveforms of the *LLC* resonant converter in fixed frequency phase shift mode.

harmonic frequencies, which can be considered as different excitations applied to the input port of the *LLC* resonant converter. Fig. 2.6 shows the amplitude of the square waveform harmonics versus duty cycle. Due to the negligible effect of higher harmonics on the steady state behavior of the circuit, only harmonics up to the fifth order are considered. Fig. 2.7 shows the key waveforms of the *LLC* resonant converter in FFPS mode. Due to the effect of higher harmonics on the resonant converter waveforms at maximum switching frequency, the resonant current is neither sinusoidal nor triangular. In this case, the amplitude of the

resonant circuit input current can be determined by:

$$i_{Ls_1}(t) = \sum_{k=1,3,5} \frac{v_{AB}(t)}{Z_{in}(jk\omega_n)} = I^1_{Ls_1} sin(\omega t + \varphi_1) + I^3_{Ls_1} sin(3\omega t + \varphi_3) + I^5_{Ls_1} sin(5\omega t + \varphi_5) \tag{2.13}$$

To achieve minimum output current in short circuit conditions, the maximum phase shift is required. In this case, the minimum circulating current exists in the resonant circuit, and the phase angle of all harmonics in (2.13) is equal to 90°. Therefore, the minimum resonant current amplitude is obtained as follows:

$$I_{L_{s_1}} = I^1_{Ls_1} - I^3_{Ls_1} + I^5_{Ls_1} \tag{2.14}$$

Fig. 2.7 shows the resonant current waveforms along with its different harmonics (1st, 3rd, and 5th) in phase shift mode. In the full bridge inverter and during the dead time interval, the resonant current should charge and discharge two Drain-Source capacitances. Therefore the minimum resonant circuit current is defined as follows:

$$\mid I_{Ls_1} \mid \geq 2C_{DS}\frac{V_{in}}{t_D} \tag{2.15}$$

As demonstrated by the analysis and equations (2.14)-(2.15), the LLC resonant tank driven by FFPS should be designed to provide the minimum circulating current required to achieve soft switching transitions (to discharge the Drain-Source effective capacitance of the MOSFETs). The minimum circulating current depends on the selected MOSFET output equivalent capacitance (energy related $C_{oss,er}$), the minimum dead time, and the input voltage level.

2.3 Design of Experiment Methodology (DoE)

In this section, the Design of Experiment (DoE) methodology is employed to consider the behaviour of the LLC resonant converter when responding to variations in different normalized parameters [98]. This methodology provides a systematic approach for applying statistics to experimentation in order to achieve efficient and accurate results. In other words, it is used to find cause-and-effect relationships between input variables and output results, by employing output response surfaces. There are many advantages to using this modeling process: it is quick, practical, and easy to employ [109, 110]. Due to the battery charger application, the main objective of the design procedure is to obtain a special LLC resonant tank to provide maximum output voltage regulation, while minimizing circulating current in part load conditions and providing soft switching conditions (in both VF and FFPS mode). The mentioned methodology can be employed to consider the behaviour of the LLC resonant converter when responding to variations in different normalized parameters of the LLC resonant converter, including L_n, L_s, and Q_L. The output response surfaces have been selected based on the most important attributes for a battery charger application, which are wide output voltage capability, high part load efficiency and soft switching in all conditions. In the following subsections, these attributes will be discussed in detail.

2.3.1 Maximum Output Voltage Regulation

In order to respond to the charge algorithm, the charger needs to regulate the output voltage from near zero up to 1.5 times the nominal voltage under different loading conditions. In the LLC resonant converter, the voltage gain curves can approach almost zero voltage in high frequency when the absolute value of the gain curves' slope at the short circuit resonant frequency is set to be maximized. Also, in order to obtain the maximum voltage gain slope,

as stated in Section 2.1, the difference between $f_{r,oc}$ and $f_{r,sc}$ should be minimized. Therefore, output response surfaces is based on the optimization of the following criteria:

$$\begin{cases} \left| \frac{\partial M_v}{\partial f_n} \right|_{f_n = f_{r,sc}} \rightarrow Maximize \ \ or \\ f_{r,sc} - f_{r,oc} \rightarrow Minimize \end{cases} \tag{2.16}$$

According to Section 2.1, when the the voltage gain of the resonant converter has a steeper negative slope, the open circuit and short circuit resonant frequencies are closer, and vice versa. Therefore, both terms presented in (2.16) have the same meaning, and in the following section, the first one will be used as the first output of the methodology.

2.3.2 High Part Load Efficiency

In resonant power converters, the circulating current has a negative impact on the efficiency under part-load and light-load conditions and it is favorable to have a constant relation between the output power and the amplitude of the resonant current. This means that if the output current decreases by 50%, so does the amplitude of the resonant currents. Through appropriate selection of resonant circuit elements, the amplitude of the resonant circuit current decreases with increasing load resistance, reducing conduction loss and providing high part-load efficiency. In other words, the less part load circulating current there is, the flatter the efficiency curve is in relation to load. Eq. (2.17) presents the second output of the methodology that should be maximized.

$$\frac{I_{L_{s1},FL}}{I_{L_{s1},HL}} \rightarrow Maximize \tag{2.17}$$

2.3.3 Soft Switching Condition

In order to provide safe and an accurate operation for the drive circuits of the power MOSFETs as well as for the Battery Management System, it is necessary to provide soft switching conditions for the LLC resonant converter in all operating areas. In the following, this criterion will be considered for both VF and FFPS approaches.

VF Mode

To guarantee the soft switching in the VF mode, the phase angle of the input impedance in all load conditions should be positive. ZVS is guaranteed for the VF mode, if the switching frequency is greater than the resonant frequency ($\varphi > 0$), which means the resonant current is lagging the output voltage of the full-bridge inverter. Ideally, in order to minimize the resonant circuit current, which is defined as the conduction losses in all active and passive elements, it is desirable to set φ equal to zero. But, in practice, variations (including the resonant circuit elements variations versus temperature and the input voltage ripple of the Power Factor Correction (PFC) stage) necessitate a minimum margin for φ during the design procedure. Moreover, in order to provide enough time to charge and discharge the MOSFETs Drain-Source capacitances in the same leg, a dead time should be defined between gate signals (e.g. $200nSec$). On the other hand, if this angle is too steep, the input resonant current peak will increase, which leads to more conduction losses and more voltage stresses on semiconductor devices and other passive elements. Eq. (2.18) presents the minimum range of the input impedance phases in nominal load conditions that the output response should fall within.

$$\begin{cases} \varphi > 10^{\circ} & \text{for practical margin} \\ \varphi < 30^{\circ} & \text{for high efficiency achievement} \end{cases} \tag{2.18}$$

Table 2.1: Normalized Parameters Range and Selected Value

Parameters	*Range*	*Selected*
L_n	$[0.5 - 1.5]$	1
L_s	$[2 - 10]$	5
Q_L	$[0.2 - 1]$	0.5

It is worthwhile to mention Eq. (2.17) reflects the flatness of the efficiency curve, and Eq. (2.18) reflects the amplitude of the resonant circuit current, which represents the maximum achievable efficiency. It is thus possible to model the converter efficiency/power loss if all components of the circuit and their resistances are defined.

FFPS Mode

In terms of resonant converter power loss, one of the main concern is the circulating current in the primary side. However, for high input voltage applications (e.g. $V_{in} = 400VDC$), the switching loss is more than the conduction loss and, therefore, the existence of circulating current leads to soft switching conditions. According to Fig. 2.7, the minimum circulating current occurs under short circuit conditions and when using the FFPS method. In this case it is vital to set this current in such a way as to almost completely charge and discharge MOSFETs' Drain-Source capacitance. According to (2.15) and Fig. 2.7, the minimum current depends on the effective capacitance displayed in parallel with the Drain-Sources of the power MOSFETs, the level of the input voltage, and the maximum allowable dead time. Eq. (2.19) presents the last output of the methodology that should be optimized.

$$| I_{Ls_1}| = I^1_{Ls_1} - I^3_{Ls_1} + I^5_{Ls_1} \rightarrow Maximize \tag{2.19}$$

In the following paragraphs, the output response surfaces of the Multivariate Statistical

Table 2.2: Modeling Results of the Normalized LLC Resonant Converter

L_n	L_s	Q_L	$\left\| \frac{\partial M_v}{\partial f_n} \right\|$	φ	$\frac{I_{L_{s1},FL}}{I_{L_{s1},HL}}$	$\frac{I_{L_{s1},sc} Z_0}{V_{in}}$
0.5	4.75	0.44	1.51	12.4	4.3	0.396
1	4.75	0.44	3.67	21.4	2.66	0.405
0.5	8.25	0.44	1.31	12.2	4.27	0.44
1	8.25	0.44	2.85	22.3	2.56	0.444
0.5	4.75	0.81	1.7	21.9	2.61	0.396
1	4.75	0.81	3.64	36	1.68	0.405
0.5	8.25	0.81	1.3	22	2.59	0.44
1	8.25	0.81	3.17	37.3	1.63	0.444
0.33	6.5	0.625	0.86	11.9	4.39	0.42
1.17	6.5	0.625	3.89	33.5	1.79	0.43
0.75	5.56	0.625	3.65	23	2.46	0.376
0.75	9.44	0.625	2	22.4	2.36	0.45
0.75	6.5	0.31	2.2 3	11.9	4.31	0.425
0.75	6.5	0.94	2.22	33.9	1.77	0.425
0.75	6.5	0.625	2.56	24	2.38	0.425

Design methodology will be considered.

In this work, Design-Expert Software from Stat-Ease is employed in order to find cause-and-effect relationships between input variables and output results [98]. As a summary, the procedure of using this software for finding the optimum amount of normalized parameters along with the information about the current design is as follows:

- The number of input variables and output responses are defined by the user (three inputs and four outputs).
- The software will ask for a range for each input variable. This is time consuming, since the variable ranges need to be iteratively determined, starting from wide ranges and shrinking them based on the previous results.
- The software will define a minimum number of simulations based on the number of inputs and their ranges (15 simulations for this example).

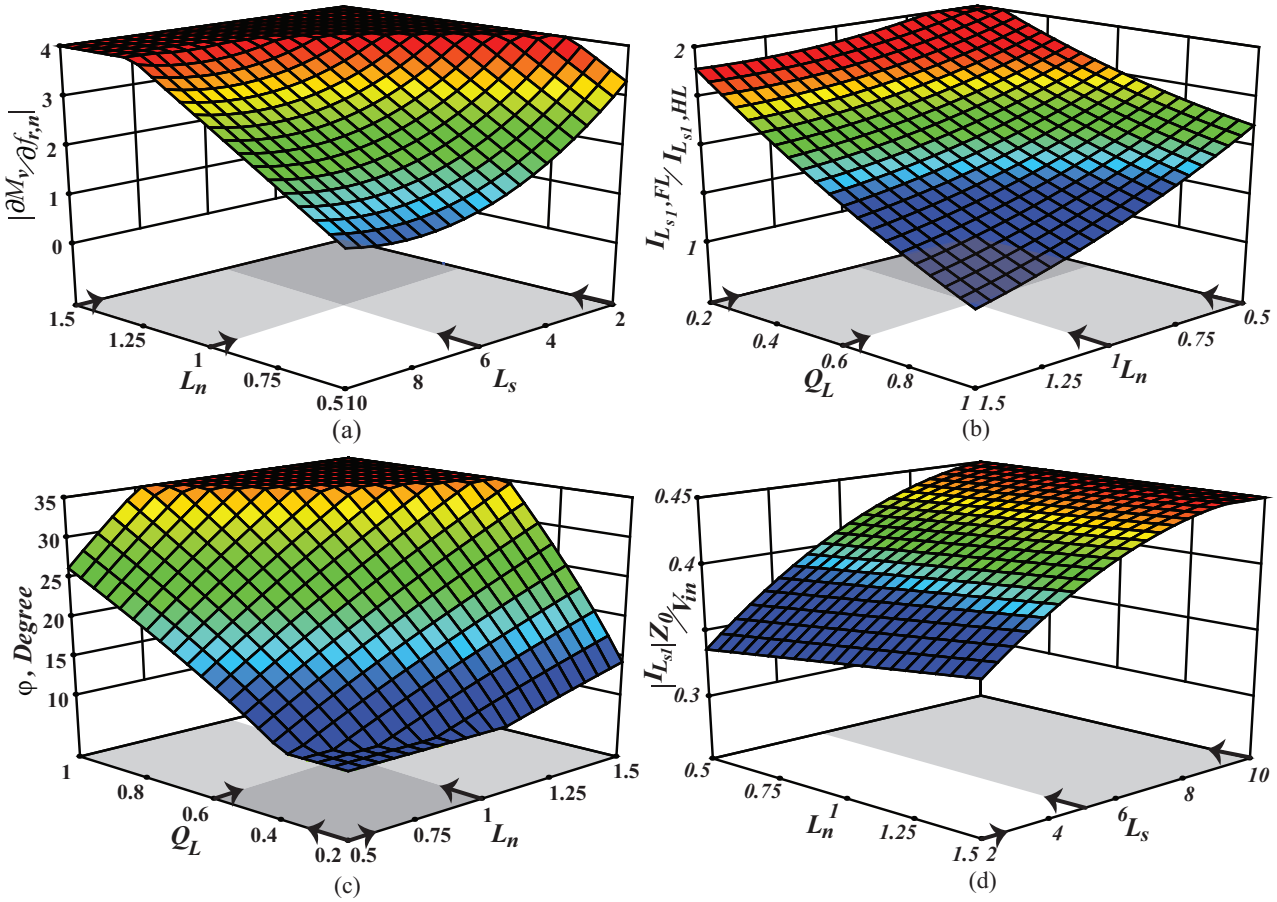

Figure 2.8: Multivariate statistical design methodology response surfaces for LLC resonant converter: (a) Voltage gain slope surface versus L_n and L_s, (b) Input resonant circuit current ratio versus L_n and Q_L, (c) Phase of the input impedance versus L_n and Q_L, (d) The circulating current amplitude under short circuit conditions versus L_n and L_s.

- The next step is to find out the output results related to input values (presented in the right side of Table 2.1).
- Entering data for both inputs and outputs, the software will draw a three-dimension surface response for each output versus two inputs, which has more influence on the surface response.
- Analyze the accuracy of the statistical results.

According to the steady-state analysis performed in Section 2.1, the equations obtained

for the LLC resonant converter are functions of three normalized variables, which are L_n, L_s, and Q_L. Table 2.1 presents the range for normalized parameters, which will be used as the inputs. It is worthwhile to mention the presented ranges in Table 2.1 have been defined after running DoE for wider ranges of input parameters and refining them. In order to select the optimized LLC resonant converter parameters, based on the number of normalized parameters, the methodology dictates the minimum number of simulation (which is 15 simulations in this example) to cover the effects of all three normalized parameters in the ranges discussed. The left side of Table 2.2 presents the values of the normalized parameters that must be used in order to extract different responses, such as voltage gain slope, phase of the input impedance, etc. In fact, the normalized parameters are input into the steady state equations of the LLC resonant converter and output results will be entered in the right side of Table 2.2. Then the Analysis of Variance Regression is employed to extract the mathematical equations, which are presented in (2.20)-(2.22), in order to model the system and draw the response surfaces. The response surfaces for LLC resonant converters have been presented in Fig. 2.8. It is necessary to mention that the surface responses presented in Fig. 2.8(a)-(d) have been drawn based on the two normalized parameters that have the most impact on the surface.

$$\begin{aligned}\varphi^{1.41} = &- 4.76 - 28.83L_n - 1.72L_s + 13.2Q_L + \\ &3.66L_nL_s + 211.28L_nQ_L\end{aligned} \tag{2.20}$$

$$\left(\frac{I_{L_{s1,FL}}}{I_{L_{s1,HL}}}\right)^{-1.17} = 0.026 - 0.12L_n - 3.95L_s - 0.1Q_L + 8.83L_nL_s + 0.63L_nQ_L + 0.06Q_L^2 \tag{2.21}$$

$$\frac{I_{L_{s1,sc}}Z_0}{V_{in}} = 0.26 + 0.03L_n - 2.86L_nL_s - 1.38L_s^2 \tag{2.22}$$

Having identified the above requirements, it is now possible to select normalized parameters by considering the different response surfaces at the same time. As explained, having a wide regulation for the output is one of the most important specifications for a battery charger. According to Eq. (2.16), in order to achieve the maximum possible regulation, the absolute value of the voltage gain derivation versus normalized frequency at the short circuit resonant frequency should be set to be maximized. According to Fig 2.8(a), in order to satisfy Eq. (2.16), the L_n and L_s should be, respectively, at the highest and lowest possible levels (the red part of the surface). Two ranges are defined for normalized parameters (gray band), and the points located in the common area (dark gray) are candidates for optimum L_n and L_s parameters. According to Eq. (2.17), in order to get a flat efficiency curve, the amplitude of the resonant circuit current in half load condition should be half of the full load condition. According to Fig 2.8(b), in order to satisfy Eq. (2.17), both the Q_L and L_n should be at the lowest possible levels (the red part of the surface). Two ranges are defined for normalized parameters (gray band), and the points located in the common area (dark gray) are candidates for optimum Q_L and L_n parameters. For providing soft switching condition in VF mode, the input impedance phase of the resonant circuit should fall within the range specified in Eq. (2.18). According to Fig 2.8(c), in order to satisfy Eq. (2.18), both Q_L and L_n should

be at the lowest possible levels (the blue part of the surface). Two ranges are defined for normalized parameters (gray band), and the points located in the common area (dark gray) are candidates for optimum Q_L and L_n parameters. Also, in order to have soft switching condition in FFPS mode, a minimum circulating current is necessary to charge and discharge the MOSFETs' Drain-Source capacitances. According to Fig 2.8(d), in order to satisfy Eq. (2.19), the L_s should be at the highest possible level, while the other normalized parameter does not affect the amplitude of the circulating current at the short circuit condition. Finally, the intersection between different common areas determines the values of normalized parameters. The final values of normalized parameters have been selected after conducting simulations and taking into account practical considerations (e.g. the maximum allowable dead time, obtainable amount of secondary leakage inductance, the effective Drain-Source capacitance of the selected MOSFET). The selected values for normalized parameters are presented in Table 2.1. It is worthwhile to mention other modeling techniques (Tabu search algorithm, numerical solution, and genetic algorithm) can be employed to find the optimum design of the resonant converters [7, 57, 111]. While the other solutions might provide more accurate results, they are time consuming and need more complicated program languages. The Design of Experiment is a straightforward methodology and can provide response surfaces for the objectives with a minimum number of simulations.

2.4 Resonant Power Converter Design

Based on the optimized selection of normalized parameters, the normalized steady state equations of the LLC resonant converter will be used to design a high power LLC resonant converter. Fig. 2.9 presents the voltage transfer function M_v, the first series inductance current $I_{L_{s_1}}$, and the input impedance phase φ versus frequency for the selected values

of normalized parameters ($L_n = 1$, $L_s = 5$) and the constant values for normalized load resistances Q_L. In Fig. 2.9(a), the voltage gain curves versus the normalized switching frequency are presented for different loaded quality factor. As presented, there are two boundaries for minimum and maximum switching frequency ($f_{n,min}$ and $f_{n,max}$), and the voltage gain curves are studied between them. According to Fig. 2.9(a), a higher loaded quality factor has a higher voltage gain and vice versa. In Fig. 2.9(b), the amplitude of the resonant circuit current versus the normalized switching frequency are presented for different loaded quality factor. As presented, a higher loaded quality factor leads to a lower normalized resonant current. In other words, increasing the load resistance in the output of the converter leads to decreasing the resonant circuit current. In Fig. 2.9(c), phase of the input impedance of the resonant circuit current versus the normalized switching frequency is presented for different loaded quality factor. As discussed previously, in order to realize the soft switching condition, the input impedance phase has to be positive for any operating point. In the following FHA results will be used in order to find out the resonant circuit elements. According to Fig. 2.9(a), the voltage gains are almost independent from the load when the switching frequency is around the short circuit resonant frequency ($f_{r,sc}$), resulting in minimum switching frequency variation versus load at nominal output voltage. Moreover, Fig. 2.9(b) shows that at f_0 the input resonant circuit current decreases in higher Q_L, resulting in high efficiency in part load conditions. This point is selected for nominal output voltage operation. As shown in Fig. 2.9(a), the minimum switching frequency is determined by the maximum output voltage in nominal output power ($Q_L = 1.12$). Fig. 2.9(c) presents the phase of the resonant circuit input impedance versus frequency for different load conditions. According to Fig. 2.9(c), the resonant circuit works in inductive mode for the operating regions described, and ZVS is provided for the full-bridge inverter. In the following description, the LLC resonant circuit elements are calculated based on the voltage transfer function curves and the charger specifications including the input voltage, output

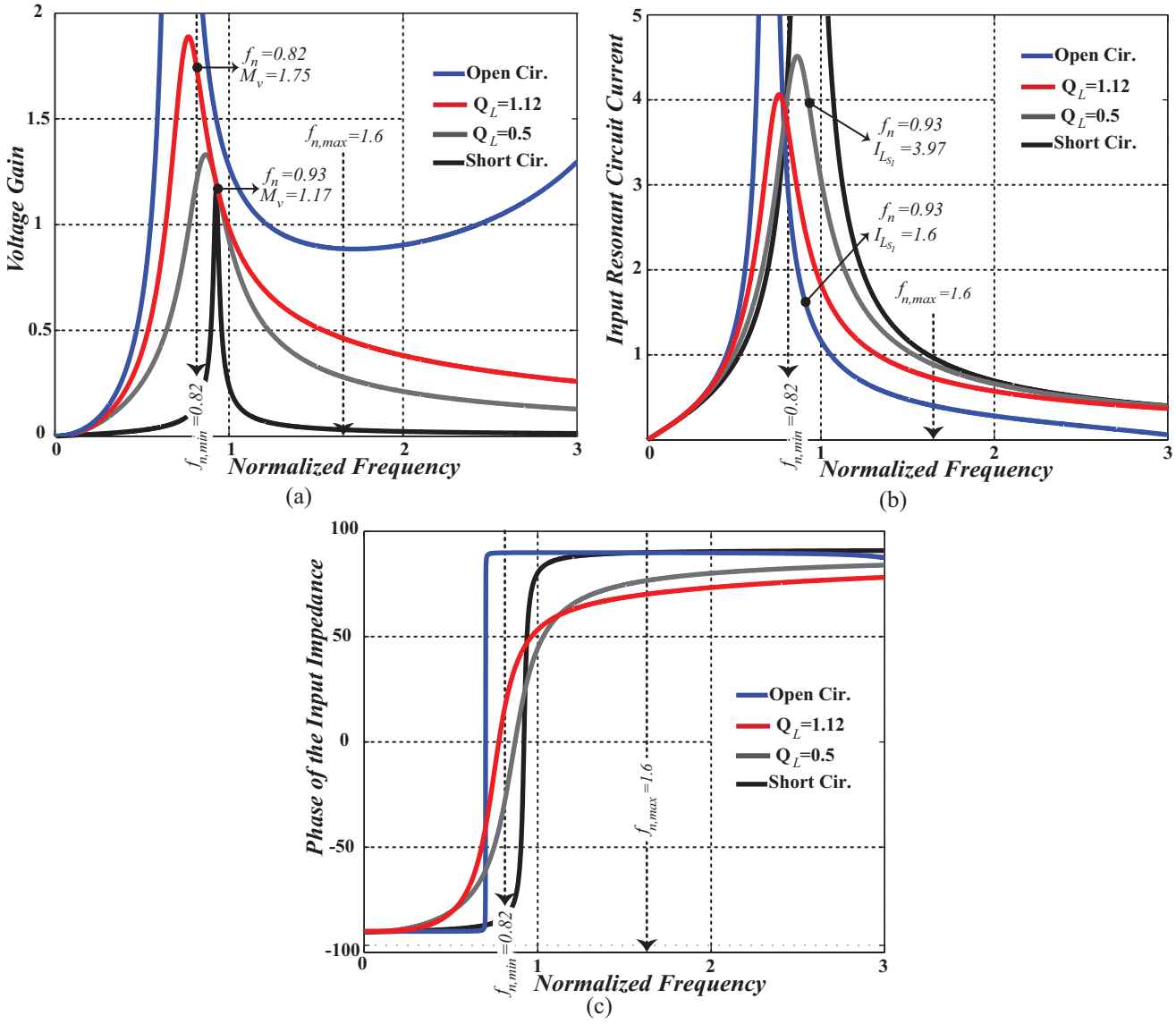

Figure 2.9: FHA analysis of the LLC resonant converter for $L_n = 1$, and $L_s = 5$, with constant values for normalized load resistances (Q_L): (a) Magnitude of voltage transfer function (M_v), (b) Magnitude of input resonant circuit current ($I_{L_{s_1}}$), (c) Phase of the input impedance (φ).

voltage, output power and switching frequency variations. The main specifications of the battery charger are as follows:

$$V_{in} = 400VDC,\ V'_{bat} = 120VDC,\ P_{out} = 3kW,\ f_s = 100 - 200kHz \tag{2.23}$$

According to Fig 2.9(a), the minimum normalized switching frequency is equal to 0.82. Therefore, the resonant frequency (f_0) is calculated using the following equation:

$$f_{n,min} = 0.82,\ f_{s,min} = 100kHz,\ f_n = \frac{f_s}{f_0} = \frac{100}{0.82} \implies f_0 = 122kHz \tag{2.24}$$

Note that due to the practical restriction at light or no-load condition (the oscillation between transformer secondary side capacitances and other parasitics elements) the maximum switching frequency has been selected through experimental prototype to be 1.6 times f_0 to prevent the LLC resonant converter from entering in positive feedback region. In nominal load conditions ($Q_L = 0.5$), the voltage gain is equal to 1.17 and, as a result, the transformer turn's ratio is obtained as follows:

$$n = \frac{N_p}{N_s} = \frac{V_{bat,n}}{V'_{bat,n}} = \frac{M_v.V_{in}}{V'_{bat}} = \frac{1.17 \times 400}{120} = 3.9 \tag{2.25}$$

In the LLC resonant converter with capacitive output filter, the equivalent resistance is obtained using (2.8):

$$R'_L = \frac{{V'_{bat}}^2}{Pout} = \frac{120^2}{3000} = 4.8\Omega \implies R_{eq} = n^2 R'_{eq} = 3.9^2 \times 4.8 = 59.2\Omega \tag{2.26}$$

Finally, the circuit elements of the LLC resonant converter are calculated as follows:

Table 2.3: *LLC* Prototype Platform Parameters

Parameters	Value
Input Voltage, V_{in}	$400VDC$
Nominal Battery Voltage, $V'_{bat,n}$	$120VDC$
Maximum Battery Voltage, $V'_{bat,m}$	$180VDC$
Maximum Output Power, P_{out}	$3kW$
Switching Frequency Range, f_s	$100 - 200kHz$
Resonant Frequency, f_0	$122kHz$
Series Resonant Capacitance, C_s	$11nF$
First Series Resonant Inductance, L_{s_1}	$154\mu H$
Second Series Resonant Inductance, L_{s_2}	$31\mu H$
Parallel Resonant Inductance, L_p	$154\mu H$
Transformer Turn's Ratio, $n = \frac{N_p}{N_s}$	4

$$
\begin{aligned}
&Z_0 = \frac{R_{eq}}{Q_L} = \frac{59.2}{0.5} = 118.4\Omega,\ \omega_0 = \frac{\omega_s}{\omega_n} = \frac{200\pi e^3}{0.82} = 244\pi e^3 \implies \\
&L_{s_1} = \frac{Z_0}{\omega_0} = \frac{118.4}{244\pi e^3} = 154\mu H,\ C_s = \frac{1}{Z_0.\omega_0} = \frac{1}{118.4 \times 244\pi e^3} = 11nF, \\
&L_{s_2} = \frac{L_{s_1}}{L_s} = \frac{154e^{-6}}{5} = 31\mu H,\ L_p = \frac{L_{s_1}}{L_n} = \frac{154e^{-6}}{1} = 154\mu H
\end{aligned}
\tag{2.27}
$$

The circuit parameters for the *LLC* resonant converter are provided in Table 2.3.

2.5 Simulation and Experimental Results

In order to validate the effectiveness of the proposed modulation method, a prototype platform has been employed to extract the maximum obtainable output voltage regulation under different load conditions. The components used in the prototypes are shown in Table 2.4. Also, the test setup picture is presented in Fig. 2.10. This setup will be modified for all

Table 2.4: Components of Resonant Converters Platforms

Component	*Part Number*	*Ratings*
MOSFET's	$IXFX64N60$	$600VDC, 64A$
Resonant Cap.	*Film Cap.*	$10nF, 2000VDC$
Resonant Ind.	$3F3$	$***$
Transformer	$3F3$	$***$
Rectifier Diode	$MBR40250$	$250V, 40A$
Output Capacitor	*Film Capacitor*	$18uF, 250VDC$

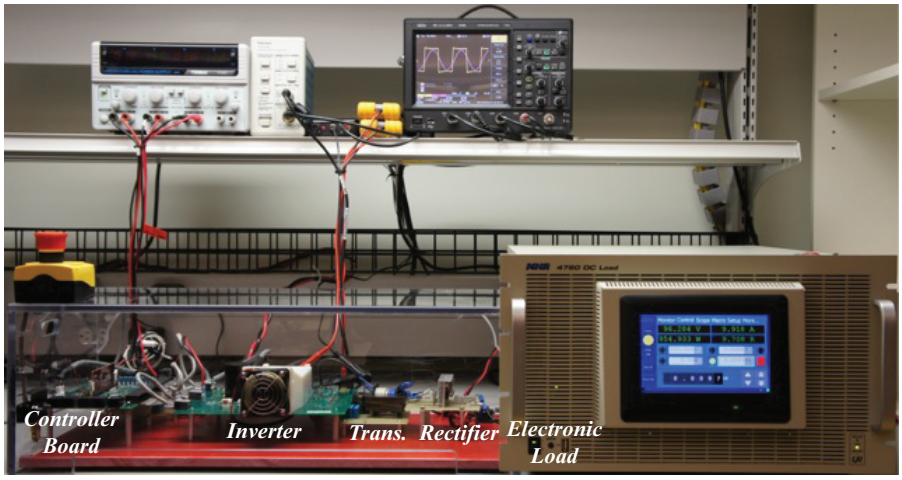

Figure 2.10: Prototype test platform of the resonant power converters.

experimental tests presented in ensuing chapters.

The simulation and experimental results for the output voltage versus frequency are presented in Fig. 2.11 for different output load conditions in solid and dotted shapes, respectively. According to Fig. 2.11, in the LLC resonant converter, the simulation and experimental results are almost the same for $R'_L = 4.8\Omega$ and $R'_L = 10.8\Omega$. But for no-load conditions, there is a discrepancy between simulation and experimental results. In fact, the effect of the parasitic capacitances on the secondary side of the transformer leads to increased output voltage in the LLC at no-load condition. Moreover, around $f_{sw} = 200kHz$, the output voltage curves start to flatten, meaning that there is no more regulation after maximum switching frequency. Fig.

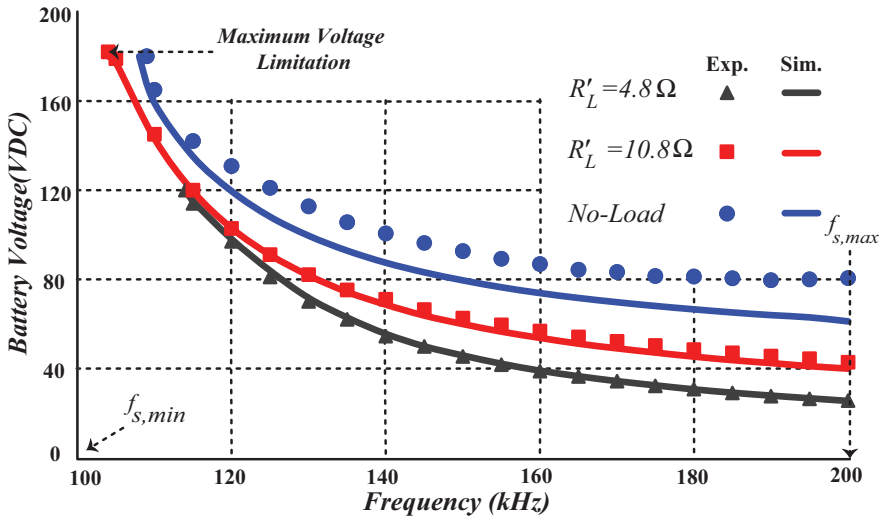

Figure 2.11: Simulation and experimental results for battery voltage versus frequency.

2.12 presents the experimental result for the proposed battery charger in VF mode (Orange: Inverter Voltage, Purple: Resonant Circuit Current, Blue: Transformer Secondary Voltage, Green: Transformer Secondary Current). According to Fig. 2.12, the zero crossings of the resonant circuit input current are within the inverter output voltage pulse and, as a result, in all of the conditions described, the full-bridge switches are fully turned on under zero voltage. Fig. 2.13 present the experimental results of LLC converter in the FFPS mode. The operating mode selection is made by a digital controller. In fact, there is a low and high limitation for switching frequency ($f_s = 100 - 200kHz$), and after reaching to the maximum switching frequency, the controller changes the modulation strategy to phase shift in order to decrease the output voltage. By employing this modulation strategy at the maximum switching frequency, it is possible to improve the output voltage regulation, even under no-load conditions. According to Fig. 2.13, the zero crossings of the resonant circuit input current are within the full bridge output voltage pulse and, as a result, the full-bridge switches are fully turned on under zero voltage. As predicted, the worse case scenario for ZVS occurs under short-circuit and maximum phase shift conditions (minimum effective duty cycle), which is shown in Fig. 2.13(c). According to (2.15) and the selected MOSFETs type for the full bridge inverter,

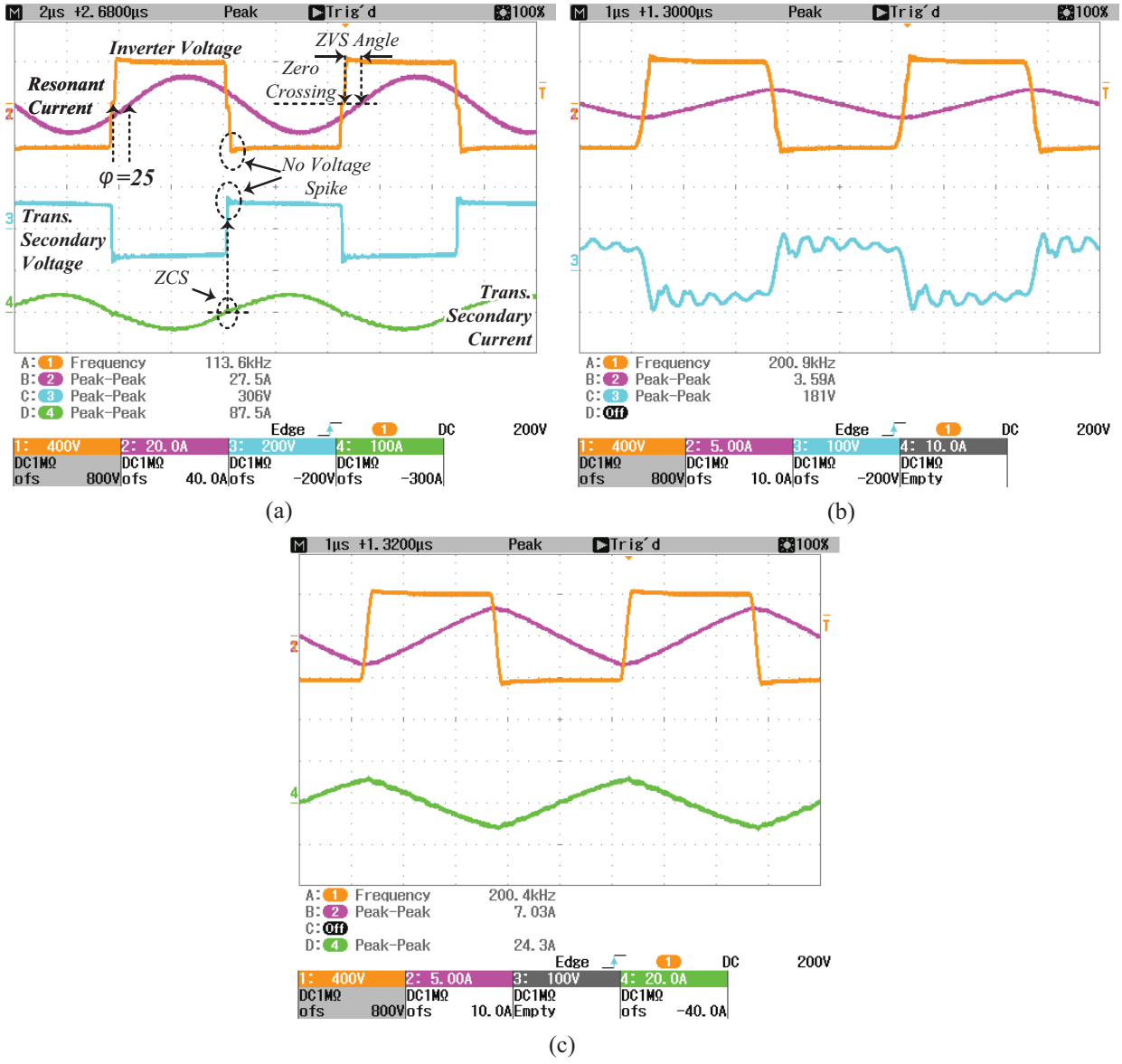

Figure 2.12: Experimental results for the LLC resonant converter in variable frequency mode, (a) $V'_{bat} = 120VDC$ and $P_{out} = 3kW$ (b) $V'_{bat} = 90VDC$ and $P_{out} = 0W$, and (e) $V'_{bat} = 0VDC$ and $I'_{bat} = 7A$.

the amount of circulating current in short circuit conditions is nearly enough to charge and discharge the Drain-Source capacitances of the power MOSFETs during the specified dead time, which is equal to 250nS. The V-I plane obtained from the experimental results is shown in Fig. 2.14. In the V-I plane, there are different limitations on the boundaries, including

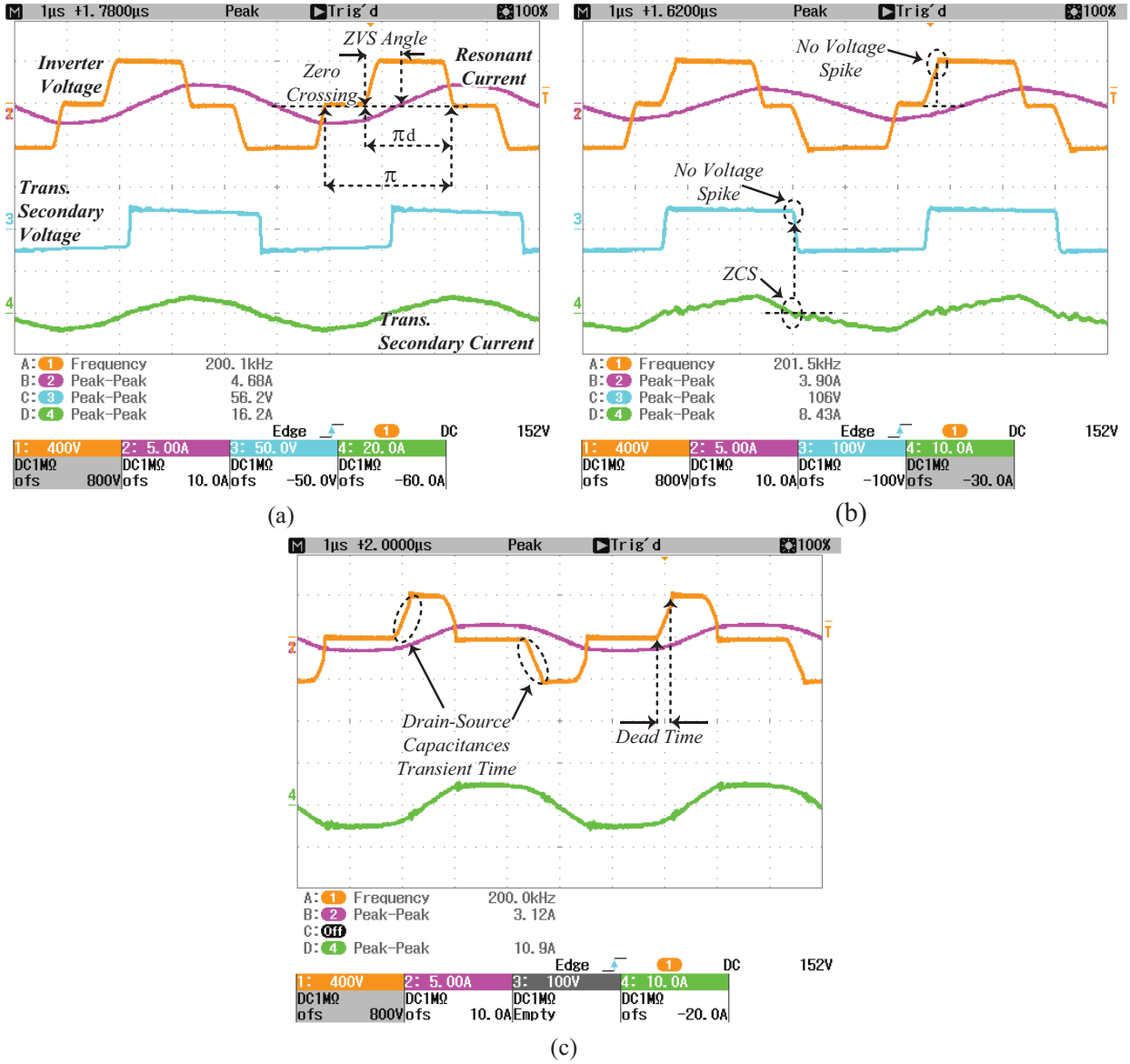

Figure 2.13: Experimental results for the LLC resonant converter in fixed frequency phase shift mode, (a) $V'_{bat} = 20VDC$ and $I'_{bat} = 4.5A$ (b) , $V'_{bat} = 45VDC$ and $I'_{bat} = 2A$, and (c) $V'_{bat} = 0VDC$ and $I'_{bat} = 2A$

current, voltage, power, and no-load conditions, and each point in the plot indicates one experimental test (red and green points indicate VF and FFPS, respectively). According to Fig. 2.14, due to the effects of the junction capacitances of the output diodes on the voltage gains, the LLC resonant converter cannot cover all of the regions in the V-I plain in the VF

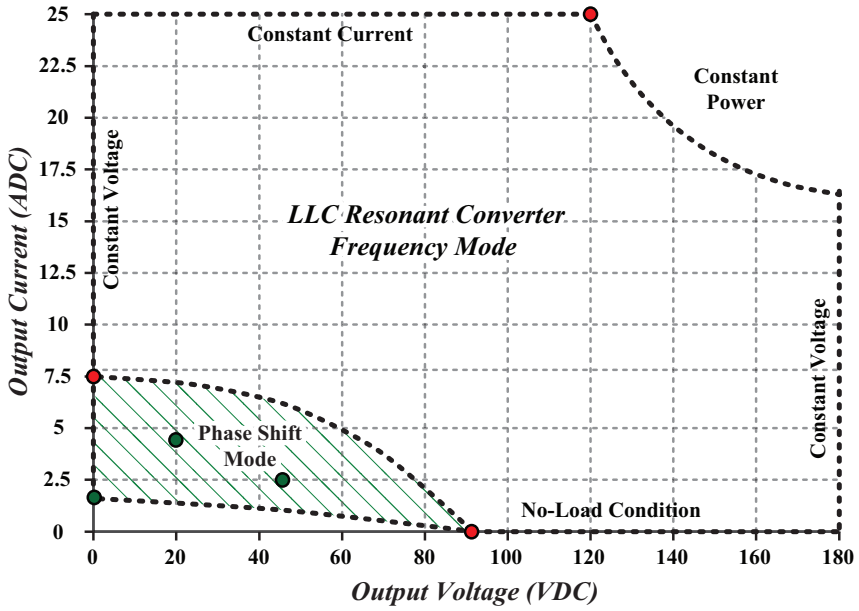

Figure 2.14: V-I plane obtained from the *LLC* resonant converters by employing digital hybrid modulation technique (The green dashed area is obtained by FFPS).

mode ($f_s = 100 - 200kHz$). The unobtainable area of the *LLC* resonant converter starts in the no-load boundary at $V_{out} = 90VDC$ and $f_s = 200kHz$, and for short circuit conditions, the output current is equal to 7 Amps. As mentioned in the introduction, the battery charger must be able to respond to different modes of the charge algorithms and cover almost all of the V-I plane region. The experimental results show that employing the FFPS strategy in the maximum switching frequency and allowable phase shift decreases the output voltage in different load conditions, which results in improved regulation. The green dashed region in Fig. 2.14 indicates the regulation improvement obtained by using FFPS. Fig. 2.15 presents the efficiency curves of the *LLC* resonant converters for three different output voltages. In Appendix D, the method of efficiency measurement is presented. According to these curves, the resonant converters designed for this study present a maximum efficiency equal to 96.5%.

In the following section, the effect of the input voltage variation on the resonant power converter operation will be investigated. Generally, battery charger power architectures in-

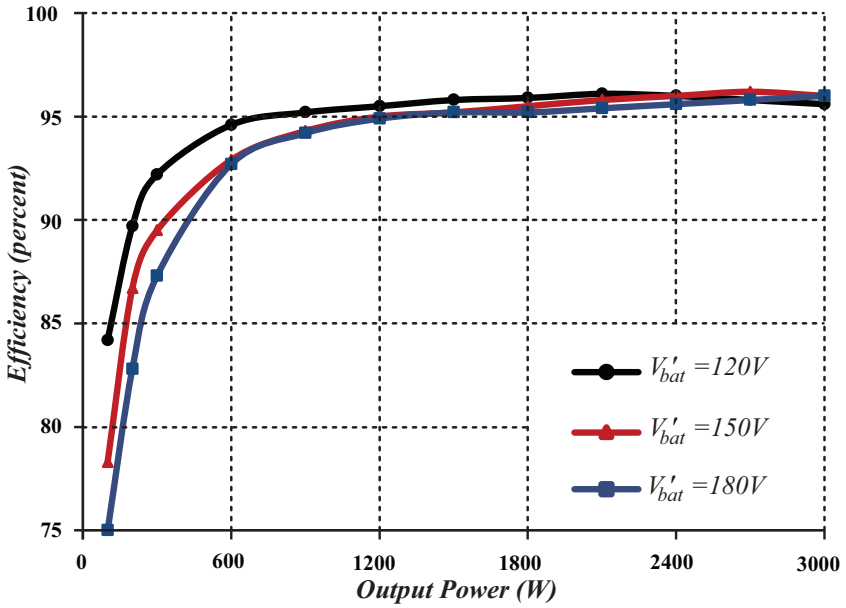

Figure 2.15: Efficiency curves of the *LLC* resonant converter at different fixed output voltages.

clude two main stages, which are AC-DC Power Factor Correction (PFC) and DC-DC isolated power converter. Therefore, the input voltage of the DC-DC resonant converter is provided by a PFC stage, which could be a conventional or interleaved continuous conduction mode boost topology [25, 28]. Generally, the output voltage of the PFC stage is not constant and can have ±10% voltage ripple, so the DC-DC power stage has to compensate this variation. In order to investigate the effect of the input voltage variation for the designed resonant converter, the prototype platform has been tested for the minimum and maximum input voltage ($V_{in} = 360 \sim 440$) and the maximum output power condition ($P_{out} = 3000W$). According to the experimental results presented in Fig. 2.16, the designed *LLC* resonant converter can compensate for the effect of the input voltage variation using frequency modulation, while transferring the maximum power to the battery pack. Comparing Fig. 2.12(a) and Fig. 2.16(a) reveals the difference between the input impedance phase in two different input voltages and in fixed output voltage and output power condition. According to Fig. 2.16(a), the input impedance phase angle of the *LLC* resonant converter is 16°, which still guarantees

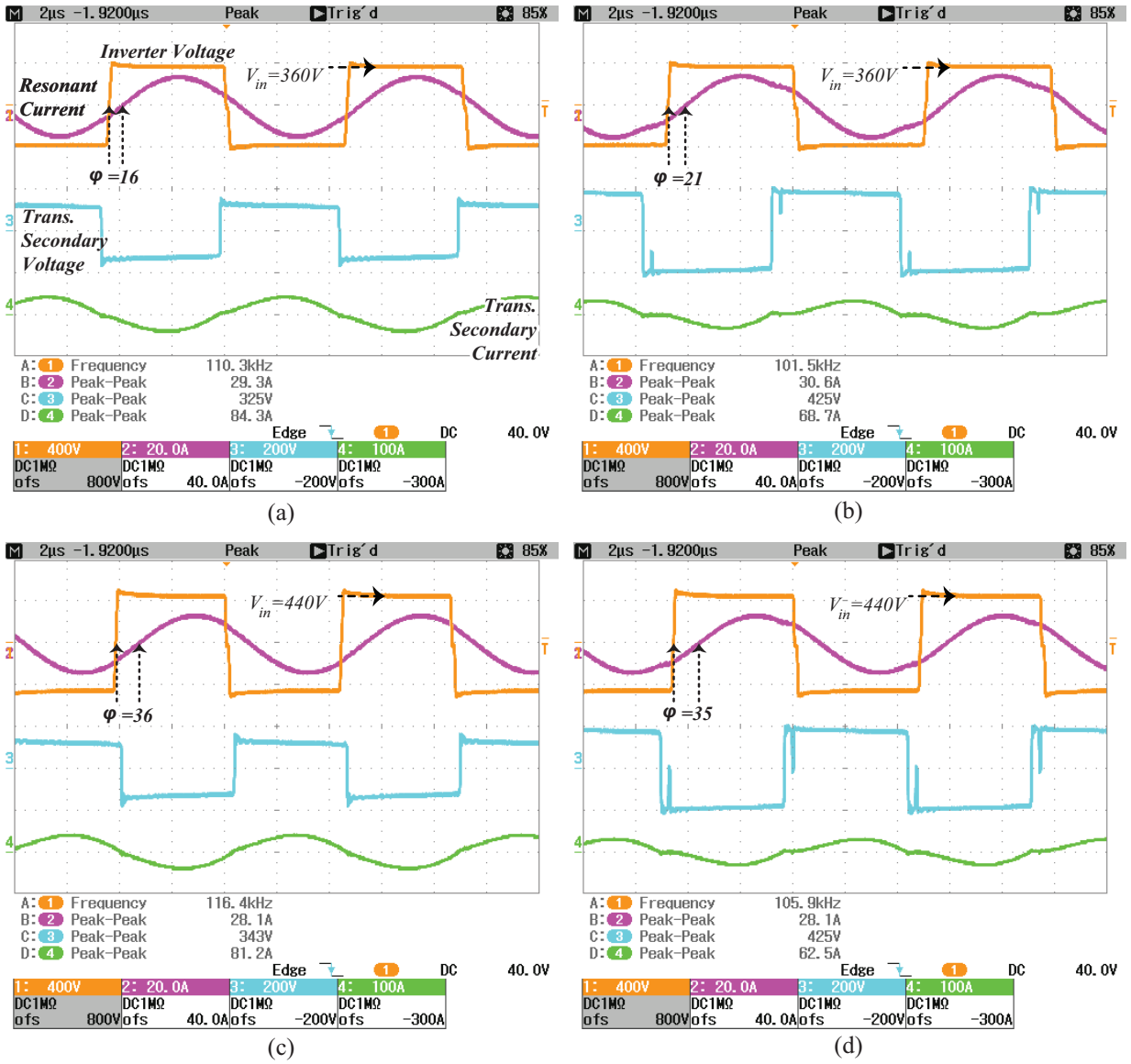

Figure 2.16: The effect of input voltage variation on the resonant converter operation in the maximum output power condition ($P_{out} = 3kW$), (a) $V_{in} = 360VDC$, and $V'_{bat} = 120VDC$, (b) $V_{in} = 360VDC$, $V'_{bat} = 180VDC$, (c) $V_{in} = 440VDC$, $V'_{bat} = 120VDC$, and (d) $V_{in} = 440VDC$, $V'_{bat} = 180VDC$.

soft switching conditions.

In order to examine the performance of the resonant converter with the proposed mod-

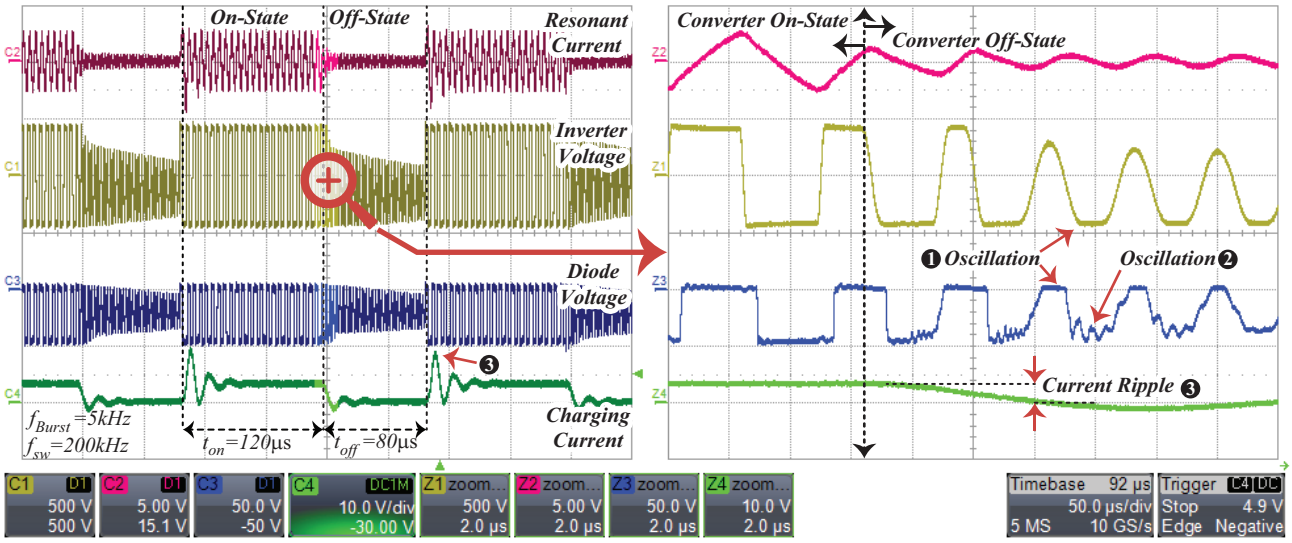

Figure 2.17: The burst mode issues in the full bridge LLC resonant converter for the $V'_{bat} = 45VDC$ and $I'_{bat} = 2A$ recovery region. ① High frequency, high voltage oscillation across inverter output nodes and output rectifier diodes caused by the interaction between MOSFET Drain-Source capacitances and the resonant circuit, ② High frequency oscillation caused by the interaction between output rectifier diodes junction capacitances and the resonant circuit. ③ Output current variation and spikes, which lead to unwanted tripping in recovery mode and interfere with the BMS current sensing circuit.

ulation technique, the prototype platform has been tested in the recovery region. One of the main advantages of the LLC resonant converter is the output filter type, which consists only of a capacitor. According to Table 2.4, the output filter consists of an $18uF$ film capacitor and can perfectly provide a ripple free charging current for the battery pack in normal switching operation ($f_s = 100 \sim 200kHz$). But in the burst mode modulation, the switching driver signals are turned on and off periodically with an intermittent cycle much lower than the minimum switching frequency ($f_{Burst} = 5kHz$). When revitalizing a dead battery, the battery absorbs current while the output filter, which is designed for minimum switching frequency operation ($f_s = 100kHz$), cannot absorb the current ripple of the burst mode cycle. As a result, the battery charger operation in this mode leads to a low quality charging current, and the battery pack is charged with a burst frequency current ripple that can reduce the battery's life span. In order to show the drawback of the burst mode mod-

ulation strategy, experimental results are presented to show the amount of charging current ripple in both Burst and Phase Shift modulations. The experimental results in Fig. 2.17 show the detrimental effect of using the full bridge LLC resonant converter in burst mode and in the 0.6 duty cycle. In Fig. 2.17, the battery voltage and current are set to 45VDC and 2ADC. According to Fig. 2.17, the battery current variation alternates between 0 and 4.2A. Also, there is a spike in the current up to 8A during the transient time as a result of the interaction between output filter capacitor and the parasitic inductance of the charger cable. The pulsating current and spikes lead to unwanted tripping in recovery mode and interfere with the BMS current sensing circuit. In order to reduce the charging current ripple in the burst mode operation, it is essential to install additional LC filters in the output of the DC-DC stage, meaning higher cost and lower power density. Also, adding extra filters to the current sensing circuit is vital. As can be seen in Fig. 2.17, due to the interaction between parasitic capacitances (including MOSFET Drain-Source and diodes junction) and the resonant circuit elements, there is high frequency, high voltage oscillation in different points of the circuit, which results in a noisy environment for the BMS. Fig. 2.18 presents the experimental result for the LLC resonant converter when it operates in Phase Shift modulation mode with the same battery voltage and current as assumed for Fig. 2.17. According to Fig. 2.18, there is no ripple in the battery charging current, which proves the capability of the proposed modulation strategy in terms of working in recovery region. All in all, the proposed Phase Shift modulation technique can provide ripple-free charging current without requiring any additional filters in the output of the converter, thereby providing a noise-free environment for the reliable operation of the BMS.

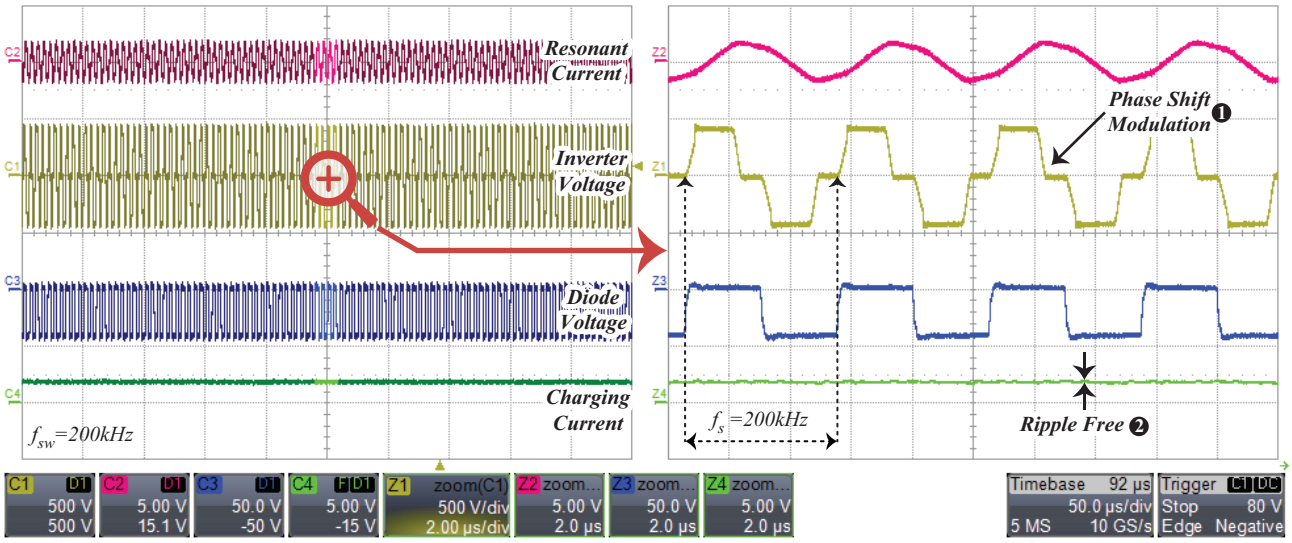

Figure 2.18: The experimental result of the proposed modulation technique for the $V'_{bat} = 45VDC$ and $I'_{bat} = 2A$ recovery region. ① indicates the phase shift strategy, which is applied in the recovery region for wider regulation. ② shows the smooth charging current without any ripple.

2.6 Summary

This chapter introduced a modified *LLC* resonant topology driven by both Variable Frequency (VF) and Phase Shift (PS) to achieve all the regulation requirements for high power battery charging. The main advantage of the *LLC* resonant converter with the proposed modulation strategy is its ability to regulate the output voltage from close to zero up to 1.5 times the nominal voltage in continuous conduction mode with low switching frequency variation, while providing soft switching conditions for semiconductor devices. The low-ripple voltage enhanced the quality of the charging current for battery charger applications in all conditions, especially the recovery region, thereby providing a noise-free environment for the reliable operation of a Battery Management System. The experimental results proved that the modified *LLC* resonant converter with this special modulation strategy covered almost all regions in the V-I plane, and had a peak efficiency of 96.5%. As presented in Section 2.3, the optimum design procedure of the modified *LLC* resonant converter for battery charger

applications is not straightforward, and always a trade-off exists between maximum output voltage regulation and other characteristics (e.g. efficiency), which necessitates using a special tool (e.g. DoE methodology) for optimization. It means the modified LLC resonant converter needs more efforts in terms of an optimum design, when comparison with PWM-type converters is taken into account. Even though modified LLC resonant converter has two more elements in its topology in comparison with PSFB (a resonant inductor and a resonant capacitor), it has a higher efficiency in comparison with PSFB which leads to a smaller cooling system. It is necessary to mention due to the high amplitude of the resonant circuit current, the series resonant capacitor has to withstand a high frequency, high amplitude voltage, which leads to an expensive film-type capacitor selection.

Chapter 3

Improving the Regulation Range of EV Battery Chargers with $L3C2$ Resonant Converters[3]

In the previous chapter, a modified special LLC tank driven by both Variable Frequency (VF) and Phase Shift (PS) was introduced as a solution to achieve all the regulation requirements for high power battery charger applications. Since the topology employs a full bridge inverter, it is more appropriate for high power applications (several kW), rather than medium power level (around $1kW$). Generally a half bridge inverter is selected for medium power levels due to having fewer elements and lower cost in comparison with full bridge inverters. In the case of half bridge inverter it is not possible to employ Phase Shift modulation strategy for wide regulation. The main aim of this chapter is to introduce a multi-resonant $L3C2$ resonant converter for medium level power applications that can cover nearly all of the regions in the battery V-I plane from near zero output voltage, zero output current to maximum output power. First, the complete analysis of the $L3C2$ resonant converter with consideration of transformer primary and secondary leakage inductances, transformer secondary winding capacitance, and output rectifier junction capacitances is obtained. Next, Design of Experiment methodology along with Design-Expert Software is employed in order to optimize the design procedure of the battery charger [98, 109]. Later, a complete set of

[3]Portions of this chapter have been published in [3, 4]

simulation and experimental results, extracted from a 96VDC, 950W $L3C2$ resonant converter is presented in order to present the characteristic features of the proposed topology for battery charger applications while providing a comparative example with the LLC topology.

3.1 Comparison of $L3C2$ and LLC Resonant Topologies

The main problem regarding LLC resonant converters for wide output voltage regulation was presented in Chapter 2 and will be reviewed briefly. Fig. 3.1(a) presents the half bridge LLC resonant converter schematic with a non-ideal transformer. In Fig. 3.1(b) the normalized voltage gains of the half-bridge LLC resonant converter versus frequency have been drawn with consideration to the parasitic capacitances. According to Fig. 3.1(b), the parasitic capacitances lead to a second resonant frequency in the voltage gains, which is far from the short circuit resonant frequency ($f_{r,sc}$). The value of second resonant frequency depends on the equivalent parasitic capacitance in the secondary side of the transformer and cannot be estimated easily. Consequently, beside the capacitive load region (in gray), there is a second non-operating area for the LLC resonant converter as indicated by red dashed regions. In this case the parasitics capacitors limit the output voltage regulation. Fig 3.1(c) illustrates the maximum VI-plane coverage of the LLC resonant converter including the normal and recovery charging area, in continuous conduction mode [25]. The red dashed region in Fig. 3.1(c) indicates the unobtainable area in the V-I plane, where the switching frequency restriction leads to the regulation issue for the LLC resonant converter.

In comparison with an LLC resonant converter, higher order resonant converters present more desirable characteristics, such as the ability to absorb parasitic inductances and capacitances of the elements and circuit effectively, employing them as resonant elements. Moreover,

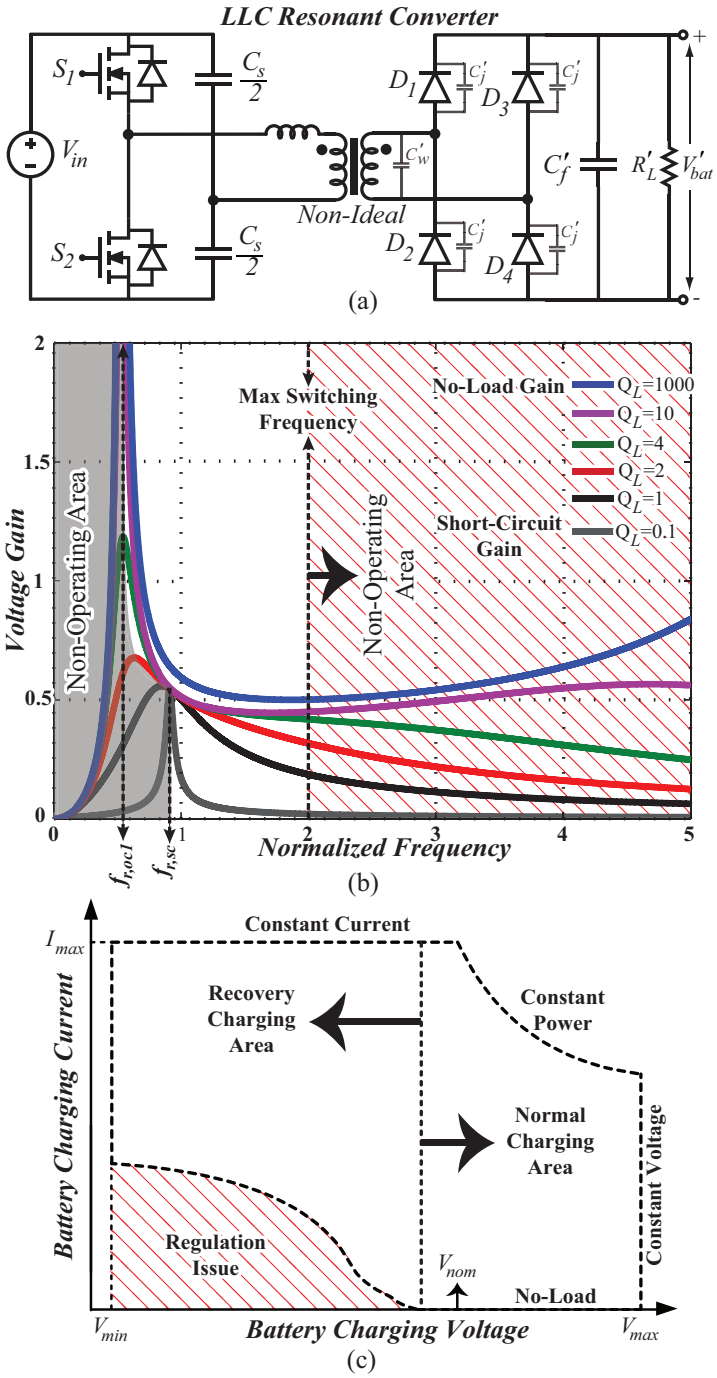

Figure 3.1: *LLC* resonant topology: (a) *LLC* schematic including parasitic capacitances, (b) *LLC* voltage gain issues (high frequency) due to the rectifier junction capacitances, and (c) *LLC* V-I plane highlighting regulation issues.

the diversity of elements in higher order resonant converters gives designers more freedom in the design procedure [112, 113]. The proposed resonant strategy using an $L3C2$ structure is shown in Fig. 3.2(a). The proposed multi-resonant charger consists of a half-bridge inverter, a resonant circuit (including external inductor, non-ideal transformer, and parallel capacitor), and a bridge rectifier with capacitive output filter. By adding a parallel capacitor, the topology is able to extend the operating frequency beyond the LLC topology and achieve significant regulation improvements. This parallel resonant capacitor put in the secondary side of the transformer is significantly higher than parasitic capacitors (grey capacitor, C'_w and C'_j), and therefore overwhelms them and makes the diode junction and winding capacitances insignificant. The typical voltage gain curves and V-I plane of the half-bridge $L3C2$ resonant converter is presented in Fig. 3.2(b)-(c). According to Fig. 3.2(b)-(c), the existence of the parallel resonant capacitor leads to a second resonant frequency in the voltage gains and, as a result, it is feasible to regulate the output voltage in a wide range, from near zero to more than nominal output voltage, by employing variable frequency method. In the following, the complete set of equations for the steady state analysis of the $L3C2$ resonant converter is presented. In order to compare the performances between LLC and $L3C2$ resonant converters, half-bridge inverters, split series resonant capacitors, and bridge rectifiers with pure capacitive output filters have been selected for both $L3C2$ and LLC resonant converters.

3.2 Multi-Resonant $L3C2$ Resonant Converter with a Non-Ideal Transformer

Fig. 3.3 shows a complete schematic of the $L3C2$ resonant converter including relevant parasitics. In Fig. 3.3, a fourth order model of the transformer (including primary and secondary leakage inductances, magnetizing inductance, and winding capacitance of the transformer

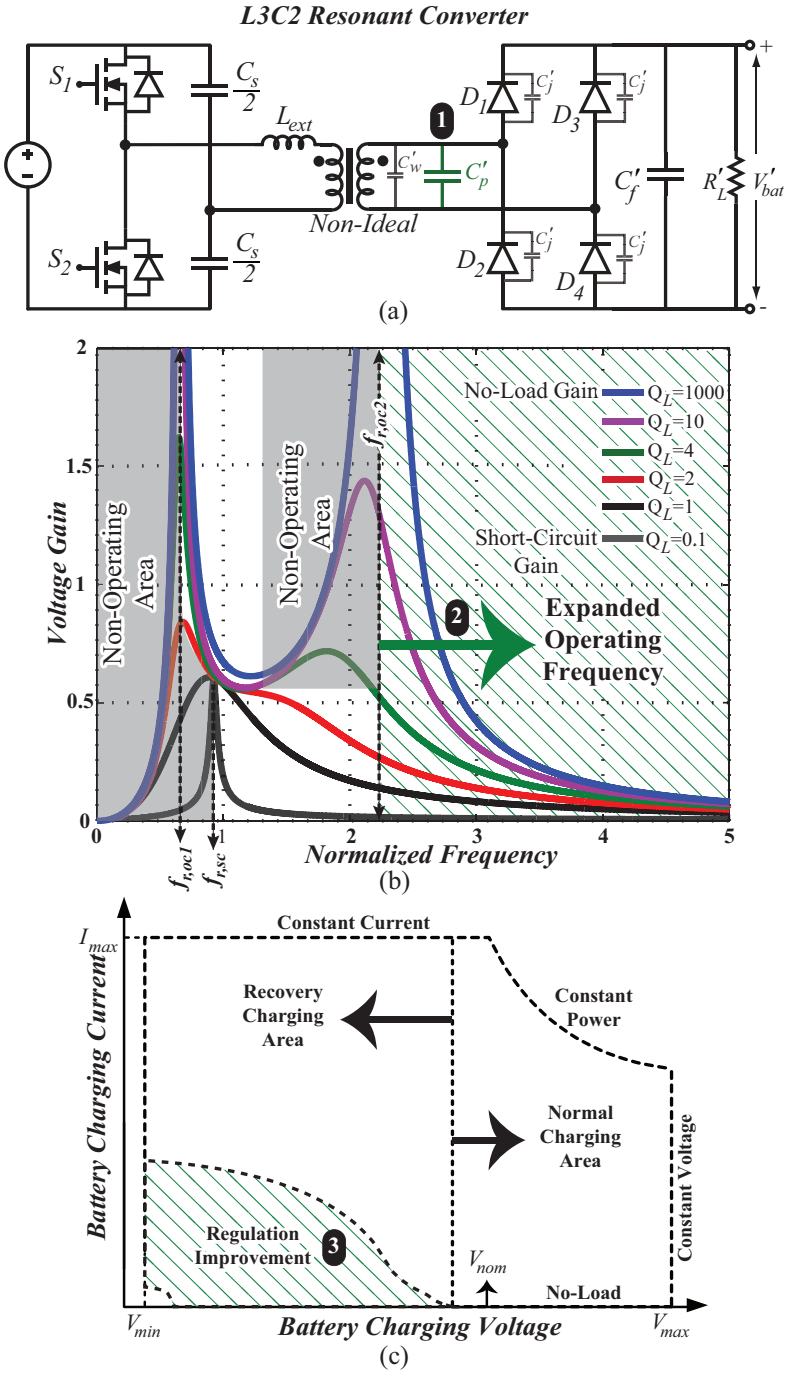

Figure 3.2: Proposed $L3C2$ resonant topology solution: (a) $L3C2$ schematic with parallel resonant capacitor in the transformer secondary side ①, (b) $L3C2$ voltage gains with expanded switching frequency operation ②, and (c) $L3C2$ V-I plane coverage showing significant regulation improvement ③.

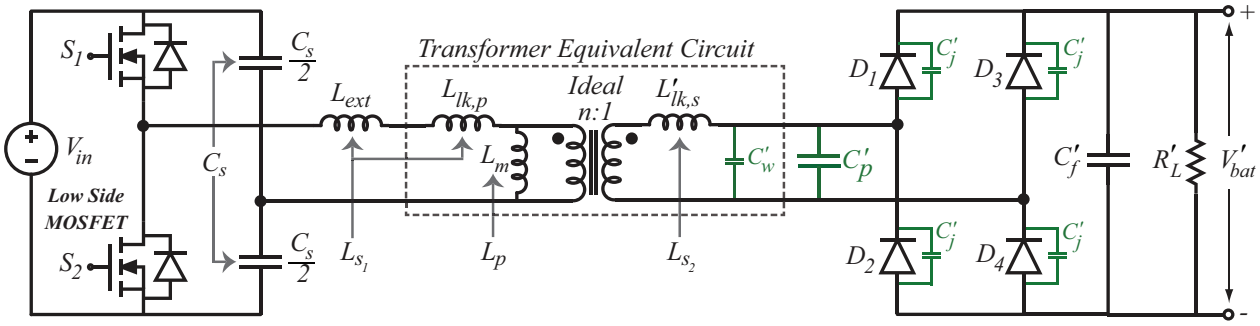

Figure 3.3: $L3C2$ resonant converter with non-ideal transformer.

secondary side) has been employed as a model for the non-ideal transformer [105]. The junction capacitances of the output rectifier are considered in parallel with the diodes. According to Fig. 3.3, the parallel resonant capacitor in the transformer secondary side can integrate parasitic capacitances into the resonant circuit (green capacitors). As depicted in Fig. 3.3, secondary leakage and the magnetizing inductances of the transformer are considered L_{s_2} and L_p, respectively. In addition, primary leakage inductance is merged with the external inductor and is part of L_{s_1}. In Fig. 3.3, all of the elements in the secondary side are defined with an apostrophe, but in all the equations, the variables and elements are transferred to the primary side with respect to the transformer turns-ratio, and are shown without an apostrophe. Different states of the output rectifier along with C_t and its main waveforms are presented in Fig. 3.4(a) and (b), respectively. In Fig. 3.4(a), the C_t is defined as follows:

$$C_t = C_w + C_p + C_j \tag{3.1}$$

Since there is no inductor at the output of the converter, in the off-state interval of the output rectifier, C_t is disconnected from the output filter, charged and discharged by $i_{L_{s_2}}$, and v_{C_t} has a semi-sinusoidal shape. The C_t voltage is clamped to the output voltage level while the output rectifier is on, and power is transferred from the resonant circuit to the output.

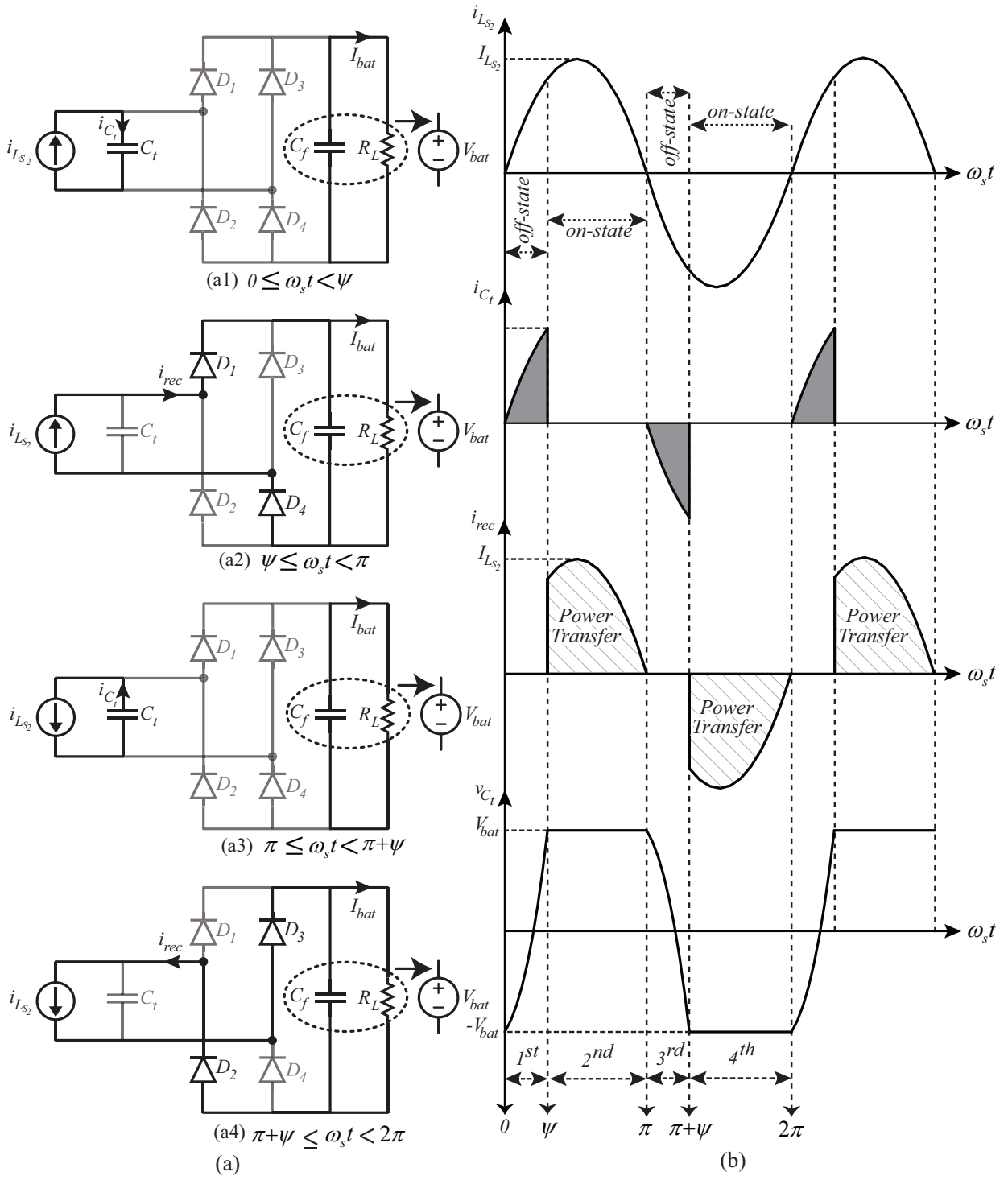

Figure 3.4: (a) Output rectifier states along with parallel resonant capacitor, and (b) Main waveforms of the output rectifier.

Due to the semi-sinusoidal waveform of the diode voltage, the diodes turn on at zero voltage and turn off at zero current (soft switching condition); therefore, the drawback effect of the diode junction capacitance in transient time can be minimized. Also, the existence of parallel resonant capacitor with rectifier input port leads to ZCS of the diodes and reduces the EMI noise [114–116]. There are four states for the output rectifier in each switching period, and all of them are illustrated in Fig. 3.4(a). According to Fig. 3.4(b), the rectifier input current is not purely sinusoidal and the rectifier input voltage has a semi-sinusoidal shape. As a result, the output rectifier and load cannot be simply modeled by an equivalent impedance. In [117], an equivalent circuit has been obtained for the output rectifier in parallel and series-parallel resonant converters with capacitive output filters. In fact, a resistive impedance in series with a capacitive impedance is used to model the circuit in Fig. 3.4(a). The elements of the equivalent circuit are defined as follows [117]:

$$R_{eq} = \frac{\sin^2 \psi}{\pi C_t \omega_s} \tag{3.2}$$

$$C_{eq} = \frac{\pi C_t}{\psi - \sin \psi \cos \psi} \tag{3.3}$$

In the above equations, the off-state interval, ψ is called non-conduction mode and is given by:

$$\psi = \cos^{-1}\left(\frac{\pi - 2\omega_s R_L C_p}{\pi + 2\omega_s R_L C_p}\right) \tag{3.4}$$

By using the equivalent circuit of Fig. 3.4(a), it is possible to employ the FHA technique for analysis of the $L3C2$ resonant circuit. In FHA analysis, it is assumed that power is only transferred from the high frequency resonant circuit to the load via the fundamental component. The AC equivalent circuit of the $L3C2$ resonant converter with capacitive output

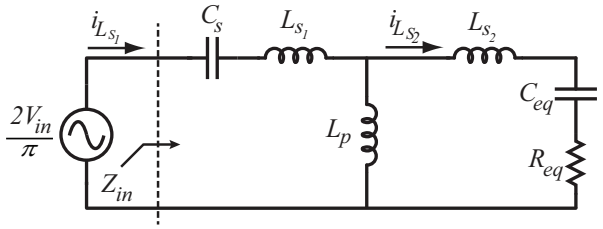

Figure 3.5: AC equivalent circuit of the $L3C2$ resonant converter.

filter is presented in Fig. 3.5. The output voltage of the half-bridge inverter is a square wave with magnitude of V_{in}. This voltage can be expanded in Fourier Series, and the fundamental component can be expressed as follows:

$$v_1 = V_1 \sin(\omega_s t), V_1 = \frac{2V_{in}}{\pi} \tag{3.5}$$

In the following, the AC equivalent circuit is analyzed to extract the steady-state equations of the $L3C2$ resonant converter. In Fig. 3.5, the input impedance of the resonant circuit is obtained as follows:

$$\begin{aligned} &\mathbf{Z_{in}}(j\omega_s) = |\mathbf{Z_{in}}|\, e^{j\varphi} = \\ &\frac{1}{j\omega_s C_s} + j\omega_s L_{s_1} + (j\omega_s L_p)||(j\omega_s L_{s_2} + R_{eq} + \frac{1}{j\omega_s C_{eq}}) \end{aligned} \tag{3.6}$$

In Eq. (3.6), φ indicates the phase of the input impedance. As mentioned previously, φ should be kept positive in all operating conditions in order to provide soft switching for power MOSFETs. Using the normalized parameters, the normalized input impedance $\frac{Z_{in}}{Z_0}$ and ψ are derived as follows:

$$Q_L = \frac{R_L}{Z_0}, Z_0 = \sqrt{\frac{L_{s_1}}{C_s}}, \omega_0 = \frac{1}{\sqrt{L_{s_1} C_s}}, \omega_n = \frac{\omega_s}{\omega_0} \tag{3.7}$$

$$\frac{\mathbf{Z_{in}}(j\omega_n)}{Z_0} = \\ (j\omega_n + \frac{1}{j\omega_n}) + \frac{\frac{j\omega_n}{L_n}(\frac{j\omega_n}{L_s} + \frac{\sin^2\psi}{\pi C_n\omega_n} + \frac{\psi-\sin\psi\cos\psi}{\pi C_n j\omega_n})}{\frac{j\omega_n}{L_n} + \frac{j\omega_n}{L_s} + \frac{\sin^2\psi}{\pi C_n\omega_n} + \frac{\psi-\sin\psi\cos\psi}{\pi C_n j\omega_n}} \tag{3.8}$$

$$\psi = \cos^{-1}\frac{\pi - 2C_nQ_L\omega_n}{\pi + 2C_nQ_L\omega_n} \tag{3.9}$$

According to Fig. 3.5 and Eqs. (3.5) and (3.8), the amplitude of $I_{L_{s_1}}$ (MOSFETs current) can be obtained as follows:

$$I_{L_{s1}} = \frac{2V_{in}}{\pi|\mathbf{Z_{in}}(j\omega_n)|} \tag{3.10}$$

In order to calculate the output current, the second resonant inductor current is considered purely sinusoidal with the following equation:

$$i_{L_{s_2}} = I_{L_{s_2}}\sin(\omega_s t + \theta) \tag{3.11}$$

and as a result, according to Fig. 3.4, the output current and output voltage are given by:

$$I_{bat} = \frac{1}{2\pi}(\int_{\psi}^{\pi} \mathrm{i_{L_{s_2}}}\,\mathrm{d}(\omega_s t) + \int_{\pi+\psi}^{2\pi} \mathrm{i_{L_{s_2}}}\,\mathrm{d}(\omega_s t)) = \frac{(1+\cos\psi)}{\pi} I_{L_{s_2}} \tag{3.12}$$

$$I_{L_{s2}} = \left|\frac{\frac{j\omega_n}{L_n}}{\frac{j\omega_n}{L_n} + \frac{j\omega_n}{L_s} + \frac{\sin^2\psi}{\pi C_n\omega_n} + \frac{\psi-\sin\psi\cos\psi}{\pi C_n j\omega_n}}\right| I_{L_{s_1}} \tag{3.13}$$

$$V_{bat} = R_L.I_{bat} = R_L\frac{(1+\cos\psi)}{\pi} I_{L_{s_2}} \tag{3.14}$$

The normalized voltage transfer function of the half-bridge $L3C2$ resonant converter with capacitive output filter is calculated as follows:

$$M_v = \frac{V_{bat}}{V_{in}} = \frac{Q_L Z_0 (1 + \cos\psi) I_{L_{s_2}}}{\pi V_{in}} \tag{3.15}$$

Fig. 3.5 and Eqs. (3.8)-(3.15) can be employed to analyze the steady-state behaviour of the $L3C2$ resonant converter with capacitive output filter. The input impedance of the resonant circuit can be defined by Eq. (3.8). Eq. (3.10) shows the current amplitude passing through resonant circuit. Also Eq. (3.15) presents the voltage gain of the whole converter (including the half bridge inverter, resonant circuit, and output rectifier), from the input voltage source to the output side.

3.3 Resonant Frequencies of the $L3C2$ Topology

It is crucial that the resonant circuit represents an inductive load, and that the current of the input resonant circuit lags the output voltage of the half-bridge inverter. This means the input impedance phase, φ, must be positive in all operating conditions. According to Fig. 3.1(b), ZVS conditions for the LLC resonant converter is guaranteed if the switching frequency is greater than the load resonant frequency. The lowest resonant frequency occurs for no-load conditions ($Q_L \rightarrow \infty$) and is labeled as $f_{r,oc1}$. However, the LLC resonant converter can not operate in high frequency due to the diodes' parasitic capacitances in the secondary of the transformer. In the $L3C2$ resonant converter, there are two resonant frequencies for high Q_L and, as a result, two non-operating regions are imposed. According to Fig. 3.2(b), the first non-operating area is similar to that of the LLC resonant circuit. The second is after the short circuit resonant frequency and just before the second open circuit resonant frequency ($f_{r,oc2}$). In fact, in this region the resonant circuit represents a capacitive load for high loaded quality factor, and the control circuit must be prevented from

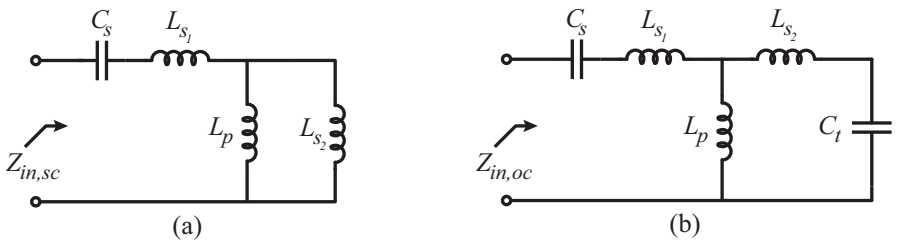

Figure 3.6: The equivalent circuit of the $L3C2$: (a) Output short circuit condition, (b) Output open circuit condition.

entering this region. Increasing the switching frequency above $f_{r,oc2}$ presents wide output voltage regulation for the $L3C2$ resonant converter, which is unobtainable for the LLC. In this section, the resonant frequencies of the $L3C2$ resonant circuit will be determined as a function of normalized parameters.

3.3.1 Short Circuit Resonant Frequency

In short circuit conditions, the value of output load tends to zero ($Q_L \to 0$) and the non-conduction angle is calculated as follows:

$$\psi = \lim_{Q_L \to 0} \cos^{-1} \frac{\pi - 2C_n Q_L \omega_n}{\pi + 2C_n Q_L \omega_n} = 0 \tag{3.16}$$

As a result, R_{eq} and C_{eq} are equal to zero and the AC equivalent circuit of the $L3C2$ resonant converter is changed. See Fig. 3.6(a). Using the normalized parameters presented in Eq. 3.7, the input impedance of Fig. 3.6(a) is given by:

$$Z_{in,sc}(j\omega_s) = \frac{1}{j\omega_s C_s} + j\omega_s L_{s_1} + (j\omega_s L_p) || j\omega_s L_{s_2} \tag{3.17}$$

$$\frac{Z_{in,sc}(j\omega_n)}{Z_0} = \frac{1 - (1 + \frac{1}{L_n + L_s})\omega_n^2}{j(\frac{1}{L_n} + \frac{1}{L_s})\omega_n} \tag{3.18}$$

and the short circuit resonant frequency, $f_{r,sc}$ is given by the following:

$$\frac{\omega_{r,sc}}{\omega_0} = \frac{1}{\sqrt{1+\frac{1}{L_n+L_s}}} \tag{3.19}$$

3.3.2 Open Circuit Resonant Frequency

In open circuit conditions ($Q_L \to \infty$) the non-conduction angle and equivalent elements are obtained as follows:

$$\psi = \lim_{Q_L\to\infty} \cos^{-1}\frac{\pi - 2C_nQ_L\omega_n}{\pi + 2C_nQ_L\omega_n} = \pi \implies R_{eq} = 0 \;\&\; C_{eq} = C_t \tag{3.20}$$

Fig. 3.6(b) shows the AC equivalent circuit of the $L3C2$ resonant converter in no-load conditions. Therefore, the input impedance of this circuit is given as follows:

$$Z_{in,oc}(j\omega_s) = \frac{1}{j\omega_s C_s} + j\omega_s L_{s_1} + (j\omega_s L_p)||(j\omega_s L_{s_2} + \frac{1}{j\omega_s C_t}) \tag{3.21}$$

$$\frac{Z_{in,oc}(j\omega_n)}{Z_0} = \frac{(\frac{C_n}{L_n}+\frac{C_n}{L_s}+\frac{C_n}{L_nL_s})\omega_n^4 - (\frac{C_n}{L_n}+\frac{C_n}{L_s}+\frac{1}{L_n}+1)\omega_n^2 + 1}{j(1-(\frac{1}{L_n}+\frac{1}{L_s})\omega_n^2)\omega_n} \tag{3.22}$$

As presented in Fig. 3.2(b), there are two open circuit resonant frequencies in the $L3C2$ resonant circuit and the final equations are presented as follows.

$$\frac{\omega_{r,oc1}}{\omega_0} = \sqrt{\frac{\frac{C_n}{L_n}+\frac{C_n}{L_s}+\frac{1}{L_n}+1 - \sqrt{(\frac{C_n}{L_n}+\frac{C_n}{L_s}+\frac{1}{L_n}+1)^2 - 4(\frac{C_n}{L_n}+\frac{C_n}{L_s}+\frac{C_n}{L_nL_s})}}{2(\frac{C_n}{L_n}+\frac{C_n}{L_s}+\frac{C_n}{L_nL_s})}} \tag{3.23}$$

$$\frac{\omega_{r,oc2}}{\omega_0} = \sqrt{\sqrt{\frac{\frac{C_n}{L_n}+\frac{C_n}{L_s}+\frac{1}{L_n}+1+\sqrt{(\frac{C_n}{L_n}+\frac{C_n}{L_s}+\frac{1}{L_n}+1)^2-4(\frac{C_n}{L_n}+\frac{C_n}{L_s}+\frac{C_n}{L_nL_s})}}{2(\frac{C_n}{L_n}+\frac{C_n}{L_s}+\frac{C_n}{L_nL_s})}}} \tag{3.24}$$

As presented in Fig. 3.2(b), the fifth order $L3C2$ resonant converter has one more open resonant frequency in comparison with the LLC resonant converter. The obtained equations for the open circuit resonant frequencies are useful to determine how far the $L3C2$ can expand the operating frequency over the LLC converter.

3.4 Secondary Leakage Inductance Effect on the $L3C2$ Resonant Converter

In order to analyze converters, transformers are typically modeled by an equivalent circuit based on the operating frequency of the converter and transformer configuration. Fig. 3.7 presents different standard equivalent circuits of the transformer that have been used in the literature for converters analysis [105, 118–123]. Employing an interleaved structure for the windings leads to high coupling between primary and secondary and as a result the lowest amount of leakage inductance obtains, which means the first or second order model of the transformer can be used (Fig. 3.7(a) and (b)) [118–120]. On the other hand, applying a sectional bobbin with an air gap between core halves leads to less coupling between windings and increases leakage inductance in both primary and secondary sides of the transformer, which is desirable in resonant converters to integrate the series resonant inductance into the transformer (Fig. 3.7(c)). This model is widely used for analysis of resonant converters [121, 122]. In this work, due to the wide operating frequency, the fourth-order equivalent circuit of the transformer, as shown in Fig. 3.7(d), is adopted to accurately analyze the

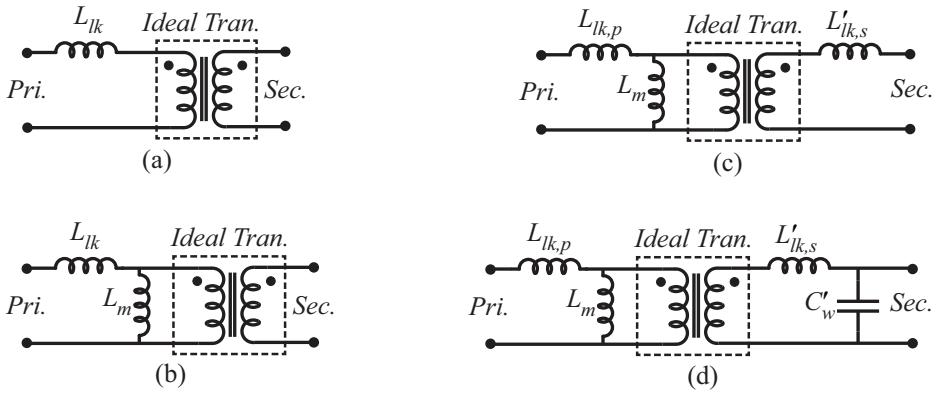

Figure 3.7: Transformer models, (a) First order, (b) Second order, (c) Third order, and (d) Fourth order.

converter. This equivalent circuit takes into account the effects of the primary and the secondary leakage inductance separately. Also, the magnetizing inductance and the secondary winding capacitance are incorporated in this equivalent circuit [105, 123].

Beside the more accurate steady state analysis, which is derived in this work, the transformer secondary leakage inductance plays an important role in the required switching frequency range of the $L3C2$ resonant converter. Fig. 3.8 shows the effect of secondary leakage inductance on the voltage gains of the $L3C2$ resonant converter. According to Fig. 3.8, a high amount of secondary leakage inductance (low value of L_s) leads to moving the second resonant frequency closer to the first one and, therefore, a wide output voltage regulation is obtainable. In other words, for the proposed resonant converter with low secondary leakage inductance, switching frequency needs to increase more in comparison with high secondary leakage inductance for getting the same output voltage regulation.

3.5 Design of Experiment Methodology (DoE)

The optimized selection of normalized parameters should be performed according to the application requirements. Similar to previous chapter, the Design of Experiment (DoE)

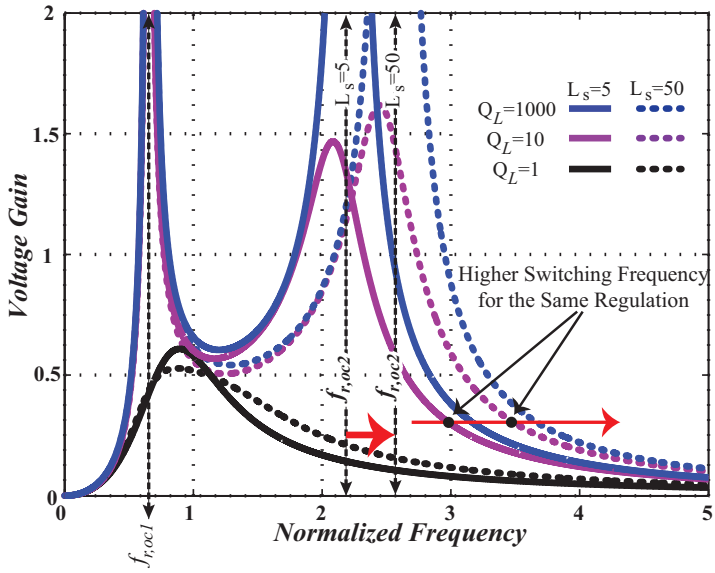

Figure 3.8: The effect of secondary leakage inductance on the voltage gain curves.

methodology is employed to consider the behaviour of both resonant converters when responding to variations in different normalized parameters. According to the steady-state analysis performed in Sections 2.1 and 3.2, the equations obtained for LLC and $L3C2$ resonant converter are functions of three and four normalized variables, respectively. The output response surfaces of DoE have been selected based on the most important attributes for a battery charger application, which are high efficiency and a wide output voltage converter. In the following subsections, these attributes will be discussed in detail.

3.5.1 Minimum Obtainable Output Voltage

To respond to different charging algorithms, the charger should regulate the output voltage from near zero up to 1.5 times the nominal voltage. As a result, the maximum output voltage regulation is the most important attribute that should be considered. According to Figs. 3.1 and 3.2, the voltage gain curves are not the same in the LLC and $L3C2$ resonant converters, and because of this, two different criteria are introduced for output voltage regulation. The output response surfaces are based on the optimization of the following criteria:

$$\begin{cases} \left| \frac{\partial M_v}{\partial f_n}\Big|_{f_n=f_{r,sc}} \right| \rightarrow Maximize & \text{for } LLC \\ \frac{V_{bat,min,NL}}{V_{bat,n}} \rightarrow Minimize & \text{for } L3C2 \end{cases} \tag{3.25}$$

According to Eq. 3.25 and Fig. 3.1, the LLC voltage gain curves can approach nearly zero voltage in high frequency when the absolute value of the gain curves' slope at the short circuit resonant frequency is set to be maximized. For the $L3C2$ resonant converter, the ratio between minimum battery voltage in no-load condition (maximum switching frequency) and nominal battery voltage is calculated.

3.5.2 Resonant Circuit Current

In order to attain high efficiency in part load condition, the difference between input resonant circuit current in nominal and no-load condition should be maximized. In other words, the lesser circulating current, the greater part load efficiency. Eq. 3.26 presents the second output of DoE that should be maximized.

$$\frac{I_{L_{s1},FL}}{I_{L_{s1},NL}} \rightarrow Maximize \tag{3.26}$$

3.5.3 Soft Switching Operating Condition

In order to provide soft switching conditions for the power MOSFETs, the phase angle of input impedance should be positive. Ideally, it is preferred to have this angle be equal to zero, but due to charging and discharging of the MOSFETs' output capacitances, a minimum lagging phase is required (calculated by Eq. 2.15). On the other hand, if this angle is too steep in the nominal load condition, the current stress on semiconductor devices and other passive elements will be increased. In other words, the cosine of the input impedance phase for the resonant circuit has a reverse relation with the amplitude of the resonant circuit

Table 3.1: Normalized Parameters Range and Selected Value

Parameter	*LLC*		*L3C2*	
	Range	*Selected*	*Range*	*Selected*
L_n	$[0.2 - 0.8]$	0.4	$[0.25 - 1.25]$	0.9
L_s	$[3 - 10]$	4.4	$[3 - 10]$	4.7
C_n	NA	NA	$[0.1 - 0.5]$	0.3
Q_L	$[0.5 - 1.5]$	1	$[0.5 - 1.5]$	1

current. It means higher input impedance phase leads to more current circulating in the resonant circuit. Eq. 3.27 presents the range of input impedance phases that the output response of DoE should fall within.

$$\begin{cases} \varphi > 10^\circ & \text{for practical margin} \\ \varphi < 30^\circ & \text{for high efficiency achievement} \end{cases} \tag{3.27}$$

In the following paragraphs, the output response surfaces of DoE will be considered. Table 3.1 presents the range for normalized parameters, which will be used as the input range of normalized parameters in DoE. The performance of carefully selected data points within these ranges of factors have been investigated for the $L3C2$ and LLC resonant converters. The $L3C2$ requires 25 simulations to cover the effects of 4 normalized parameters, while the LLC converter used 15 points to study the impact of 3 normalized parameters. Significance testing was combined with ANOVA regression to develop 3D response surfaces for each of the 3 main attributes listed above [109, 110]. The response surfaces for LLC and $L3C2$ resonant converters have been presented in Figs. 3.9 and 3.10, respectively. It is necessary to mention that each surface response has been drawn based on the two normalized parameters that have the most impact on the surface.

It is possible to select normalized parameters for each resonant converter by considering

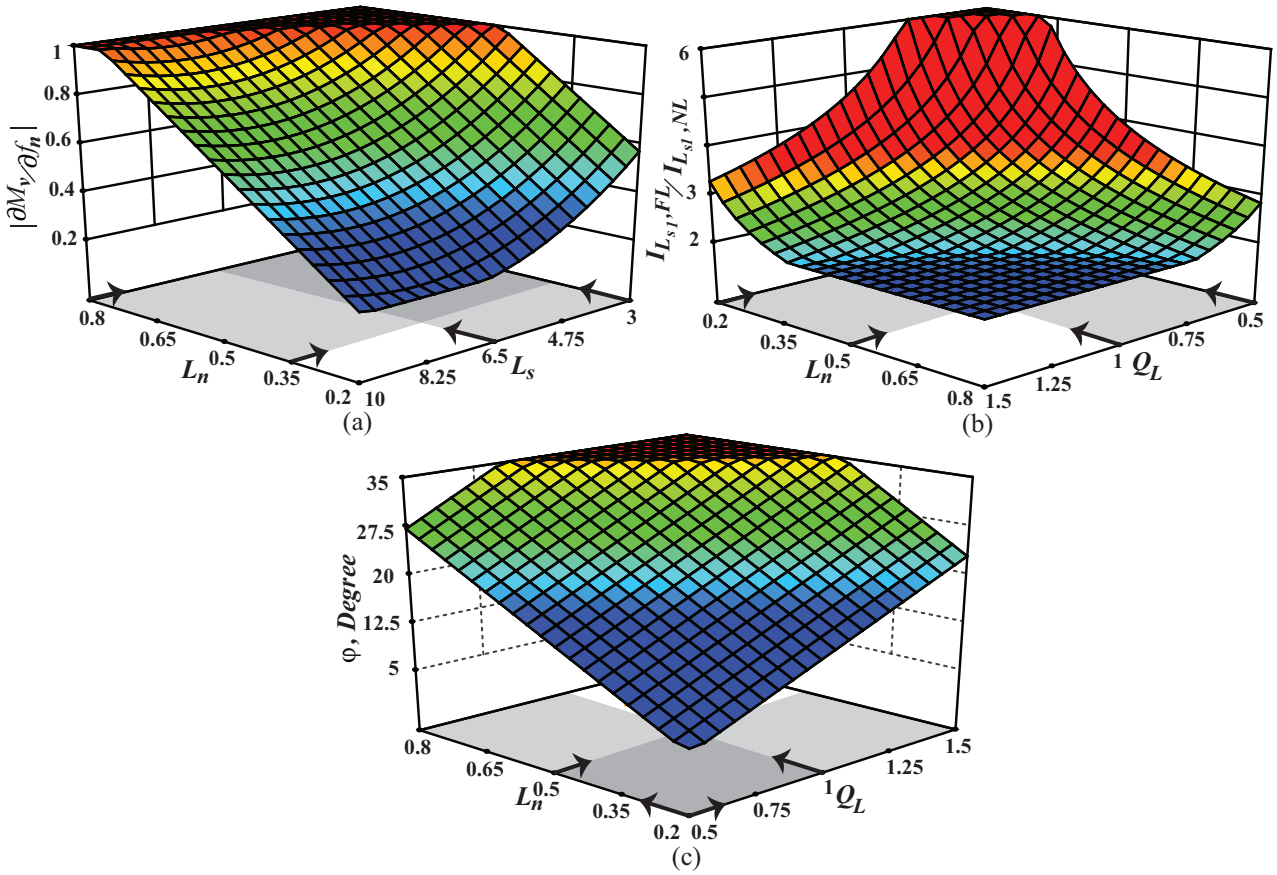

Figure 3.9: DoE response surfaces for LLC resonant converter: (a) Voltage gain slope surface versus L_n and L_s, (b) Input resonant circuit current ratio versus L_n and Q_L, and (c) Phase of the input impedance versus L_n and Q_L.

the different response surfaces at the same time. The selection of normalized parameter is similar to that discussed in Section 2.3. According to Fig. 3.9(a), in order to satisfy Eq. 3.25, the L_n and L_s should be, respectively, at the highest and lowest possible levels. Two ranges can be defined for normalized parameters (gray band), and the points located in the common area (dark gray) are candidates for optimum L_n and L_s parameters. The same concept can be applied to other surfaces of Fig. 3.9 with respect to Eqs. 3.26 and 3.27, and finally, the intersection between different common areas determines the values of normalized parameters. The same routine has been employed in order to select the normalized value of the $L3C2$ resonant converter. The final values of the normalized parameters have

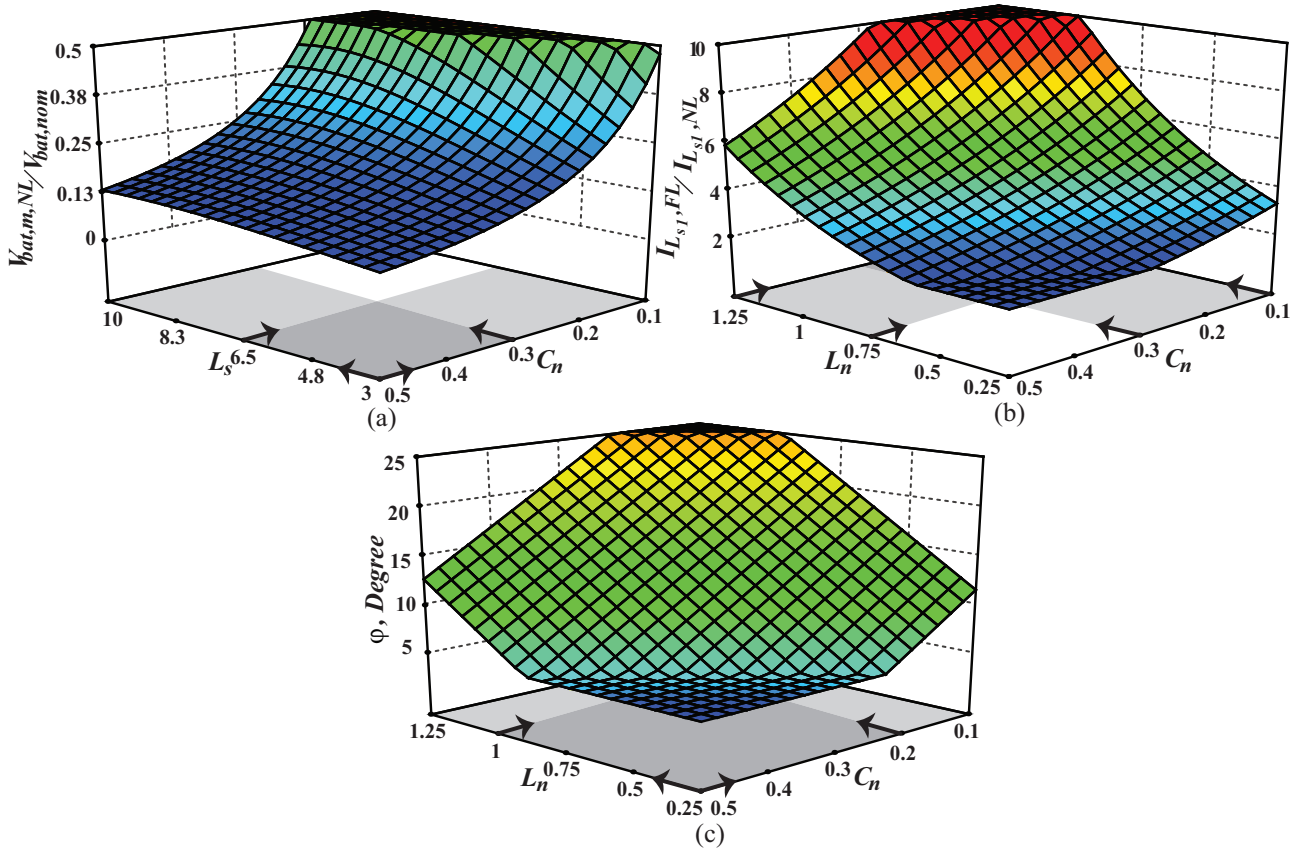

Figure 3.10: DoE response surfaces for $L3C2$ resonant converter: (a) Voltage gain ratio surface versus L_s and C_n, (b) Input resonant circuit current ratio versus L_n and C_n, and (c) Phase of the input impedance versus L_n and C_n.

been selected after conducting simulations and taking into account practical considerations, especially the amount of secondary leakage inductance. According to Figs. 3.9(a) and 3.10(a), secondary leakage inductance on both resonant converters under consideration has a positive effect on output voltage regulation. This means that a high amount of secondary leakage inductance (low value of L_s) can expand the output voltage regulation.

3.6 Resonant Converters Design

In this section, based on the optimized selection of normalized parameters, the voltage gain curves of the resonant converter will be used to design two power converters with the same

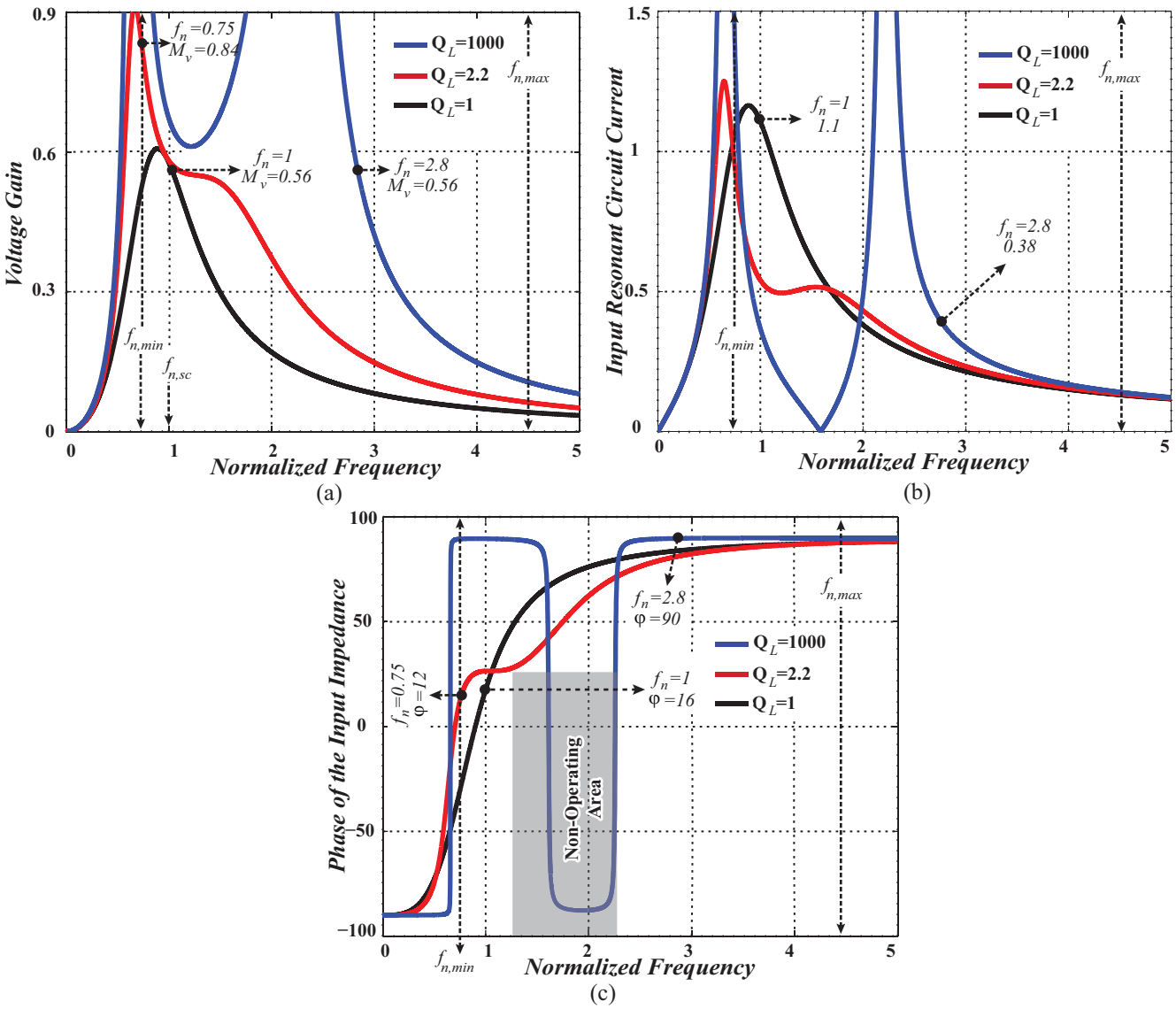

Figure 3.11: FHA analysis of the $L3C2$ resonant converter with capacitive output filter for $L_s = 4.7$, $L_n = 0.9$ & $C_n = 0.3$, and constant values of normalized load resistances (Q_L): (a) Magnitude of voltage transfer function (M_v), (b) Amplitude of the normalized first series inductance current ($I_{L_{S_1}}$), and (c) Phase of the input impedance (φ).

input-output specifications and switching frequency variations.

3.6.1 $L3C2$ Design

Fig. 3.11 presents the voltage transfer function M_v, first series inductance current $I_{L_{s_1}}$, and the input impedance phase φ versus frequency for $L_n = 0.9$, $L_s = 4.7$, and $C_n = 0.3$. As observed in Fig. 3.11(a), the minimum switching frequency is determined by the maximum output voltage in nominal output power ($Q_L = 2.2$) located between $f_{r,oc1}$ and $f_{r,sc}$. In order to obtain high efficiency in nominal load conditions, the circulating current must be minimal. According to Fig. 3.11(b), the amplitude of the switches' current decreases drastically in higher Q_L when the switching frequency is around short circuit resonant frequency $f_{r,sc}$. Moreover, the voltage gain is independent from the load (no-load conditions are exceptional) means minimum switching variation in nominal output voltage. This point is selected for nominal load operation ($Q_L = 1$). The minimum required output voltage in no-load conditions defines the maximum switching frequency ($Q_L = 1000$). According to Fig 3.11(a), it is possible to increase the switching frequency in order to decrease the output voltage to zero. Fig. 3.11(c) presents the phase of the resonant circuit input impedance, φ versus frequency for different load conditions. In order to obtain high efficiency and provide a noise-free output voltage, soft switching is necessary for the power MOSFETs. Therefore, it is vital that the resonant circuit behave like an inductive load. According to Fig. 3.11(c), between the minimum and maximum switching frequency there is a non-operating area for high Q_L. Except for in the mentioned non-operating area, the resonant circuit works in inductive regions and ZVS is provided for the half-bridge inverter. In the following, the $L3C2$ resonant circuit elements are calculated based on the voltage transfer function curves and the power charger specifications including the input voltage, output voltage, output power and switching frequency variations. The main specifications of the battery charger are assumed as follows:

$$\begin{aligned} V_{in} &= 400VDC,\ V'_{bat} = 96VDC \\ P_{out} &= 950W,\ f_s = 100 - 600kHz \end{aligned} \tag{3.28}$$

According to Fig. 3.11(a), the minimum normalized switching frequency is equal to 0.75. As a result the resonant frequency is given by the following equation:

$$f_{n,min} = 0.75,\ f_{s,min} = 100kHz,\ f_n = \frac{f_s}{f_0} \implies f_0 = 133kHz \tag{3.29}$$

The voltage gain at $f_n = 1$ and the nominal load conditions are given as follows:

$$M_v = 0.56\ for\ Q_L = 1,\ L_n = 0.9,\ L_s = 4.7,\ C_n = 0.3 \tag{3.30}$$

Therefore, the parallel capacitor voltage (output voltage) and transformer turns-ratio are calculated as follows:

$$\begin{aligned} V_{bat,n} &= M_v.V_{in} = 0.56 \times 400 = 224VDC \\ n &= \frac{N_p}{N_s} = \frac{V_{bat,n}}{V'_{bat,n}} \implies n = \frac{224}{96} = 2.33 \end{aligned} \tag{3.31}$$

According to Eqs. 3.7, the characteristic impedance is given by:

$$R_L = \frac{{V_{bat}}^2}{P_{out}},\ Z_0 = \frac{R_L}{Q_L} \implies Z_0 = \frac{{V_{bat}}^2}{P_{out}Q_L} = 53\Omega \tag{3.32}$$

Therefore, the resonant components are obtained as follows:

Table 3.2: LLC and $L3C2$ Resonant Converters Parameters

Parameters	LLC	$L3C2$
V_{in}	$400VDC$	$400VDC$
$V'_{bat,n}$	$96VDC$	$96VDC$
$V'_{bat,max}$	$144VDC$	$144VDC$
P_{out}	$950W$	$950W$
f_s	$100-600kHz$	$100-600kHz$
f_0	$145kHz$	$133kHz$
C_s	$30nF$	$23nF$
C'_p	NA	$40nF$
L_{s_1}	$41\mu H$	$63\mu H$
L_{s_2}	$9\mu H$	$13\mu H$
L_p	$103\mu H$	$70\mu H$
$n=\frac{N_p}{N_s}$	2.17	2.33

$$\begin{aligned} \omega_0 &= \frac{\omega_s}{\omega_n} = 266\pi e^3 \implies L_{s_1} = \frac{Z_0}{\omega_0} = 63\mu H \\ C_s &= \frac{1}{Z_0.\omega_0} = 23nF,\ L_{s_2} = \frac{L_{s_1}}{L_s} = 13\mu H \\ L_p &= \frac{L_{s_1}}{L_n} = 70\mu H,\ C_p = C_n.C_s = 6.9nF \end{aligned} \tag{3.33}$$

The $L3C2$ resonant circuit parameters used in the simulation results and experimental prototype are summarized in Table 3.2.

3.6.2 LLC Design

Fig. 3.12 shows the voltage transfer function M_v, first series inductance current $I_{L_{s_1}}$, and the input impedance phase φ versus frequency for $L_n = 0.4$, and $L_s = 4.4$. As indicated in Fig 3.12(a), the minimum normalized switching frequency is equal to 0.69. Therefore the resonant frequency is calculated using the following equation:

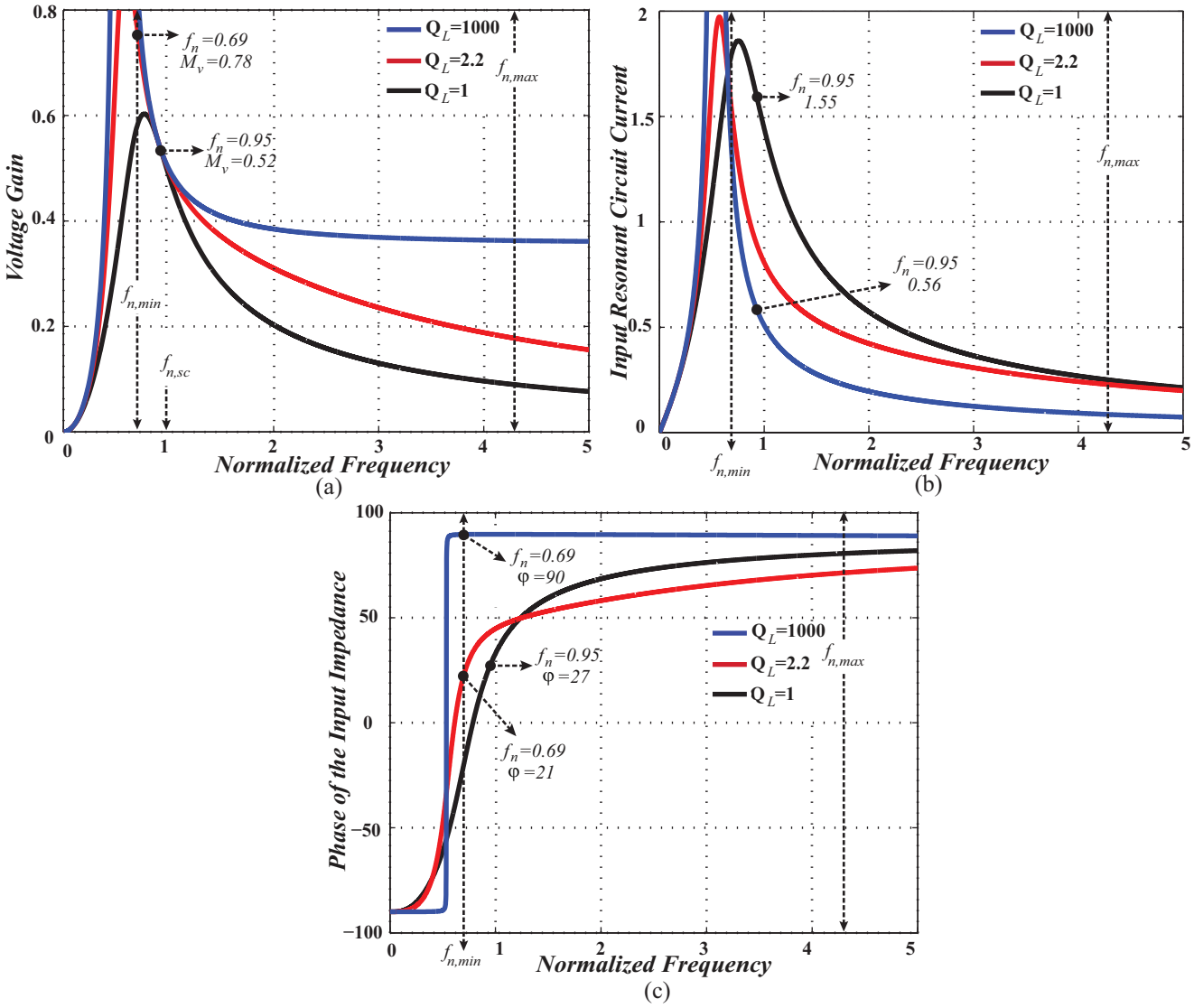

Figure 3.12: FHA analysis of the LLC resonant converter for $L_s = 4.4$, and $L_n = 0.4$, with constant values for normalized load resistances (Q_L): (a) Magnitude of voltage transfer function (M_v), (b) Amplitude of the normalized first series inductance current ($I_{L_{S_1}}$), and (c) Phase of the input impedance (φ).

$$f_{n,min} = 0.69,\ f_{s,min} = 100kHz,\ f_n = \frac{f_s}{f_0} \implies f_0 = 145kHz \tag{3.34}$$

In nominal load conditions ($Q_L = 1$) the voltage gain is equal to 0.52 and, as a result, transformer turns-ratio is obtained as follows:

$$n = \frac{N_p}{N_s} = \frac{V_{bat,n}}{V'_{bat,n}} = \frac{M_v.V_{in}}{V'_{bat}} = 2.17 \tag{3.35}$$

In the LLC resonant converter with capacitive output filter the equivalent resistance is obtained using Eq. 2.8 and is equal to:

$$R'_L = \frac{{V'_{bat}}^2}{Pout} = 9.7\Omega \implies R'_{eq} = 7.9\Omega,\ R_{eq} = n^2 R'_{eq} = 37.2\Omega \tag{3.36}$$

The resonant circuit elements of the LLC resonant circuit are calculated as follows:

$$\begin{aligned} &Z_0 = \frac{R_{eq}}{Q_L} = 37.2\Omega,\ \omega_0 = \frac{\omega_s}{\omega_n} = 290\pi e^3 \\ &\implies L_{s_1} = \frac{Z_0}{\omega_0} = 41\mu H,\ C_s = \frac{1}{Z_0.\omega_0} = 30nF,\ L_{s_2} = 9\mu H,\ L_p = 103\mu H \end{aligned} \tag{3.37}$$

The circuit parameters for the LLC resonant converter are provided in Table 3.2. According to Fig. 3.12(c), the input resonant phase of the LLC is positive for the mentioned range of the switching frequency and the resonant circuit represents an inductive load. As a result, ZVS is guaranteed for all loads and output voltage conditions. Comparing the converters elements collected in Table 3.2 reveals that the only extra element in the proposed $L3C2$ resonant converter is the parallel resonant capacitor put in the transformer secondary side.

3.7 Simulation and Experimental Results

In order to investigate and compare the performance of the designed resonant converters ($L3C2$ versus LLC), software simulation and prototype platforms have been employed to extract the voltage gains under different load conditions. The components, which are used in the prototypes are shown in Tables 3.3. The selected switching frequency is between $100kHz$ and $600kHz$, and the frequency span for the voltage gain curves is $10kHz$, which

Table 3.3: Components of Resonant Converters Platforms

Component	*Part Number*	*Ratings*
Inverter MOSFET's	$IXFX64N60$	$600VDC, 64A$
Series Resonant Cap.	*Film Cap.*	$10nF, 2000VDC$
Series Resonant Ind.	$RM12$	$3F3$
Transformer	$RM14$	$3F3$
Parallel Resonant Cap.	*Film Cap.*	$10nF, 1000VDC$
Rectifier Diode	$MBR40250$	$250V, 40A$
Output Cap.	*Film Cap.*	$1.5uF, 250VDC$

means more than fifty points have been extracted in each drawing. The simulation and experimental results are presented in Fig. 3.13. There are several limitations indicated in each figure, including minimum and maximum switching frequencies, the maximum output power, and the maximum output voltage. The simulation and experimental results are presented in solid and dotted shapes, respectively. Fig. 3.13 presents the results for the LLC and $L3C2$ resonant converters under three different load conditions. According to Fig. 3.13(a), in the LLC resonant converter the simulation and experimental results are almost the same for $R'_L = 9.75\Omega$ and $R'_L = 21.9\Omega$. But for no-load condition in the LLC resonant converter, there is a discrepancy between simulation and experimental results. In fact, for switching frequency higher than $300kHz$, the effect of the output diodes junction capacitances leads to increased output voltage in the LLC. As observed in Fig. 3.13(b), in the $L3C2$ resonant converter the simulation and experimental voltage gains have a good fit for different load conditions. The analytical equations obtained based on FHA can precisely predict the behavior of the multi-resonant $L3C2$ resonant converter with capacitive output filter for a wide range of output voltages and loads (as already depicted in Fig. 3.11(a)).

In order to the provide high quality output voltage and maximize the converter efficiency, it is vital to realize soft commutation for the output rectifier diodes. Basically, the reverse

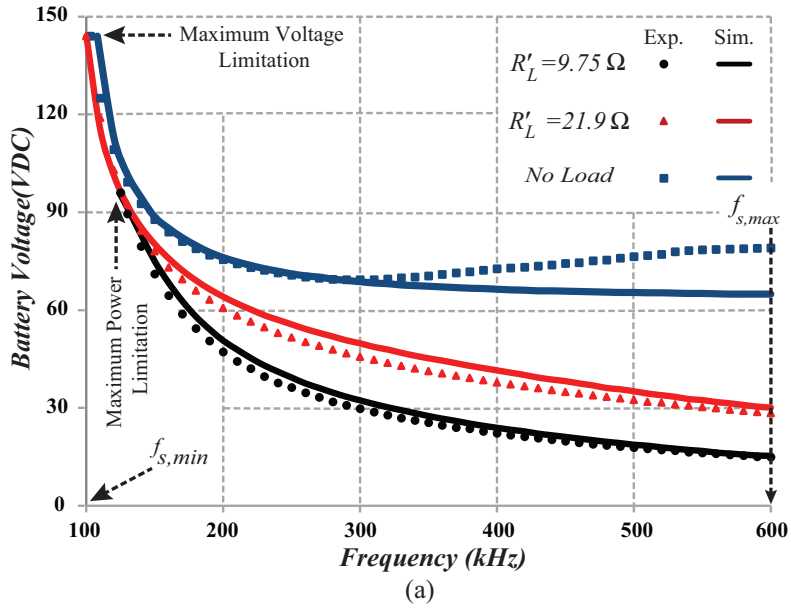

(a)

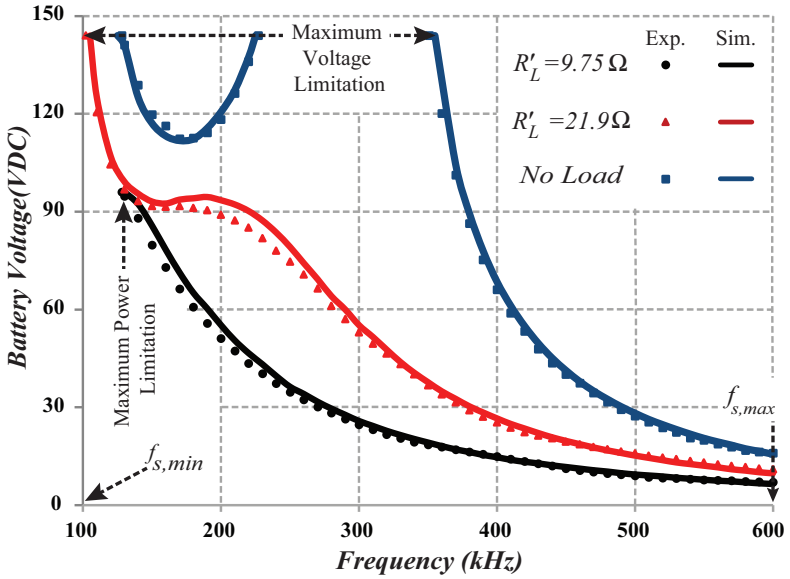

(b)

Figure 3.13: Simulation and experimental results for battery voltage versus frequency. (a) The LLC resonant converter, and (b) The $L3C2$ resonant converter.

recovery current of output rectifier diodes during the turn-off transition leads to a high voltage peak across output diodes and, as a result, diodes with more withstand voltage should be selected, which means more conduction losses. The LLC and $L3C2$ converters can provide ZCS for output diodes for wide variation of switching frequency. Fig. 3.14(a)-(b) shows the

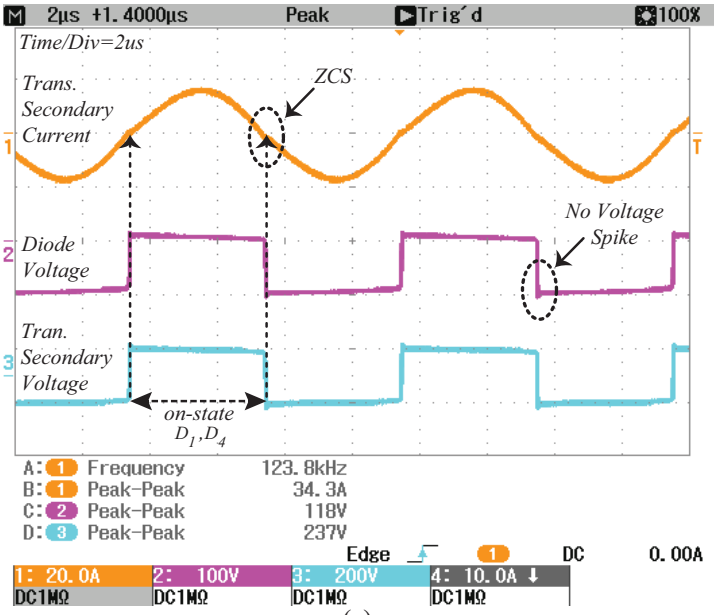

(a)

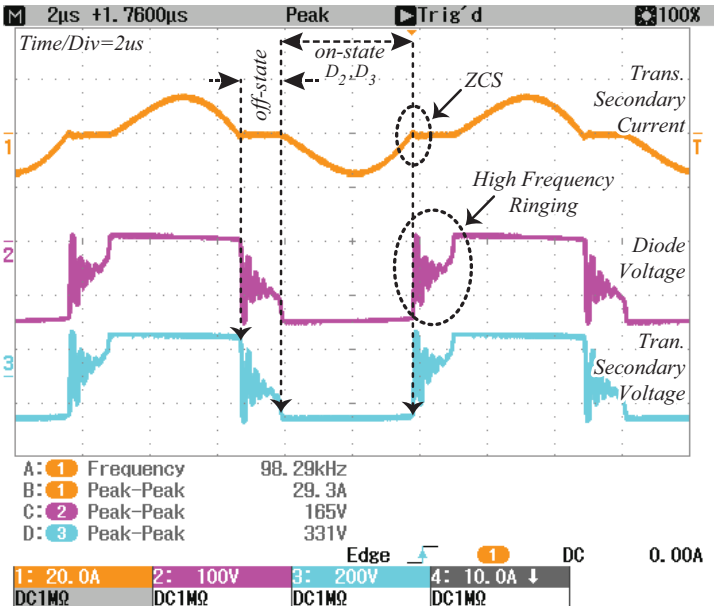

(b)

Figure 3.14: LLC transformer secondary side waveforms: (a) $V'_{bat} = 96VDC$ and $P_{out} = 950W$, and (b) $V'_{bat} = 144VDC$ and $P_{out} = 950W$ (High voltage, high frequency ringing for this condition).

experimental waveforms of the voltage and current on the secondary side of the transformer in the LLC resonant converters for two full power conditions. According to these figures, ZCS is provided for output rectifier diodes and voltage peak is eliminated. However in the LLC

resonant converter for switching frequency below and far from $f_{r,sc}$ (around the minimum switching frequency) and during the off-state intervals of the output rectifier diodes, high voltage, high frequency ringings exist across the rectifier diodes, which decrease the quality of the output voltage and increase the EMI. The proposed $L3C2$ design overcomes this issue and results in reduced ringing. According to the operating modes of the $L3C2$ output rectifier, as indicated in Fig. 3.4, in the end of power transfer interval, once $i_{L_{s_2}}$ reaches zero, the output diodes current smoothly reaches zero. This causes ZCS at turn-off and avoids any reverse recovery losses in the output diodes. In addition, the voltage across the diodes is smooth and sinusoidal during the switching transitions which leads to a minimum negative impact on the diode junction capacitance in transient time. Fig. 3.15(a)-(b) presents the transformer secondary side waveforms extracted from the $L3C2$ resonant converter platform. The experimental results for two full load conditions show the soft switching transient in turn-on and turn-off conditions without any high frequency ringing.

Figs. 3.16 and 3.17 present the voltage and current waveforms extracted from experimental platforms of the LLC and $L3C2$ resonant converters, respectively. In each figure, Drain-Source voltage of the low-side MOSFET and the first series inductor current (MOSFETs current) are illustrated for different conditions. According to these figures, the zero crossings of the resonant circuit input current is within the low-side MOSFET voltage pulse and, as a result, in all of the presented conditions the half-bridge switches are fully turned on under zero voltage. Therefore, both the LLC and the $L3C2$ achieve soft switching transitions.

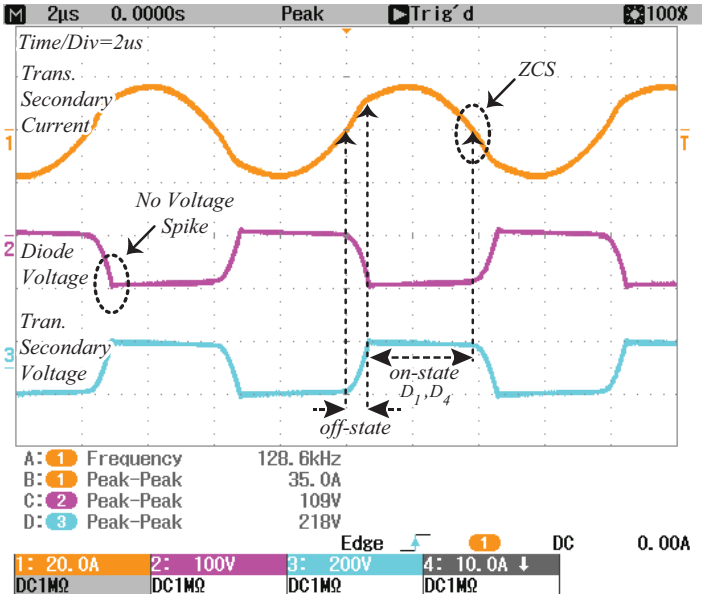

(a)

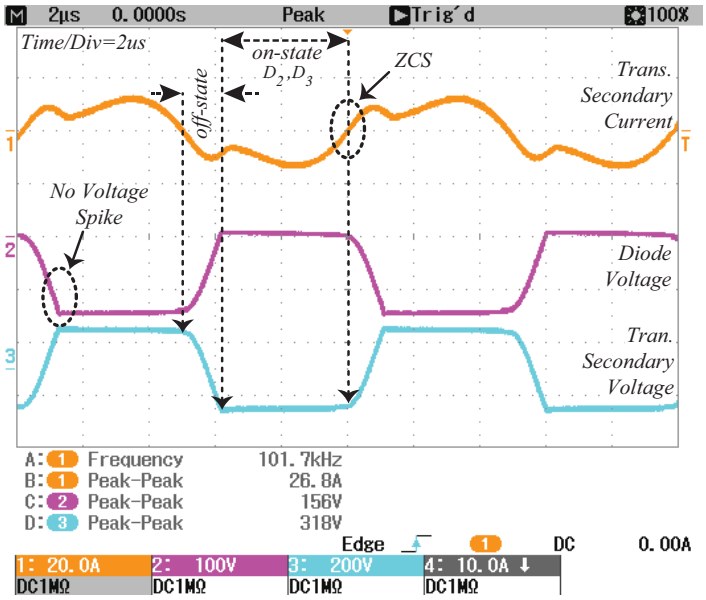

(b)

Figure 3.15: $L3C2$ transformer secondary side waveforms: (a) $V'_{bat} = 96VDC$ and $P_{out} = 950W$, and (b) $V'_{bat} = 144VDC$ and $P_{out} = 950W$ (Elimination of the high frequency ringing).

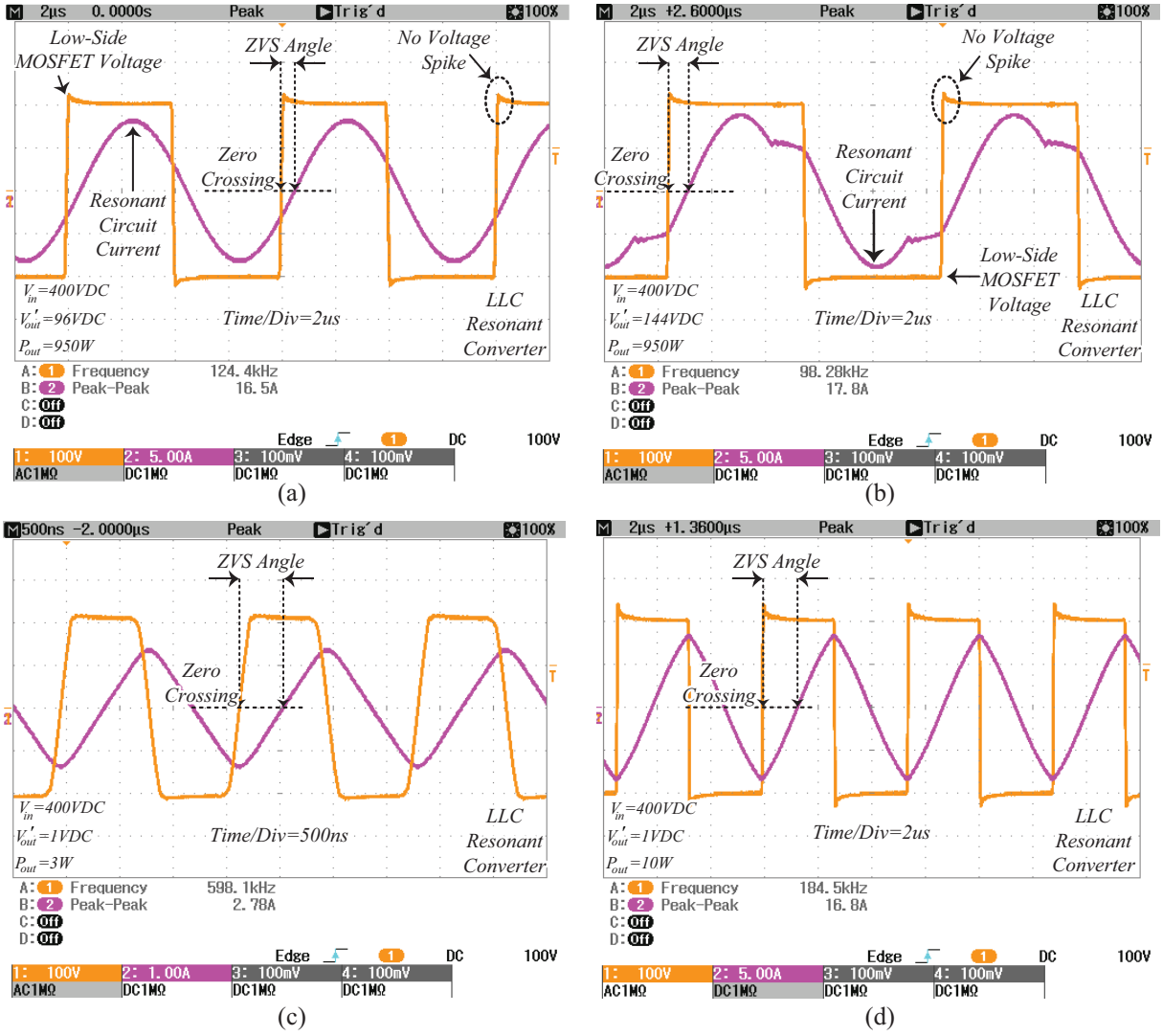

Figure 3.16: Experimental results for the LLC resonant converter, Drain-Source voltage for low-side MOSFET in half-bridge inverter (S_2) and first series resonant inductor current ($I_{L_{s_1}}$): (a) $V'_{bat} = 96VDC$ and $P_{out} = 950W$, (b) $V'_{bat} = 144VDC$ and $P_{out} = 950W$, (c) $V'_{bat} = 1VDC$ and $P_{out} = 3W$, and (d) $V'_{bat} = 1VDC$ and $P_{out} = 10W$.

3.8 Comparison of the LLC and $L3C2$ as a Battery Charger

In this section, two main aspects of the studied resonant converters are considered, including the efficiency curves and obtainable V-I planes. One of the main advantages of resonant

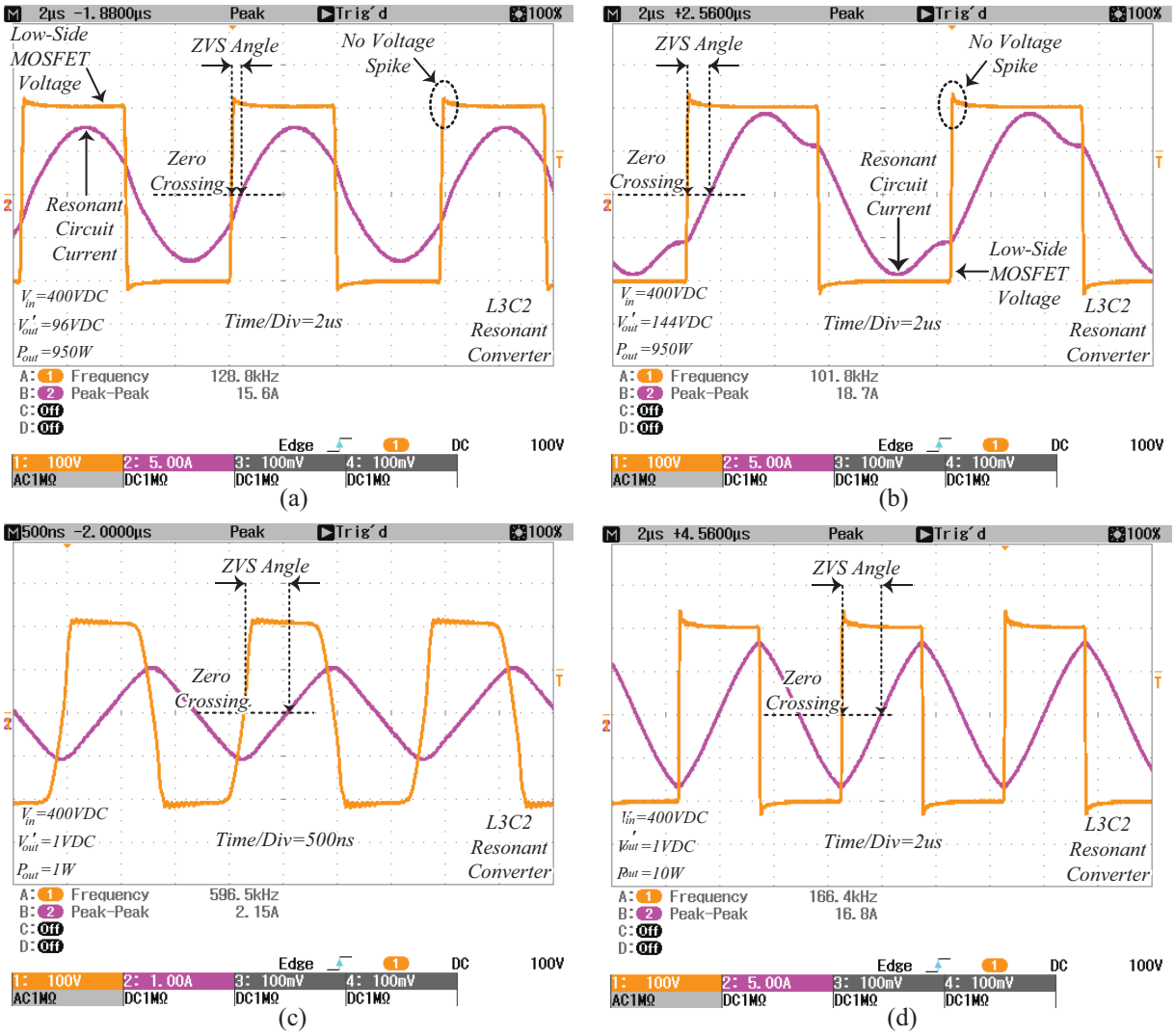

Figure 3.17: Experimental results for the $L3C2$ resonant converter, Drain-Source voltage for low-side MOSFET in half-bridge inverter (S_2) and first series resonant inductor current ($I_{L_{s_1}}$): (a) $V'_{bat} = 96VDC$ and $P_{out} = 950W$, (b) $V'_{bat} = 144VDC$ and $P_{out} = 950W$, (c) $V'_{bat} = 1VDC$ and $P_{out} = 1W$, and (d) $V'_{bat} = 1VDC$ and $P_{out} = 10W$.

converters is soft switching, which leads to high switching frequency and high power density. In addition, ZVS is necessary to provide a low noise environment which improves the quality of the output voltage. Fig. 3.18 presents the efficiency curves of the LLC and $L3C2$ resonant converters for two different output voltages. According to these curves, the designed resonant converters present an efficiency higher than 95% for an output power greater than $500W$,

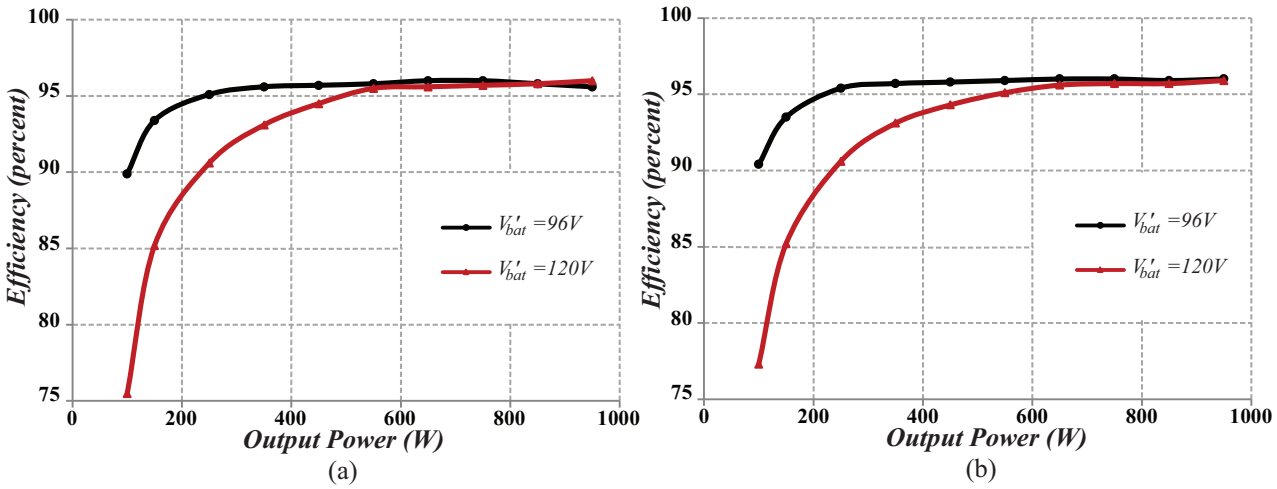

Figure 3.18: Efficiency curves at fixed output voltages: (a) LLC resonant converter, and (b) $L3C2$ resonant converter.

and the maximum efficiency for both cases is 96%.

In the following, the V-I planes of the LLC and $L3C2$ are obtained in order to investigate the maximum coverage region. As mentioned in the introduction, the battery charger must be able to respond to different modes of the charge algorithms and cover almost all of the V-I plane region. The V-I planes obtained from the experimental platforms of the resonant converters are shown in Fig. 3.19. In order to draw the planes, the platforms have been tested under different output voltage and output current conditions. In each plane there are different limitations on the boundaries, including current, voltage, and power, and each point in the boundary indicates one experimental test. The V-I plane obtained from the LLC resonant converter platform is shown in Fig. 3.19(a). Due to the effect of output diodes junction capacitances in no-load conditions, the output voltage increases for switching frequencies higher than $300kHz$ (as indicated in Fig. 3.13(a)). Note that the unobtainable area of the LLC resonant converter starts in the no-load boundary at $V'_{bat} = 72VDC$. In order to decrease the battery voltage to less than $72VDC$, the battery current is forced to increase from zero. Finally, in the minimum desired voltage $V'_{bat} = 1VDC$, the current

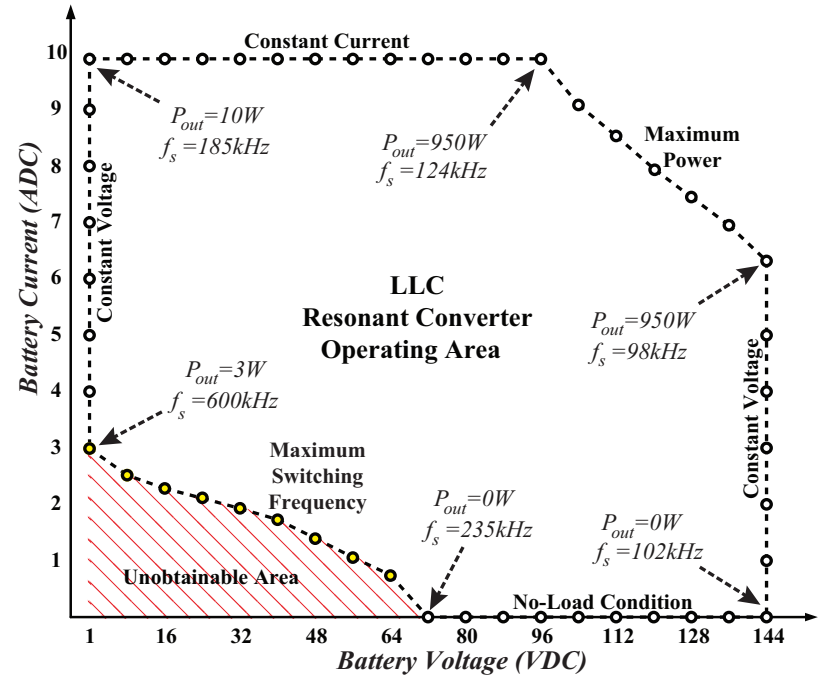

(a)

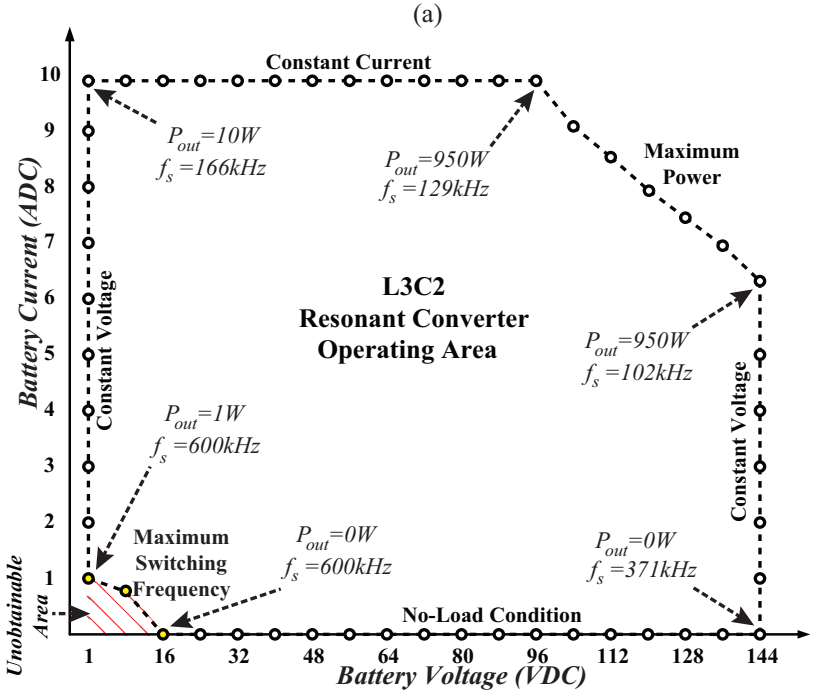

(b)

Figure 3.19: Obtained V-I plane from two considered resonant converters: (a) *LLC* resonant converter, and (b) *L3C2* resonant converter.

is equal to 3Amps. The red dashed region indicates the unobtainable area of the LLC resonant converter. Fig. 3.19(b) proves that the multi-resonant $L3C2$ resonant converter can cover almost all of the region in the V-I plane. According to Fig. 3.19(b), the minimum output voltage in no-load conditions occurs at $V'_{bat} = 16VDC$, and the area obtained by the proposed resonant converter is significantly extended in comparison with the LLC V-I plane. Fig. 3.19(b) demonstrates that the proposed $L3C2$ resonant converter is capable of covering the battery V-I plane, regulating the voltage from near zero to 1.5 times nominal voltage under different load, and can be employed as a battery charger without using burst mode operation.

3.9 Summary

This chapter introduced the multi-resonant half bridge $L3C2$ resonant topology as a power converter for medium power level applications that can regulate the battery voltage in a wide range, from near zero voltage, zero current to the maximum output power, without using burst mode operation. Due to the wide voltage regulation, the proposed resonant converter can respond to charge algorithms of different kind of batteries, such as Lead-acid and Li-Ion and is a good candidate for use as a charger in electric vehicles. The main advantage of the proposed resonant converter in comparison with LLC resonant converter is its ability to revitalize dead batteries in continuous conduction mode. The low-ripple output voltage enhances the quality of the charging current in the recovery region, thereby increasing the life cycle of the battery. Also, soft switching of the MOSFETs and output rectifier diodes provide high efficiency, and the capability of working in high switching frequency without any limitation. Since the $L3C2$ resonant converter can be implemented using a half bridge inverter, the total cost will be lower in comparison with the solution presented in Chapter 2; however, the new $L3C2$ topology has one extra resonant element in comparison with LLC,

as presented in Table 3.2, and the optimum design of the $L3C2$ will be more complicated and need more effort in comparison with the LLC resonant converter. There is also a trade-off between using LLC and $L3C2$ resonant converters when efficiency curves are taken into account. Even though the $L3C2$ resonant converter can operate in the the continuous conduction mode and provide a ripple free charging current for the battery pack, Fig. 3.18 shows that the LLC resonant converter has a better flat efficiency curve at the maximum battery voltage $V'_{bat} = 120VDC$. According to Fig. 3.18, the LLC resonant converter has 0.5% better efficiency at around $600W$ in comparison with the $L3C2$.

Chapter 4

Fourth Order $L3C$ Resonant Converter for PV Battery Charger applications[4]

In Chapters 2 and 3, two different topologies (modified LLC and $L3C2$) and one modulation strategy (frequency and phase shift modulation) were presented as solutions for battery charger applications for medium to high power levels. In this chapter, a new resonant power converter will be introduced with the application of Electric Vehicles with rooftop photovoltaic (PV) panels. In Chapters 2 and 3, it was assumed that the input voltage of a DC-DC power stage is almost constant and is provided by a PFC input stage. Since solar irradiance and surface temperature can affect the performance of the solar panel and change the PV panel voltage, the input voltage of a DC-DC power converter is not constant and changes in a wide range ($V_{pv} = 24 - 45VDC$). Also, in an EV, the PV panel energy needs to be stored in a recharegable battery. The combination of PV panel and rechargeable battery requires extreme regulation from the input ($V_{pv} = 24 - 45VDC$) to output ($V'_{bat} = 230 - 430VDC$), which needs to be supported by a DC-DC power converter. In this case, the DC-DC power converter should not only track the input voltage variation for extracting the maximum available power from the PV panel, but also boost the input voltage by variable gain and respond to the different state of charge of the battery pack. As an example of extreme input and output regulations, Fig. 4.1(a) shows a single PV panel on the rooftop of an EV. The power capacity range is from $50W$ to $350W$ and the input voltage ranges widely from

[4]Portions of this chapter have been accepted for publication in [5]

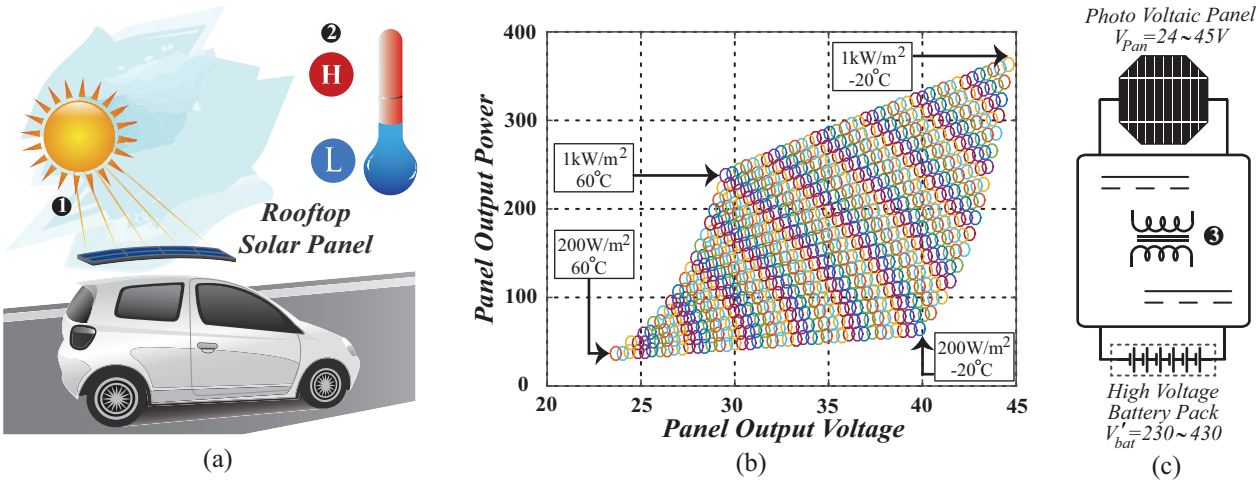

Figure 4.1: (a) Pure electric vehicle with roof top solar panel[8] (① and ② depict sun radiation and temperature can vary depending on geography location and time of the day), (b) panel power-voltage plane covered by DC-DC power converter, for each point in the mentioned area, DC-DC power converter should regulate the battery voltage from $V'_{bat} = 230VDC$ to $V'_{bat} = 430VDC$, and (c) DC-DC power converter block diagram which should regulate the battery charging voltage from $230VDC$ to $430VDC$ in a wide variation of input voltage (③ illustrates the necessity of galvanic isolation for the power converter).

$V_{pv} = 24 - 45VDC$. This undesirable wide input variation is due to the effect of solar irradiance and ambient temperature that affects the power-voltage characteristics of the PV panel illustrated in Fig. 4.1(b). As well, the battery pack depicted in Fig. 4.1(c) shows that the output voltage should comply with extreme regulation as well to cover $230 - 430VDC$.

This chapter proposes a high-efficiency isolated fourth-order $L3C$ resonant converter with the variable frequency control, which has the capability of extreme regulation for applications which interface PV panels to high-voltage battery packs with the aim of tracking the maximum input power while regulating the output voltage in a wide range. In comparison with other well-known series-parallel resonant power converter topologies (e.g. $LLC; LCLC; L3C2$), the proposed topology presents a steep voltage gain versus frequency, which makes it an excellent candidate for PV to high-voltage battery pack applications. Also, this topology does not employ a series resonant capacitor in the primary side of the

converter, which removes a high-voltage, high-current ripple capacitor from the primary side and facilitates the charger design in terms of component selections. The parallel resonant capacitor, put in the secondary of the transformer, leads to Zero Current Switching (ZCS) of the output rectifier diodes, eliminates the voltage peak produced by the diodes reverse recovery current and decreases the noise in the output voltage. Moreover, due to operating in the inductive load region, power MOSFETs in the high frequency $L3C$ resonant converter always work in ZVS for different load condition, providing high-efficiency, low-noise output voltage. Other particular advantages of the proposed converter are inherent short circuit protection and voltage gain of more than unity for resonant tank. In this chapter, first the general equations for solar PV panels will be extracted based on the general model of a solar cell and employed to determine the variation of power-voltage characteristics of a specific PV module versus irradiance and temperature variations [124–126]. Then, the complete analysis of the $L3C$ resonant converter with consideration of transformer primary and secondary leakage inductances, transformer secondary winding capacitance, and output rectifier junction capacitances is obtained. Using the analytical equations extracted for fourth-order $L3C$ resonant circuits, a $350W$ DC-DC power converter is designed and implemented. Finally, experimental results are presented to demonstrate the circuit performance and to prove the feasibility of extreme regulation for both input and output sides. The results show the $L3C$ resonant converter can track all input voltage variations related to maximum input power ($(V_{pv} = 24 - 45VDC)$ presented in Fig. 4.1(b)), while regulating the battery voltage from $230VDC$ to $430VDC$.

4.1 Photovoltaic Module Characteristics

As presented in Fig. 4.1(b), the PV panel maximum output power changes with respect to irradiance and temperature and the proposed $L3C$ resonant converter should track these

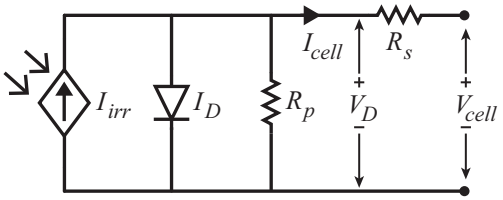

Figure 4.2: General model of a solar cell including parallel and series resistors.

variations in order to transfer the maximum input power to the high-voltage battery pack. In this section the general equations for PV panels will be extracted and employed to determine the variation of power-voltage characteristics of a specific PV module versus irradiance and temperature variations. A PV module consists of a number of interconnected solar cells forming a single unit. To model the power-voltage characteristics of a PV module, the power-voltage characteristics of a single solar cell should be determined and then expanded to obtain the behavior of a PV array or module. A solar cell is traditionally represented by an equivalent circuit composed of a current source, an anti-parallel diode, a series resistance (R_s) and a shunt resistance (R_p), as shown in Fig. 4.2 [124, 125]. In Fig. 4.2, I_{irr} is the irradiance current, which is generated when the cell is exposed to sunlight and is dependent on the solar irradiance and temperature [124, 125].

$$I_{irr} = I_{irr,ref}(\frac{G}{G_{ref}})[1 + \alpha_T(T - T_{ref})] \tag{4.1}$$

The subscript ref represents the standard reference conditions and α_T represents the rate of change of the short-circuit current with respect to temperature and is provided by the manufacturers. The cell temperature, T is a function of changes in the ambient temperature and changes in the insulation [125].

$$T = T_{amb} + (\frac{NOCT - 20°C}{0.8})G \tag{4.2}$$

$NOCT$ represents the Nominal Operating Cell Temperature provided by the manufacturer. In Fig. 4.2, I_D is the current of the anti-parallel diode which characterizes the non linearity of the solar cell and is a function of the diode voltage and temperature, as presented in (4.3) [124].

$$I_D = I_o(e^{\frac{qV_D}{nkT}} - 1) \tag{4.3}$$

In Eq. (4.3), n is the ideality factor or the ideal constant of the diode and T is the temperature of the cell. The ideality factor (n) represents the different mechanisms of moving carriers across the junction. As an example, for silicon, n will be 1.3 [126]. I_o is the diode saturation current or cell reverse saturation current [124]. According to Fig. 4.2, the relation between the voltage and current of the PV cell can be obtained as follows.

$$I_{cell} = I_{irr} - I_o(e^{\frac{q(V_{cell}+I_{cell}R_s)}{nkT}} - 1) - \frac{(V_{cell} + I_{cell}R_s)}{R_p} \tag{4.4}$$

And for a PV panel with N_s number of series cells and N_p number of parallel cells, Eq. (4.4) can be rewritten as as follows:

$$I_{pv} = N_pI_{irr} - N_pI_o(e^{\frac{q(V_{pv}+I_{pv}R_sN_s/N_p)}{nkT}} - 1) - \frac{V_{pv} + I_{pv}R_sN_s/N_p}{R_pN_s/N_p} \tag{4.5}$$

The V-I relationship of a PV panel presented in Eq. (4.5) can be used to obtain the Power-Voltage relationship of a PV panel in different ambient temperature and solar irradiance and determine the maximum power point of the PV panel. In cases that the resistive parameters, R_s and R_p, are not provided by the manufacturer of the PV panels, the equations can be simplified by setting them as zero and infinity, respectively. In this study, the Power-Voltage characteristics of a PV module from Canadian Solar is presented in Fig. 4.1(b) [127]. For this specific example, the PV array consists of 72 PV cells connected in series and parallel.

The PV panel coefficients are extracted from datasheet, and by employing Eq. (4.5), the variation of Power-Voltage of photovoltaic module as a function of irradiance and temperature is presented in Fig. 4.3. The voltage related to maximum power point for each condition is defined in Fig. 4.3, which indicates wide input voltage variation ($V_{pv} = 24 - 45VDC$). According to Fig. 4.3, the power-voltage characteristics of a photovoltaic module is as a function of the irradiance and surface temperature. It means in order to get the maximum power from the solar panel, the input voltage has to be adjusted,which reflects the need for the proposed $L3C$ converter to regulate a wide input voltage range.

4.2 Steady State Analysis of $L3C$ Resonant Converter

In this section, the complete analysis of an $L3C$ resonant converter will be presented. Fig. 4.4 shows a complete schematic of the proposed $L3C$ resonant converter, including a transformer secondary side and diode junction parasitic capacitances. In Fig. 4.4, a fourth order model of the transformer (including primary and secondary leakage inductances, magnetizing inductance, and winding capacitance of the transformer secondary side) has been employed as a model for the non-ideal transformer [123]. Also, the junction capacitances of the output rectifier are considered in parallel with diodes. In the proposed resonant converter, the parallel resonant capacitor in the secondary side of the transformer can merge all parasitics capacitors of the secondary side into the resonant circuit. As shown in Fig. 4.4, the primary leakage inductance is merged with the external inductor and is part of L_{s_1}. In addition, the secondary leakage and magnetizing inductances of the transformer are considered L_{s_2} and L_p, respectively. As mentioned previously, due to the high amplitude, high frequency current in the primary side of the converter, well-known series-parallel resonant power converters (e.g. $LLC, LCC, LCLC,\ L3C2$) have difficulties in terms of series resonant capacitor selection,

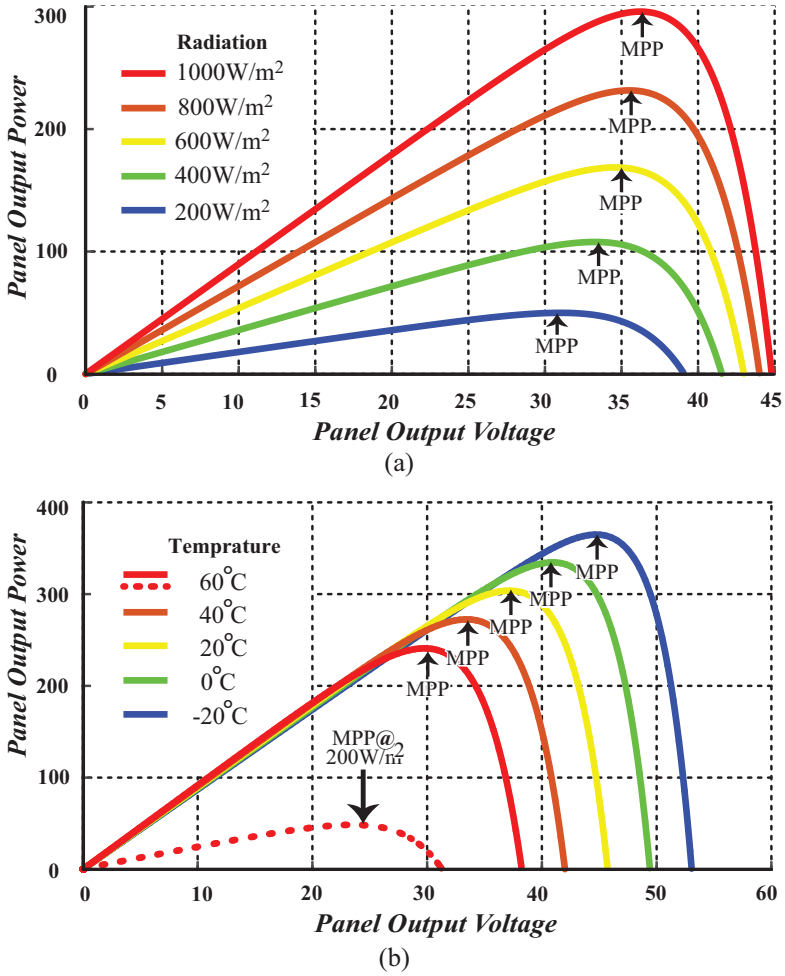

Figure 4.3: Variation of Power-Voltage characteristics of a photovoltaic module as a function of (a) Irradiance at $20°C$, and (b) Temperature at $1000W/m^2$. The dashed curve in Fig. 4.3(b) presents the minimum output power of the PV panel, occurs at maximum ambient temperature ($60°C$) and minimum sun irradiance ($200W/m^2$)

and this resonant capacitor has to withstand high current and voltage stresses. According to Fig. 4.4, the proposed topology does not employ any series resonant capacitor in the primary side of the converter, which facilitates the charger design in terms of component selections. In Fig. 4.4, all of the elements in the secondary side are defined with an apostrophe, but in all equations, the variables and elements are transferred to the primary side with respect to the transformer turns-ratio, and are shown without an apostrophe. Since the behaviour of the output rectifier in the $L3C$ is similar to that of the $L3C2$ (Section 3.2), the same equivalent

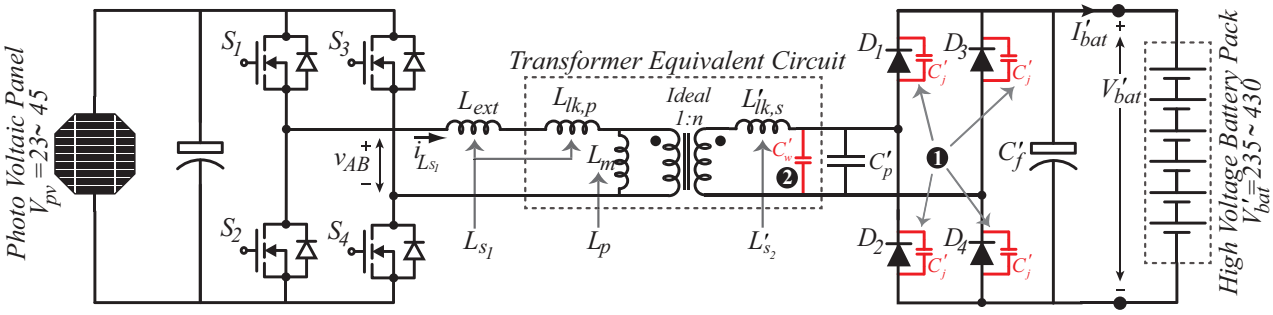

Figure 4.4: Full bridge *L3C* resonant converter schematic with capacitive output filter, applicable for PV to high voltage battery applications.

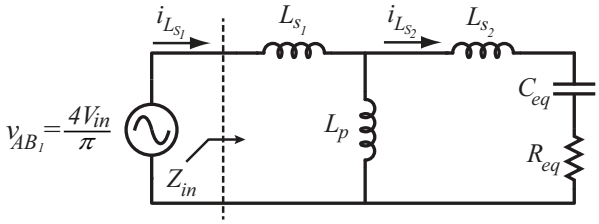

Figure 4.5: AC equivalent circuit of the *L3C* resonant converter.

circuit can be employed in order to model the output rectifier along with output filter and load. The elements of the equivalent circuit are presented in Eq. (3.2) and Eq. (3.3).

Fig. 4.5 shows the AC equivalent circuit of the resonant circuit along with the equivalent impedance of the transformer secondary side, R_{eq} and C_{eq} (including the output rectifier, output filter, and load). By using this equivalent circuit, it is possible to employ the FHA technique for analysis of the *L3C* resonant circuit. In order to calculate the output current, the second series resonant inductor current is assumed to be purely sinusoidal. Due to the non-conduction angle of the output rectifier, the output current can be obtained as follows [3]:

$$I_o = \frac{(1+\cos\psi)}{\pi} I_{L_{s_2}} \tag{4.6}$$

Therefore, the output voltage of the full-bridge *L3C* resonant converter with capacitive

output filter is given by:

$$V_{bat} = R_{bat}.I_{bat} = R_L \frac{(1+\cos\psi)}{\pi} I_{L_{s_2}} \tag{4.7}$$

According to Fig. 4.5, applying KVL and KCL gives the relation between the battery voltage and the amplitude of the resonant circuit input current, $I_{L_{s1}}$.

$$I_{L_{s_2}} = \left| \frac{j\omega_s L_p}{j\omega_s L_p + j\omega_s L_{s_2} + R_{eq} + \frac{1}{j\omega_s C_{eq}}} \right| I_{L_{s_1}} \tag{4.8}$$

In order to calculate the resonant circuit input current, the input impedance of the AC equivalent circuit should be obtained, which can be expressed by:

$$\mathbf{Z_{in}}(j\omega_s) = j\omega_s L_{s_1} + (j\omega_s L_p)||(j\omega_s L_{s_2} + R_{eq} + \frac{1}{j\omega_s C_{eq}}) = |\mathbf{Z_{in}}|\, e^{j\varphi} \tag{4.9}$$

One of the advantages of the proposed resonant converter is the capability to protect the full-bridge inverter from output over current and short circuit conditions. In over current conditions, $R_{bat} \to 0$ and by considering (4.9), Z_{in} would be as follows:

$$\mathbf{Z_{in}}(j\omega_s) = j\omega_s L_{s_1} + j\omega_s L_p||j\omega_s L_{s_2} \tag{4.10}$$

In this case, the inverter switches are loaded by an inductor that can limit the switches current and also load current. In fact, the resonant circuit provides an inherent short circuit protection at any operating frequency for the full-bridge inverter. In the AC equivalent circuit, the fundamental component of the resonant circuit input voltage ($v_{AB_1}(t)$) can be obtained as follows:

$$v_{AB_1} = \frac{4V_{in}}{\pi} \sin(\omega_s t) \tag{4.11}$$

According to Fig. 4.5 and Eqs. (4.9) and (4.11), the amplitude of $I_{L_{s1}}$ (MOSFETs

current) can be obtained as follows:

$$I_{L_{s1}} = \frac{4V_{in}}{\pi|\mathbf{Z_{in}}(j\omega_s)|} \tag{4.12}$$

The following normalized parameters are introduced for the resonant circuit.

$$\begin{aligned} &L = L_p + L_{s_2}, L_n = \frac{L_{s_1}}{L_p}, L_s = \frac{L_{s_1}}{L_{s_2}}, \\ &Z_0 = \sqrt{\frac{L}{C_t}}, Q_L = \frac{R_L}{Z_0}, \omega_0 = \frac{1}{\sqrt{LC_t}}, \omega_n = \frac{\omega_s}{\omega_0} \end{aligned} \tag{4.13}$$

Considering Eq. (4.7),(4.8), and (4.12) the normalized voltage gain of the $L3C$ resonant converter is obtained as follows:

$$M_v = \frac{V_{bat}}{V_{in}} = \frac{Q_L Z_0(1+\cos\psi)}{\pi V_{in}} \cdot \left| \frac{\frac{j\omega_n L_s}{L_n+L_s}}{\frac{\sin^2\psi}{\pi\omega_n} + j(\frac{\omega_n L_s}{L_n+L_s} + \frac{\omega_n L_n}{L_n+L_s} - \frac{\psi-\sin\psi\cos\psi}{\pi\omega_n})} \right| \frac{4}{\pi|\mathbf{Z_{in}}(j\omega_n)|} \tag{4.14}$$

where

$$\psi = \cos^{-1}(\frac{\pi - 2\omega_0 Q_L}{\pi + 2\omega_0 Q_L}) \tag{4.15}$$

In the next section, Eq. (4.14) will be employed to study the voltage gain behavior of the $L3C$ resonant converter and its capability for extreme regulation, while considering input impedance phase of the resonant circuit for soft switching condition.

4.3 Resonant Power Converter Design

In this section, the design procedure will be presented for power conditioning of a $350W$ solar PV panel to high voltage battery pack, using proposed $L3C$ resonant converter. The main objective during design procedure is to design $L3C$ in such a way as to cover all regions of the Power-Voltage plane presented in Fig. 4.1(b) and regulate the battery voltage from $V_{bat} = 230VDC$ to $V_{bat} = 430VDC$. According to the steady-state analysis of the $L3C$ resonant converter, the equations obtained for $L3C$ steady state condition is a function of three normalized variables (L_n, L_s, and Q_L), making the design a multidimensional optimization problem with multiple tradeoff challenges. The desired normalized parameters should be selected in such a way to provide essential voltage gain (around 10) for boosting the voltage from the PV panel to the high voltage battery (from $V_{pv} = 24 - 45VDC$ to $V'_{bat} = 230VDC - 430VDC$) while providing soft switching conditions for all semiconductor devices. In this chapter, the values of the normalized parameters are selected based on maximum required voltage gain in different input voltage conditions and essential output voltage regulations, and the values of the input impedance phase needed to achieve ZVS in all conditions, and similar to previous chapters, Design of Experiment Methodology (DoE) has been employed. Based on the obtained normalized equations for input impedance phase and voltage gain, presented in Eqs. 4.9 and 4.14 respectively, the behaviour of the resonant converter is studied using DoE for a wide range of normalized parameters with consideration of input-output voltage variations, which leads to $L_n = 0.25$, $L_s = 5$, and $Q_L = 2$ as the optimum normalized parameters. In this case, $Q_L = 2$ presents the load condition related to maximum output voltage and output power, $V_{bat} = 430VDC$ and $P_{out} = 350W$ at minimum operating temperature and maximum irradiance ($-20°C$ and $1000W/m^2$). Fig. 4.6 presents the voltage transfer function M_v, and the input impedance phase φ versus normalized frequency for selected values of normalized parameters. The main specifications of the battery

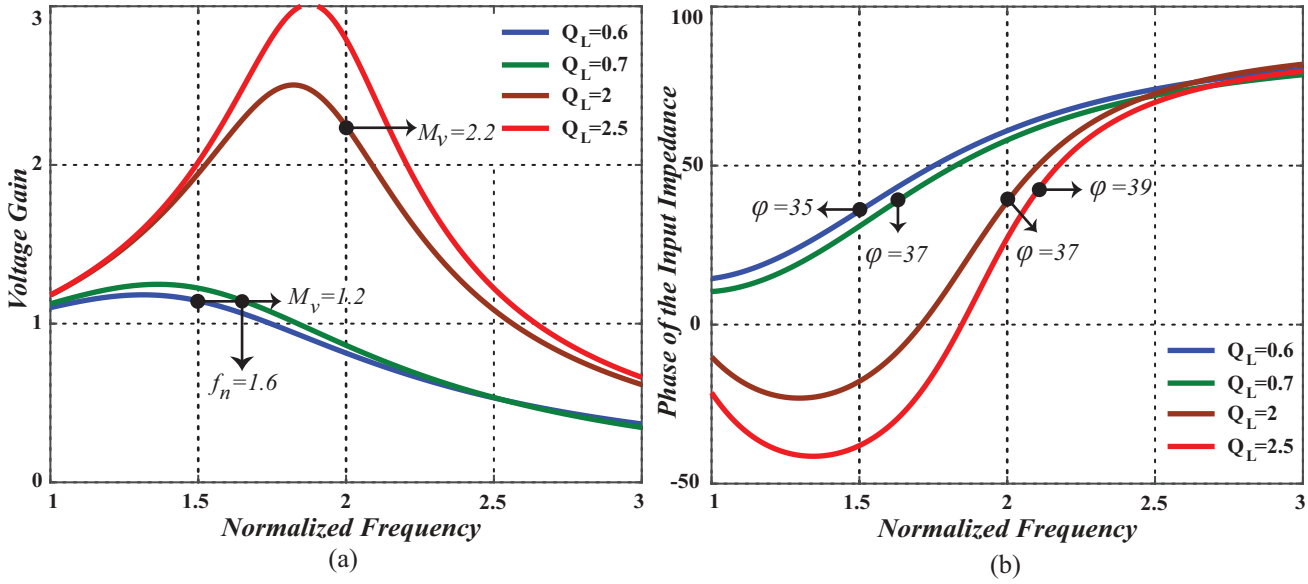

Figure 4.6: FHA analysis of the $L3C$ resonant converter for $L_n = 0.25$, and $L_s = 5$, with constant values for normalized load resistances (Q_L): (a) Magnitude of voltage transfer function (M_v), and (b) Phase of the input impedance (φ).

charger are presented in Table 4.1. According to Table 4.1, the resonant frequency is equal to $f_0 = 140kHz$. Therefore, the switching frequency is calculated using the following equation:

$$f_0 = 140kHz,\ f_n = 2,\ f_n = \frac{f_s}{f_0} \implies f_s = 2 \times 140 = 280kHz \tag{4.16}$$

The voltage gain at $f_n = 2$ (brown curve, $Q_L = 2$) for the nominal load conditions are given as follows:

$$M_v = 2\ for\ Q_L = 2,\ L_n = 0.25,\ L_s = 5 \tag{4.17}$$

Therefore, the parallel resonant capacitor voltage (output voltage) and transformer turns-ratio are calculated as follows:

Table 4.1: *L3C* Prototype Platform Parameters

Parameters	Value
Input Voltage, V_{in}	$24 - 45VDC$
Battery Voltage, $V'_{bat,n}$	$230 - 430VDC$
Maximum Output Power, P_{out}	$350W$
Switching Frequency Range, f_s	$150 - 350kHz$
Based Resonant Frequency, f_0	$140kHz$
First Series Resonant Inductance, L_{s_1}	$3.75\mu H$
Second Series Resonant Inductance, L_{s_2}	$0.7\mu H$
Parallel Resonant Inductance, L_p	$15\mu H$
Parallel Resonant Capacitance, C_s	$5nF$
Transformer Turn's Ratio, $n = \frac{N_p}{N_s}$	$4 : 18$

$$V_{bat,n} = M_v.V_{in} = 2.2 * 44.5 = 98VDC,\ n = \frac{N_p}{N_s} = \frac{V_{bat,n}}{V'_{bat,n}} \implies n = \frac{430}{98} = 4.4 \tag{4.18}$$

According to Eq. 4.11, the characteristic impedance and resonance frequency are given by:

$$R_L = \frac{{V_{bat}}^2}{P_{out}},\ Z_0 = \frac{R_L}{Q_L} \implies Z_0 = \frac{{V_{bat}}^2}{P_{out}Q_L} = 13.8\Omega,\ \omega_0 = \frac{\omega_s}{\omega_n} = 280\pi e^3 \tag{4.19}$$

Therefore, the resonant components are obtained as follows:

$$L = \frac{Z_0}{\omega_0} = 15.7\mu H,\ C_p = \frac{1}{Z_0.\omega_0} = 82nF,\ L_{s_1} = 3.75\mu H,\ L_p = 15\mu H,\ L_{s_2} = 0.7\mu H \tag{4.20}$$

The *L3C* resonant circuit parameters used in the experimental prototype are summarized in Table 4.1.

4.4 Experimental Results and Theory Validation

In order to investigate the performance of the proposed fourth order $L3C$ resonant converter for extreme input-output regulation, a prototype platform has been employed to extract the maximum obtainable coverage of Fig. 4.1(b) under minimum and maximum output voltage regulation. The components, which are used in the prototypes, are shown in Table 4.2. According to Table 4.1, the switching frequency range is between $150kHz$ and $350kHz$, and the frequency for maximum output power at maximum output voltage is set to be $280kHz$. Due to high current amplitude in the primary side, a high efficiency full-bridge inverter with low on-resistance MOSFET is used to convert the input DC voltage to a high-frequency AC voltage. The resonant tank consists of an external air-core inductor ($L_{ext} = 4.2\mu H$ series placed in the transformer's primary side), an external parallel capacitor (placed in the secondary side of the transformer), and the parasitic components of the transformer (including primary and secondary leakage inductances and magnetizing inductance). Figs. 4.7-4.10 show the experimental results for the minimum and maximum output voltage under different input voltage and input power conditions (maximum power point presented in Fig. 4.3). Each figure contains full-bridge inverter voltage, resonant circuit current, transformer secondary side voltage, and transformer secondary side current. Figs. 4.7-4.10 show the response of the $L3C$ resonant converter to variation of the input voltage, which are caused as a result of either changes in PV panel irradiance, or temperature. As mentioned in the introduction, the battery charger must be able to respond to different modes of the charge algorithms and track the input voltage variation in order to transfer the maximum available power. According to presented experimental results, the proposed fourth order $L3C$ resonant converter can regulate the output voltage in a wide range (($V_{bat} = 230 - 430VDC$)), and track the input voltage variation for extracting the maximum available power from PV panel

Table 4.2: Components Platform of the $L3C$ Resonant Converters

Component	$Part\,Number$	$Ratings$
MOSFET's	$STH240N10F$	$100VDC, 180A$
Resonant Cap.	$Film\,Cap.$	$8.2nF, 1600VDC$
Resonant Ind.	$AirCore$	$LitzWire$
Transformer	$3C95$	$RM14$
Rectifier Diode	$C3D04060$	$600VDC, 4A$
Output Capacitor	$Film\,Capacitor$	$1.5uF, 630VDC$

using the switching frequency modulation.

In order to provide soft switching conditions for power MOSFETs, the phase angle of the input impedance should be positive. According to experimental results, the zero crossings of the resonant circuit input current are within the inverter output voltage pulse and, as a result, in all of the conditions described, the full-bridge switches are fully turned on under zero voltage. On the other hand, to provide high-quality output voltage and maximize the converter efficiency, it is vital to realize soft commutation for the output rectifier diodes. Basically, the reverse recovery current of output rectifier diodes during the turn-off transition leads to high voltage peaks across output diodes and as a result, diodes with more withstand voltage should be selected, which means more conduction losses. According to the waveforms of the voltage and current on the secondary side of the transformer, ZCS is provided for output rectifier diodes, and the voltage peak is eliminated. As indicated in Figs. 4.7-4.10, in the end of the power transfer interval, once $i_{L_{s2}}$ reaches zero, the output diodes' current smoothly reaches zero. This causes ZCS at turn-off and avoids any reverse recovery losses in the output diodes. In addition, the voltage across the diodes is smooth and sinusoidal during the switching transitions which leads to minimum negative impact of the diode junction capacitance in transient time. As presented before in the converter analysis, the proposed

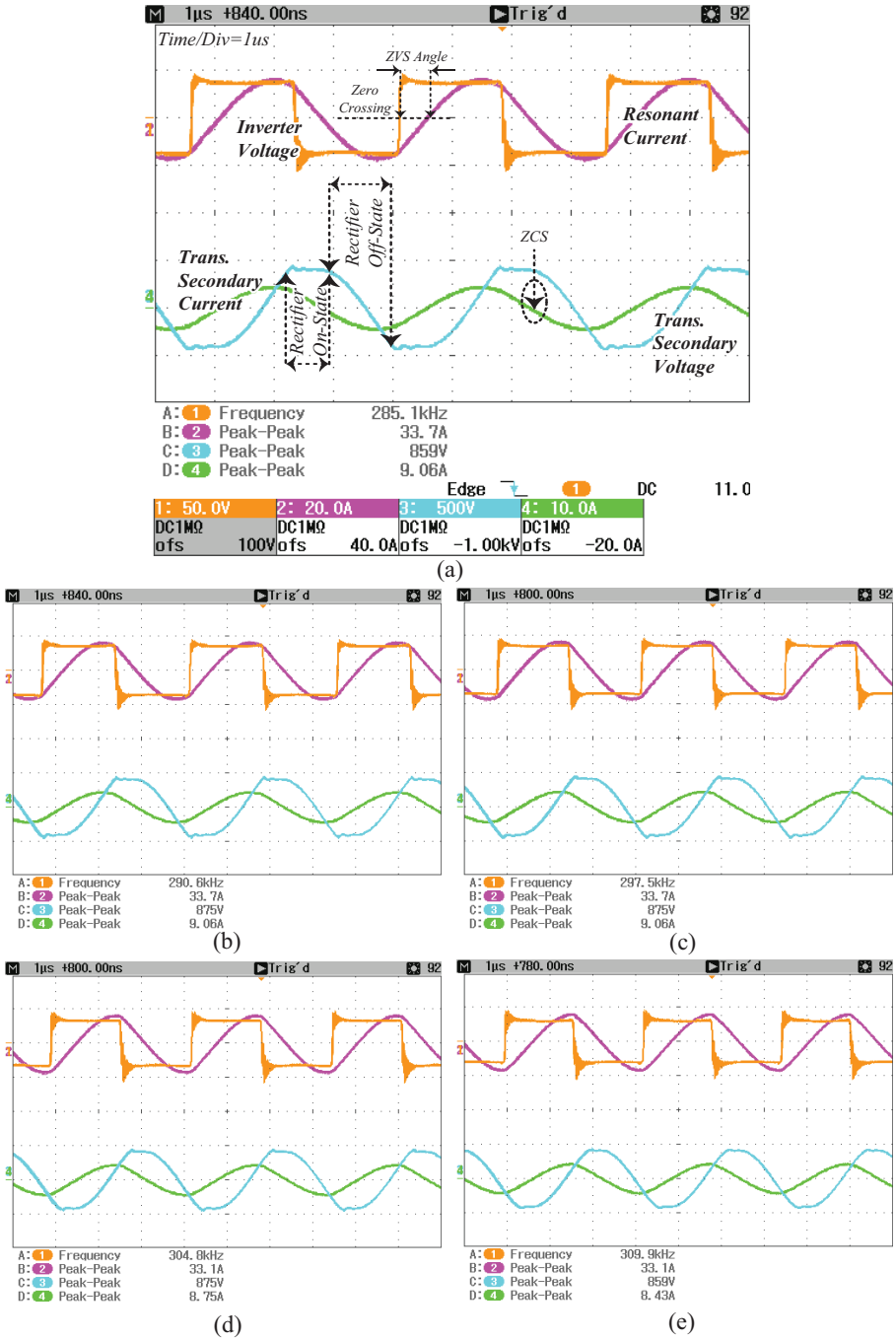

Figure 4.7: $L3C$ resonant converter experimental results for maximum battery voltage ($V'_{bat} = 430VDC$), fixed ambient temperature ($25°C$), and different irradiance: (a) $1000W/m^2$: $V_{in} = 37VDC$ and $P_{in} = 296W$, (b) $800W/m^2$: $V_{in} = 36VDC$ and $P_{in} = 232W$, (c) $600W/m^2$: $V_{in} = 35VDC$ and $P_{in} = 169W$, (d) $400W/m^2$: $V_{in} = 33VDC$ and $P_{in} = 108W$, and (e) $200W/m^2$: $V_{in} = 31VDC$ and $P_{in} = 50W$.

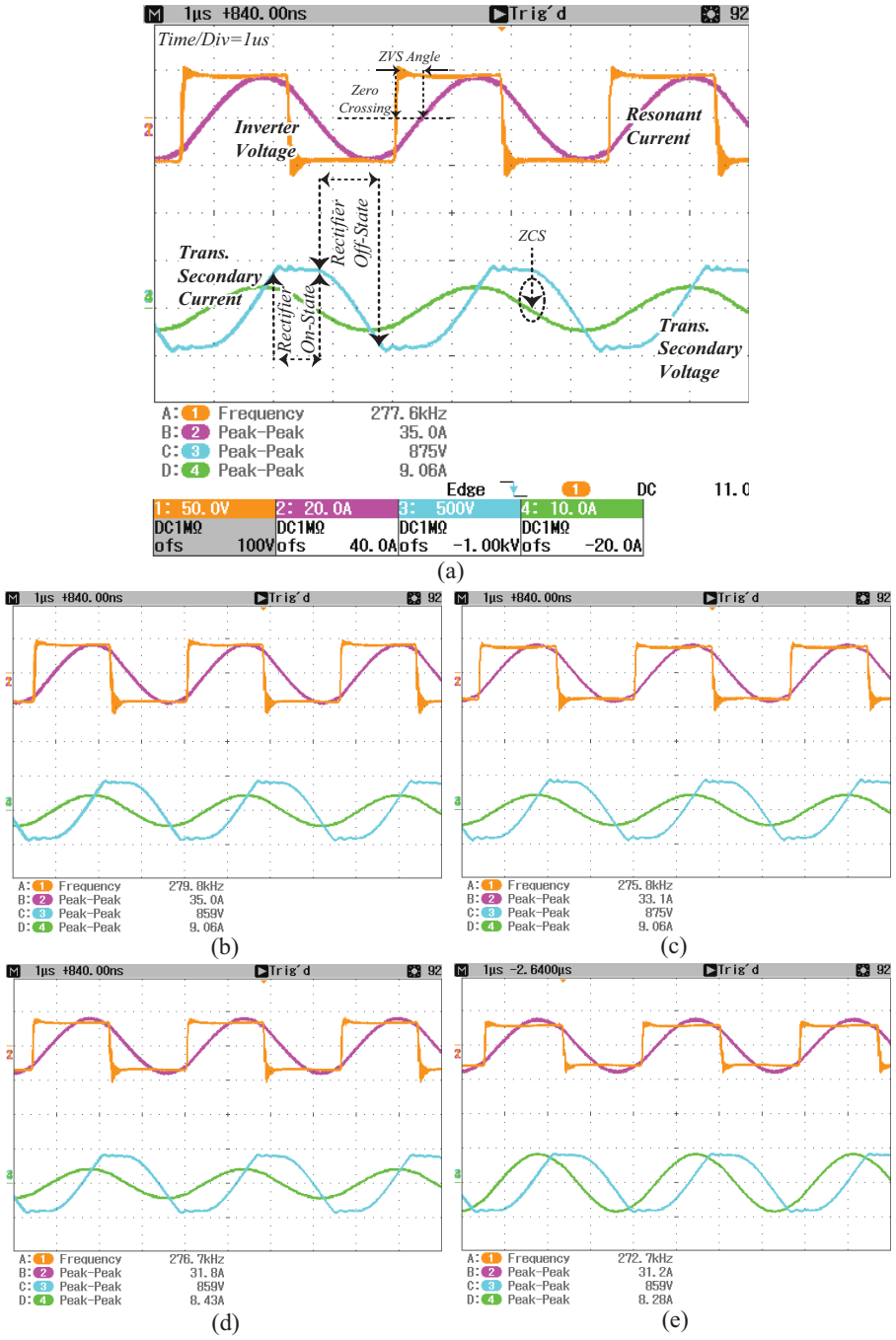

Figure 4.8: $L3C$ resonant converter experimental results for maximum battery voltage ($V'_{bat} = 430VDC$), fixed irradiance ($1000W/m^2$), and different temperature: (a) $-20°C$: $V_{in} = 45VDC$ and $P_{in} = 365W$, (b) $0°C$: $V_{in} = 41VDC$ and $P_{in} = 335W$, (c) $20°C$: $V_{in} = 37VDC$ and $P_{in} = 304W$, (d) $40°C$ $V_{in} = 34VDC$ and $P_{in} = 272W$, and (e) $60°C$ $V_{in} = 30VDC$ and $P_{in} = 241W$.

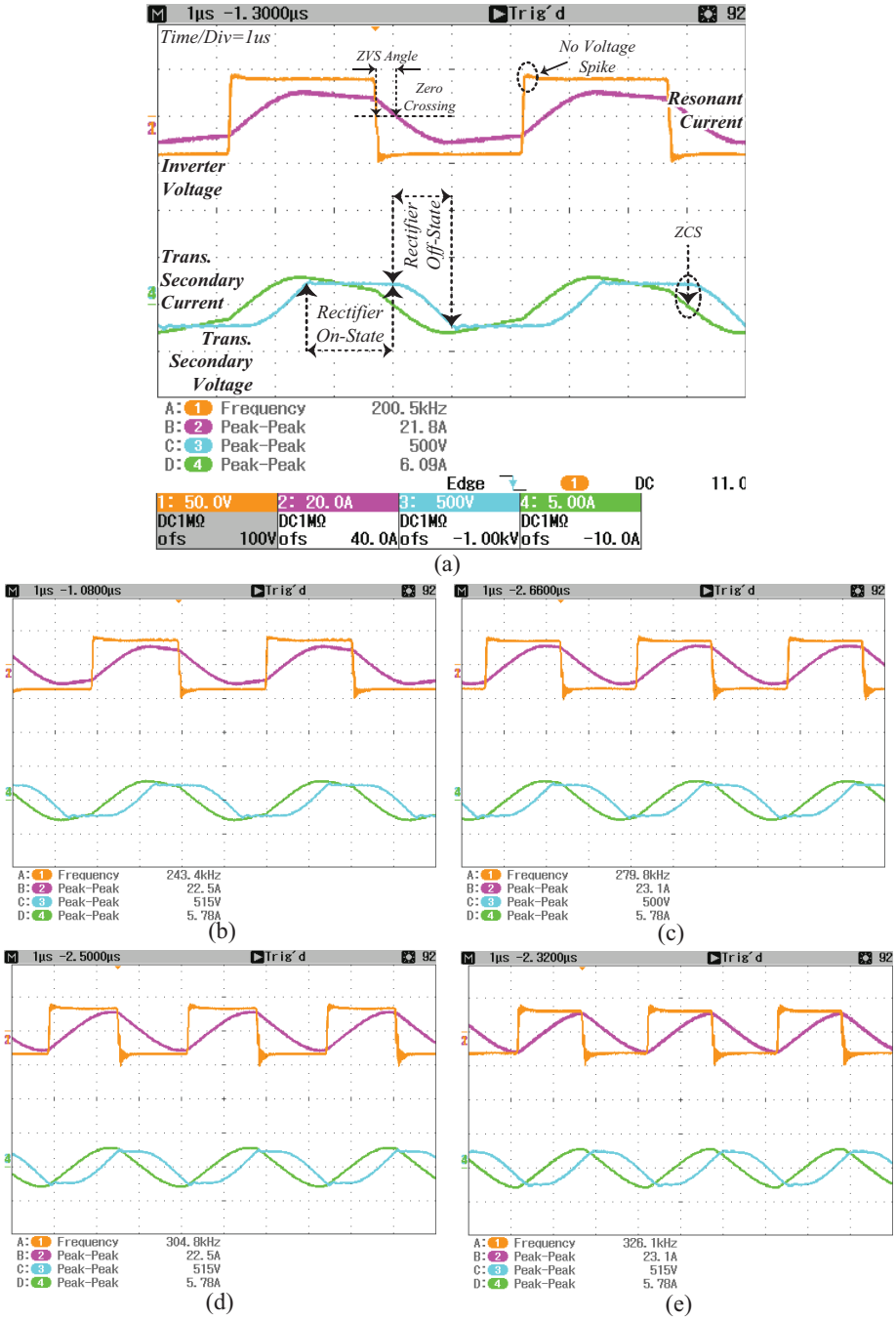

Figure 4.9: $L3C$ resonant converter experimental results for minimum battery voltage ($V'_{bat} = 230VDC$), fixed ambient temperature ($25°C$), and different irradiance: (a) $1000W/m^2$: $V_{in} = 37VDC$ and $P_{in} = 296W$, (b) $800W/m^2$: $V_{in} = 36VDC$ and $P_{in} = 232W$, (c) $600W/m^2$: $V_{in} = 35VDC$ and $P_{in} = 169W$, (d) $400W/m^2$: $V_{in} = 33VDC$ and $P_{in} = 108W$, and (e) $200W/m^2$: $V_{in} = 31VDC$ and $P_{in} = 50W$.

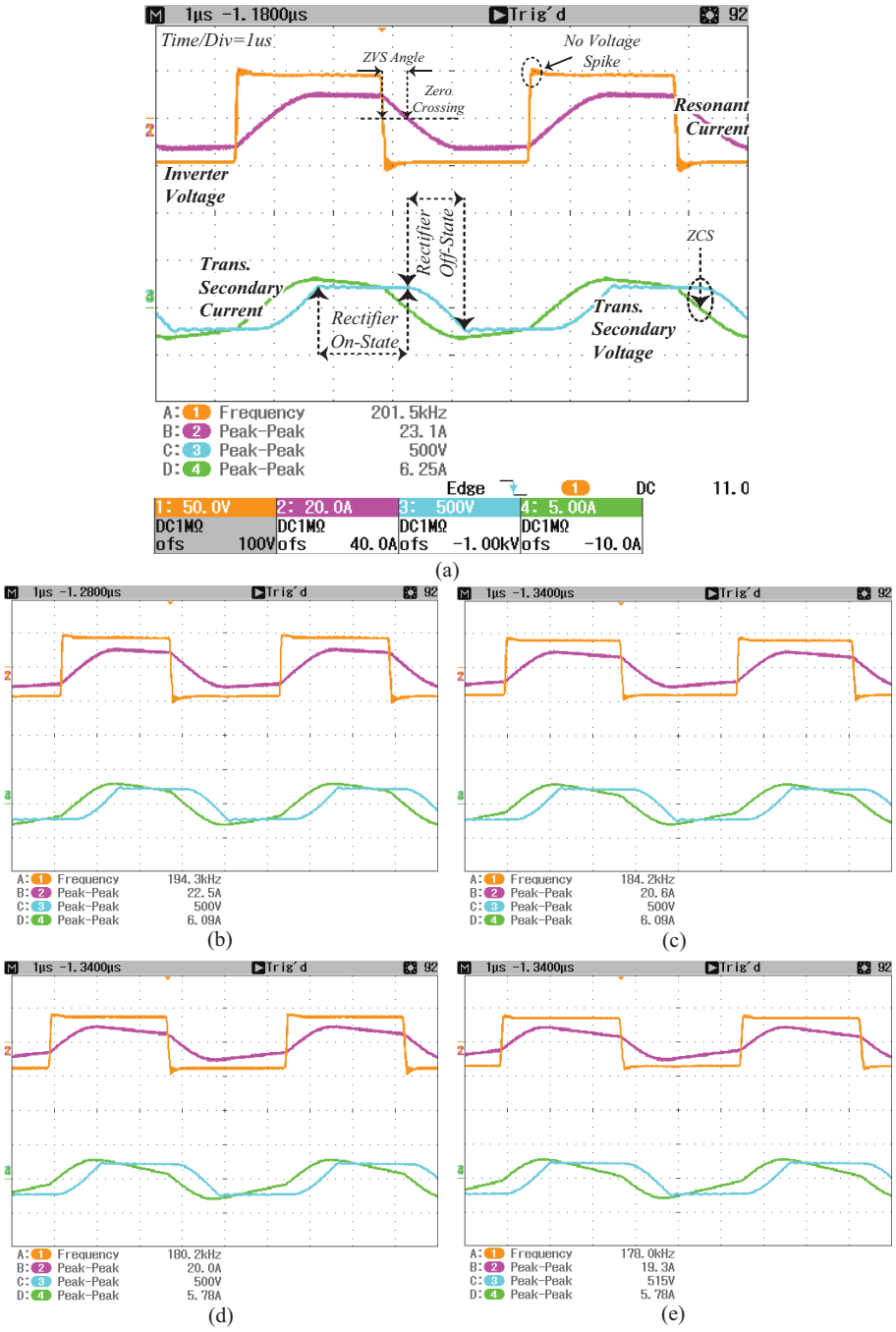

Figure 4.10: $L3C$ resonant converter experimental results for minimum battery voltage ($V'_{bat} = 230VDC$), fixed irradiance ($1000W/m^2$), and different temperature: (a) $-20°C$: $V_{in} = 45VDC$ and $P_{in} = 365W$, (b) $0°C$: $V_{in} = 41VDC$ and $P_{in} = 335W$, (c) $20°C$: $V_{in} = 37VDC$ and $P_{in} = 304W$, (d) $40°C$: $V_{in} = 34VDC$ and $P_{in} = 272W$, and (e) $60°C$: $V_{in} = 30VDC$ and $P_{in} = 241W$.

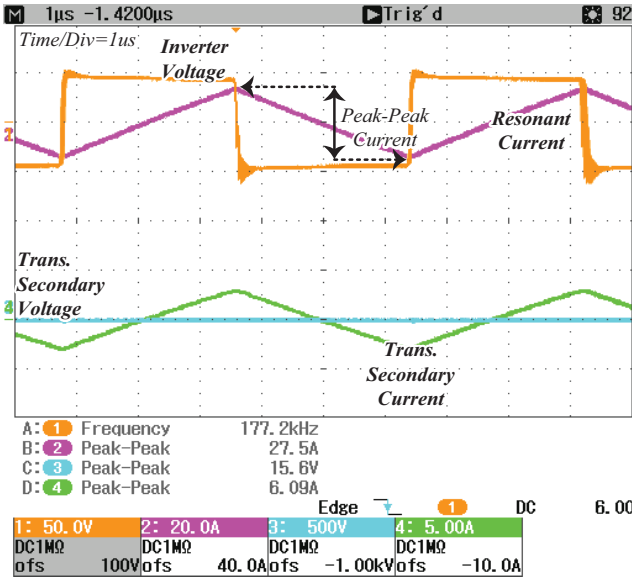

Figure 4.11: $L3C$ resonant converter short circuit test at minimum switching frequency ($f_s = 177kHz$) and maximum input voltage ($V_{in} = 44VDC$)

$L3C$ resonant converter has the capability to protect the full-bridge inverter from output over current and short circuit conditions. Fig. 4.11 presents the converter main waveforms under output short circuit condition and maximum input voltage condition. According to Fig. 4.11, the converter can safely work under output short circuit condition and protects the full bridge MOSFET, which can facilitate the control and protection circuit design. Fig. 4.12 presents the efficiency curves of the $L3C$ resonant converters for different input voltage and output voltages. Each point in Fig. 4.12 related to one experimental test, presented in Figs. 4.7-4.10. According to these curves, the resonant converters designed for this study present a maximum efficiency equal to 97.5%.

4.5 Summary

This chapter introduced the $L3C$ resonant power converter with extreme regulation capability, which can be employed as a battery charger for PV systems with high-voltage battery

banks. The main advantages of the proposed resonant converter are its ability to track input voltage variation of the PV panel, and regulate the output voltage in a wide range as the maximum power point continually changes. Despite other well-known resonant power converters (e.g. $LLC, LCC, LCLC$, $L3C2$), the proposed topology does not employ a series resonant capacitor in the primary side of the converter, which makes the charger design easier in terms of component selections. Also, soft switching of the MOSFETs and output rectifier diodes provide high efficiency, and the capability of working in high switching frequency. In spite of the fact that the $L3C$ resonant converter is able to provide an extreme regulation for PV to battery pack applications, the circulating current in the primary side of the $L3C$ resonant converter is higher than other studied resonant topologies (LLC, $L3C2$). Since this converter has very low resistance elements in the primary side, this circulating current does not affect the efficiency and just increases the current stress for the primary MOSFETs. Also, the high frequency transformer is very sensitive to any kind of mismatch for the primary gate signals (it becomes saturated). This means that the gate signals, which are applied to MOSFETs, have to be completely symmetrical, which necessitates having an accurate and similar driver for all gate signals.

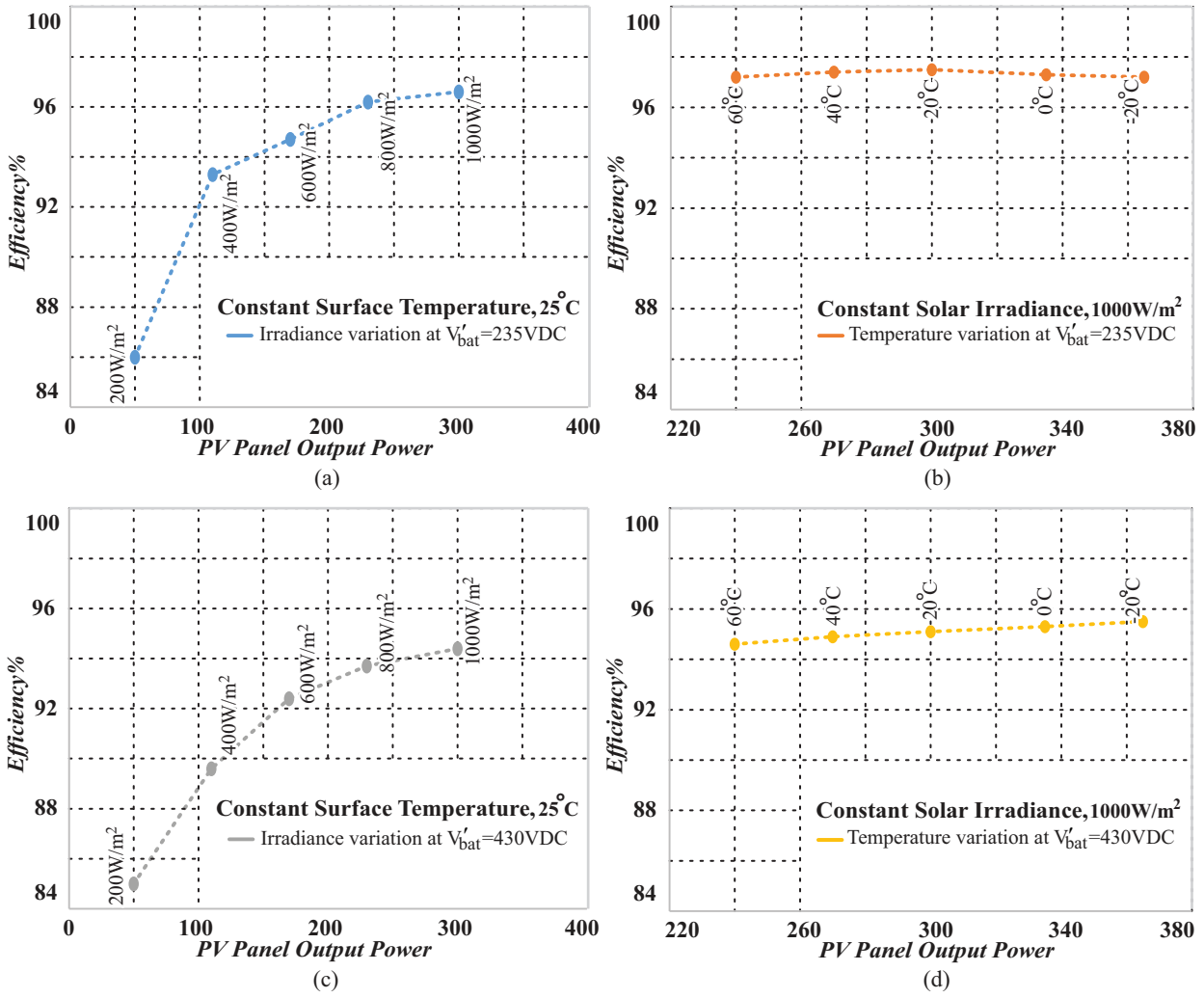

Figure 4.12: Efficiency curves of the $L3C$ resonant converter for different conditions, a) Efficiency for constant surface temperature ($25°C$) and irradiance variations at $V_{out} = 235VDC$, b) Efficiency for constant solar irradiance ($1000W/m^2$) and temperature variations at $V_{out} = 235VDC$, c) Efficiency for constant surface temperature ($25°C$) and irradiance variations at $V_{out} = 430VDC$, d) Efficiency for constant solar irradiance ($1000W/m^2$) and temperature variations at $V_{out} = 430VDC$.

Chapter 5

Conclusions

5.1 Conclusions and Contributions

To eliminate the negative effect of the burst mode strategy for medium and high power battery chargers and provide extreme regulation for solar battery chargers, this dissertation explored resonant converter topologies for DC-DC power converters. The proposed solutions can successfully be employed for battery charger applications, and can cover different power levels from low to high power applications.

5.1.1 Burst Mode Elimination in High Power LLC Resonant Battery Charger

In order to eliminate burst mode issues for high power battery charger applications, a special LLC tank design method driven by both Variable Frequency (VF) and Phase Shift (PS) modulation was introduced in Chapter 2 to achieve all the regulation requirements for high power battery charging applications. The design procedure was based on the multivariate design methodology and resulted in advantageous extreme regulation in the converter and the elimination of detrimental burst mode operation. The complete analysis of the resonant converter (higher order including leakage inductance), along with mathematical equations, were presented in order to optimize and select the normalized parameters of the LLC resonant converter. The main advantage of the LLC resonant converter with the proposed modulation

strategy is its ability to regulate the output voltage from near-zero volts up to 1.5 times the nominal voltage in continuous conduction mode with low switching frequency variation, while providing soft switching conditions for semiconductor devices in all operating conditions. The low-ripple output voltage enhanced the quality of the charging current for battery charger applications in all conditions, especially the recovery region, thereby providing a low-noise environment for the reliable operation of the Battery Management System. The experimental results extracted from a $3kW$ prototype platform proved that the LLC resonant converter with this special modulation strategy covered almost all regions in the V-I plane, and had a peak efficiency of 96.5%, which can be employed as a high power, wide voltage regulator for battery charger applications.

5.1.2 Improving the Regulation Range of EV Battery Chargers with $L3C2$ Resonant Converters

The second technical challenge, which was about DC-DC power converters for medium power level applications, was addressed in Chapter 3. Chapter 3 introduced the multi-resonant $L3C2$ resonant topology as a power converter for medium power level that can regulate the output voltage in a wide range, from near zero voltage, zero current to the maximum output power, without using burst mode operation. The complete analysis of the resonant converter along with mathematical equations were presented. The equations were able to precisely predict the behaviour of the converter. Due to wide output voltage regulation, the proposed resonant converter can respond to charge algorithms of different kinds of batteries, such as Lead-acid and Li-Ion and is a good candidate for use as a charger in electric vehicles. The main advantage of the proposed resonant converter is its ability to revitalize dead batteries in continuous conduction mode. The low-ripple output voltage enhances the quality of the charging current in the recovery region, thereby increasing the life cycle of the battery. Also,

soft switching of the MOSFETs and output rectifier diodes provide high efficiency, and the capability of working in high switching frequency without any limitation. The simulation and experimental results obtained from a $96VDC, 950W$ power platform verify the theoretical analysis and the performance of the proposed converter in terms of coverage in the V-I plane.

5.1.3 Fourth Order $L3C$ Resonant Converter for PV Battery Charger applications

The third contribution and technical challenge, which was about researching a power converter with extreme regulation for solar battery charger applications, was addressed in Chapter 4. Chapter 4 introduced the $L3C$ resonant power converter that can be employed as a battery charger for PV to battery applications. The main advantage of the proposed resonant converter is its ability to track the maximum power point of the PV panel, which can change due to solar irradiance and temperature variation, and regulate the output voltage in a wide range. Also, soft switching of the MOSFETs and output rectifier diodes provide high efficiency, and the capability of working in high switching frequency. Moreover, despite other well-known resonant power converter (e.g. $LLC, LCC, LCLC$, $L3C2$), the proposed topology does not employ a series resonant capacitor in the primary side of the converter, which makes the charger design easier in terms of component selections. The complete analysis of the resonant converter along with mathematical equations were presented. Also, the general equations for solar PV panel were extracted and employed to determine the variation of voltage-power characteristics of a PV module versus irradiance and temperature changes. The experimental results obtained from a $350W$ power platform verify the theoretical analysis and the performance of the proposed converter in terms of tracking the input voltage variations and wide output voltage regulation.

The concepts introduced in all chapters of this work were thoroughly tested experimentally

in order to prove the validation of the proposed resonant power converters and modulation strategies for battery charger applications. Although the proposed high-order resonant power converters can provide a ripple free charging current for battery packs, but due to the complexity of high-order resonant circuits the optimum design procedure is not straightforward and needs more efforts in comparison with third order resonant (LLC, LCC) and PWM-type converters.

5.1.4 Specific Academic Contributions

The work in this dissertation are reported in two journal publications and six international conference papers so far. The work encompasses applications from low to high power, and has presented the benefits outlined in this dissertation.

The following publication introduced modified LLC resonant converter for high power battery charger applications:

- **N. Shafiei**, M. Ordonez, M. Craciun, M. Edington, and C. Botting, "High power LLC battery charger: wide regulation using phase-shift for recovery mode," in *IEEE Energy Conversion Congress and Expo (ECCE)*, 2014, pp. 2037-2042. [1]

- **N. Shafiei**, M. Ordonez, M. Craciun, C. Botting, and M. Edington, "Burst mode elimination in high-power LLC resonant battery charger for electric vehicles," *IEEE Transactions on Power Electronics*, vol. 31, no. 2, pp. 1173-1188, Feb. 2016. [2]

The following publication introduced fifth order $L3C2$ resonant power converter for medium level power applications:

- **N. Shafiei**, M. Ordonez, W. Eberle, "Output rectifier analysis in parallel and series-parallel resonant converters with pure capacitive output filter," in *IEEE Applied Power Electronics Conference and Exposition (APEC)*, 2014, pp. 9-13. [3]

- **N. Shafiei**, M. Ordonez, "Improving the regulation range of EV battery chargers with *L3C2* resonant converters," *IEEE Transactions on Power Electronics*, vol. 30, no. 6, pp. 3166-3184, June 2015. [4]

The following publication introduced the *L3C* resonant power converter with high voltage gain for solar Photovoltaic applications:

- **N. Shafiei**, M. Ordonez, C. Botting, M. Craciun, and M. Edington, "Fourth order *L3C* resonant converter for wide output voltage regulation," in *IEEE Applied Power Electronics Conference and Exposition (APEC)*, 2015, pp. 1467-1471. [5]

The research on battery charger design procedure and optimization in resonant power converters resulted in the following publications:

- **N. Shafiei**, M. Ordonez, S. R. Cove, M. Craciun, and C. Botting, "Accurate modeling and design of *LLC* resonant converter with planar transformers," in 2015 IEEE Energy Conversion Congress and Exposition (ECCE), Sept 2015, pp. 5468-5473. [6]

- **N. Shafiei**, S. A. Arefifar, M. A. Saket, and M. Ordonez, "High efficiency *LLC* converter design for universal battery chargers," in 2016 IEEE Applied Power Electronics Conferenc eand Exposition (APEC), March 2016, pp. 2561-2566. [7]

Some publications resulted from collaborative research around magnetic design for planar transformers and high efficiency resonant power converters:

- A. Saket, **N. Shafiei**, and M. Ordonez, "*LLC* Converters with Planar Transformers: Issues and Mitigation," *IEEE Transactions on Power Electronics*, vol. 32, no. 6, pp. 4524-4542, June 2017. [128]

- S. Cove, M. Ordonez, **N. Shafiei**, and J. Zhu, "Improving wireless power transfer efficiency using hollow winding with track-width-ratio," *IEEE Transactions on Power Electronics*, vol. 31, no. 9, pp. 6524-6533, Sep. 2016. [129]

- A. Saket, **N. Shafiei**, and M. Ordonez, "Planar Transformers with Inherent Noise Cancellation for Flyback and Forward Converters," {*IEEE Transactions on Power Electronics*, Early Access.

- A. Saket, **N. Shafiei**, and M. Ordonez, "Planar transformer winding technique for reduced capacitance in *LLC* power converters," in 2016 IEEE Energy Conversion Congress and Exposition (ECCE), Sept 2016.

- A. Saket, **N. Shafiei**, and M. Ordonez, "Planar transformers with no common mode noise generation for flyback and forward converters," in 2016 IEEE Applied Power Electronics Conference and Exposition (APEC), March 2017.

- M. Mohammadi, **N. Shafiei**, and M. Ordonez, "*LLC* synchronous rectification using coordinate modulation," in 2016 IEEE Applied Power Electronics Conference and Exposition (APEC), March 2016, pp. 848-853. [130]

- A. Saket, **N. Shafiei**, and M. Ordonez, "Low parasitics planar transformer for *LLC* resonant battery charger," in 2016 IEEE Applied Power Electronics Conference and Exposition (APEC), March 2016, pp. 854-858. [131]

- Z. Qu, V. Dayal, J. Dong, R. Sangha, **N. Shafiei**, A. Arefifar, M. Ordonez, M. Craciun, C. Botting, "Comprehensive power MOSFET model for LLC resonant converter in renewable energy application," in 2016 IEEE Power Electronics for Distributed Generation Systems (PEDG), June 2016, pp. 1-5. [94]

5.2 Future Work

Although the main focus of this thesis was on DC-DC resonant power converters with extreme regulation with the specific application for electric vehicles, the proposed topologies

and modulation strategies can be employed in any energy system with rechargeable battery packs as a energy storage (e.g. renewable energy systems). This variety of battery chargers applications indicates the importance of more research and study on the area of DC-DC resonant power converters. This work opens up many full areas of research regarding design optimization, and performance improvement for Masters and PhD students. As a starting point for future work, some research has been done by the author on design optimization and performance improvement for DC-DC resonant power converter, which published in IEEE international conferences. [6, 7, 130, 132]

- Planar transformer applications for resonant converters: In order to design and fabricate low profile (slim) resonant converters, it is essential to replace conventional wire-wound magnetic transformers with low profile planar ones. In planar transformers, to decrease high-frequency AC resistance and leakage inductance, the primary and secondary windings are stacked together using the interleave structure method, which leads to a high amount of inter-winding and intra-winding capacitances. This topic opens a research area in the investigation of how to model planar transformers, how to eliminate the winding capacitance effects, and how to improve the fabrication process. A new model for LLC resonant converters has been presented based on fourth order model of the planar transformer [6].

- Optimized design of resonant converters: Due to wide operating frequency of resonant converters as a battery charger, it is important to propose a new methodology that focuses on multiple operating points rather than obtaining peak efficiency at one operating point. There are many degrees of freedom during design (such as the selection of resonant circuit elements, operating switching frequency, transformer specification, maximum achievable efficiency), which dictates an optimization algorithm in order to find the optimum values of the design variables. This topic opens a research area in the

investigation of optimum design procedures of resonant converters for battery charger applications. A new approach for designing an LLC resonant converter as a universal battery charger has been presented with wide conversion efficiency using Tabu Search algorithm [7].

- Time domain analysis of resonant converters: The current method for analyzing resonant topologies is called First Harmonic Approximation (FHA). This kind of modeling method is straightforward and can be employed for designing the resonant converter. However, this method only considers the fundamental frequency harmonic and is correct when the switching frequency variation is around the circuit resonant frequency. Due to the wide frequency variation in resonant converters for battery charger applications, the study of these type of circuits in the time domain is an opportunity to provide more accurate steady state analysis, which can lead to a more accurate design and optimization procedure [132].

- Resonant converter efficiency improvement: Although a resonant converter can provide soft switching condition for all semiconductor devices, which leads to have a better efficiency, conductive losses in the output rectifier is an obstacle for getting the highest possible efficiency at high output current applications. Due to different operating modes of resonant converters as battery chargers, another interesting topic as a future work could be the study of the synchronous rectifier for resonant converter with high output current applications. In [130], a new strategy referred to as Coordinate Modulation has been presented.

Appendices

Appendix A

Glossary

AC	Alternating Current.
BMS	Battery Management System.
DC	Direct Current.
EMI	Electro Magnetic Interference.
$FFPS$	Fixed Frequency Phase Shift.
LED	Light Emitting Diode.
$Li-Ion$	Lithium-Ion Battery.
$NiMH$	Nickel-Metal Hydride Battery.
PCB	Printed Circuit Board.
PFC	Power Factor Correction.
$PSPWM$	Phase Shift Pulse Width Modulation.
PWM	Pulse Width Modulation.
$PVPanel$	Photo Voltaic Panel.
VF	Variable Frequency.
ZCS	Zero Current Switching.
ZVS	Zero Voltage Switching.

Appendix B

Hard Switching versus Soft Switching

B.1 Hard Switching

Hard switching occurs when there is an overlap between the voltage and current when switching the semiconductor device on and off [133]. Fig. B.1 shows the switching transition and its instantaneous energy loss during the transient time (red area). This overlap causes power loss in the semiconductor device, which can be calculated by [134]:

$$P_{loss} = V_{DS} \times I_D \times f_{sw} \times (t_{on} + t_{off}) \tag{B.1}$$

According to Eq. (B.1), the switching frequency has a direct relationship with the power loss during the transient, which restricts the design of high efficiency and high power density converters. Hard-switching problems can be presented as follows:

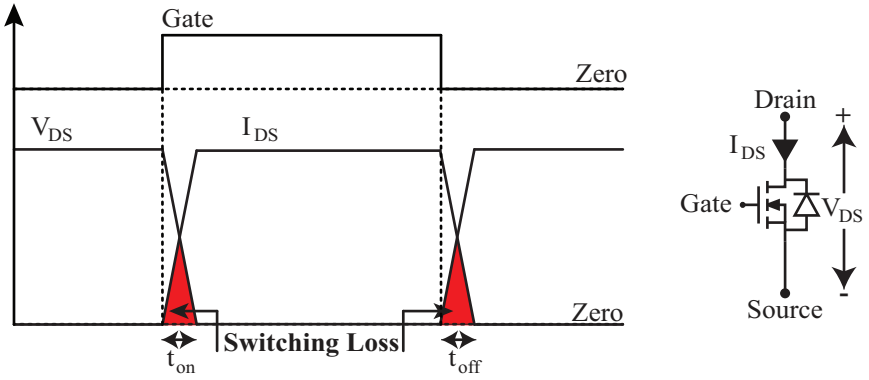

Figure B.1: Hard switching MOSFET current and voltage waveform.

- Switching losses.
- Low efficiency, especially at high switching frequency.
- Semiconductor stress.
- EMI due to high $\frac{dI_D}{dt}$ and $\frac{dV_{DS}}{dt}$

B.2 Soft Switching

The soft switching phenomenon happens when either voltage or current is forced to be zero before turning on or turning off the semiconductor device [133]. Fig. B.2 shows the switching transition of a soft switched semiconductor device. According to Fig. B.2, the semiconductor current is zero when the voltage across the device changes from its maximum to zero, or vice versa. Due to the elimination of overlap between the semiconductor voltage and current, the semiconductor power loss is eliminated and it is possible to design high efficiency power converters which can be run at higher frequency.

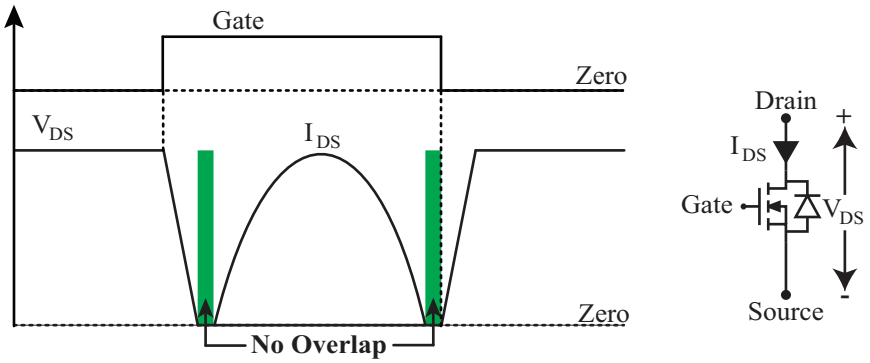

Figure B.2: Soft switching MOSFET current and voltage waveform.

B.3 Difference Between ZVS and ZCS

In order to provide soft switching for a semiconductor device, either the voltage or the current of the device has to be zero during transition. As both names imply either voltage or current within the transistor is zero before switching occurs. For the Zero Voltage Switching (ZVS), the semiconductor will be turned on at zero Drain-Source voltage to eliminate the turn on switching loss. For Zero Current Switching (ZCS), the semiconductor will be turned off at zero Drain current to eliminate the turn off switching loss [133].

Appendix C

Resonant Power Converters for Soft Switching

A resonant mode power converter offers the potential of achieving soft switching conditions for semiconductor devices and the possibility of increasing the switching frequency, which leads to a smaller, lighter, and less costly system [135]. With a resonant circuit in the power path, the switches can be configured to operate at either zero current or voltage switching, greatly reducing their stress levels. Also, the resonant sine wave minimizes higher frequency harmonics, thus reducing noise levels and, since the circuit now requires inductance and capacitance, parasitic elements can be integrated into the resonant circuit rather than detract from circuit performance [48, 135]. With these benefits, power converters operating in the range of 500 kHz to 2.0 MHz are now practical and are already being produced by a few leading edge manufacturers [136].

Fig. C.1(a) presents the general block diagram of the DC-DC resonant converter. The resonant circuit consists of a combination of inductors and capacitors in the power path between the input and output ports. By having the resonant circuit, the resonant circuit input current is filtered at the resonant frequency and therefore the current waveform is almost a pure sinusoidal one, which is demonstrated by Fig. C.1(b). This sinusoidal current flows through the inverter switches as well. By shaping the switch current, it is possible to provide a situation whereby each switch can operate at either the zero current or zero voltage. Since using MOSFETs is the preferred switch type for high frequency applications,

the resonant circuit has to represent an inductive load and the i_{res} lags behind the voltage v_{res} by the phase angle φ, where $\varphi > 0$ [48]. Because a power MOSFET is composed of a transistor and an anti-parallel diode, it is possible for this type of switch to conduct either a positive or negative current. Fig. C.2 presents the voltage and current waveforms of a single MOSFET operating in the inductive load condition. According to Fig. C.2, before applying the Gate signal, the switch current is negative and the anti-parallel diode is on, which means the Drain-Source voltage is maintained at about $-1V$ by the anti-parallel diode during the MOSFET turn-on transition. According to Fig. C.2, the Gate signal is applied after V_{DS} is brought to zero and before i_D passes zero and becomes positive. In this case, the turn-on switching loss is eliminated. In Fig. C.2, the correct time for applying the Gate signal is presented by the Zero Crossing term.

While resonant converters have several desired features such as high efficiency, low EMI and high power density, there are some drawbacks in comparison with PWM type power converters (e.g. Phase Shift Full Bridge PWM converter). Due to the sinusoidal shape of the current passing through all elements and semiconductor devices, the peak current is higher in resonant converters, which leads to more current stresses for all elements. Moreover, in no-load and light-load conditions, there is a circulating current passing through inverter switches and the resonant circuit. As a result of this circulating current, the efficiency curve for resonant converters is not as flat as PWM-type topologies. Also, the design of a resonant converter is an involved task, and requires more effort for optimization compared to PWM converters.

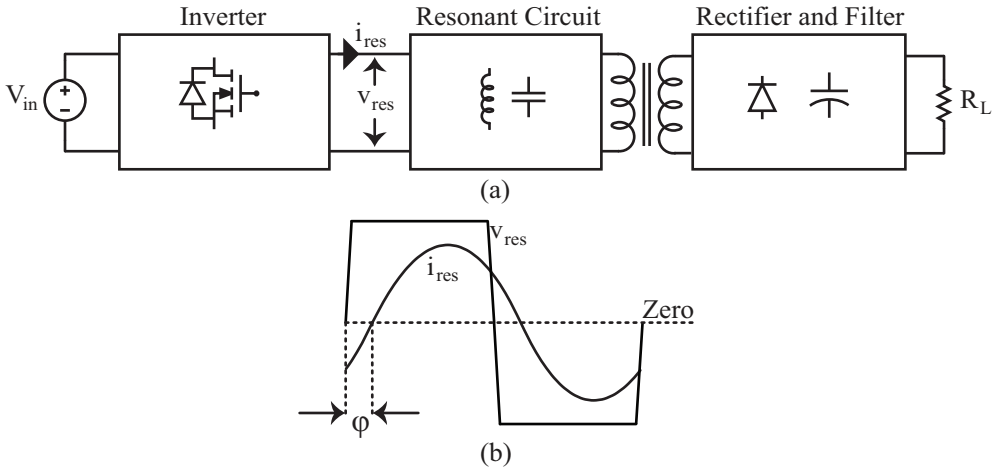

Figure C.1: (a) The general block diagram of the resonant power converters, (b) The voltage and current waveforms for the input of resonant circuit (inductive load condition).

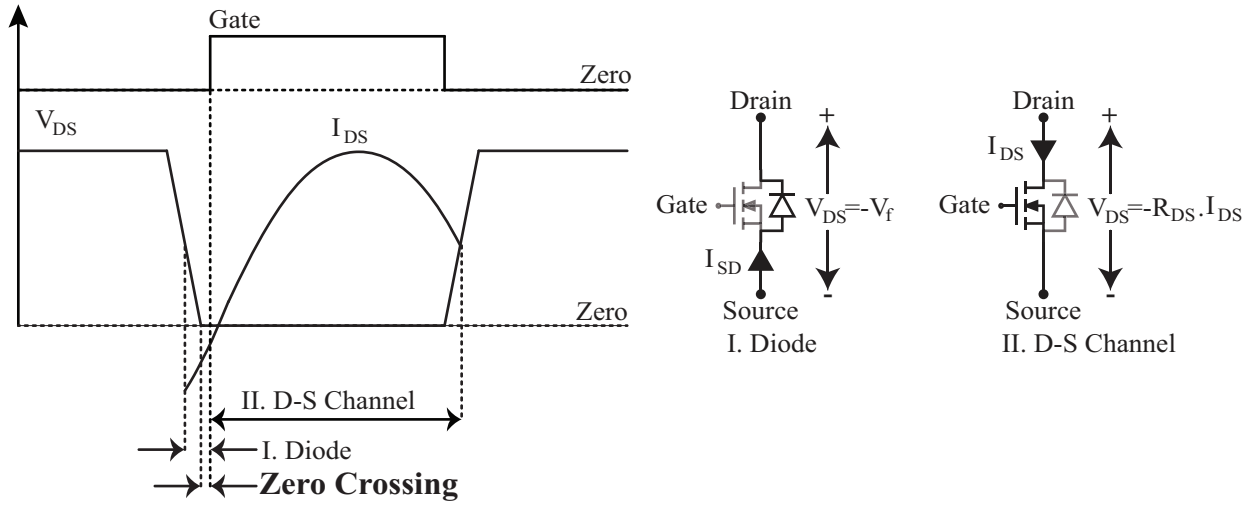

Figure C.2: Waveform of a MOSFET working at the inductive load condition.

Appendix D

Efficiency

D.1 Efficiency Calculation

In this work, efficiency curves are presented for different prototype platforms. In order to calculate the efficiency, the input and output powers need to be measured with a power meter and by employing Eq. (D.1), it is possible to calculate the efficiency. Fig. D.1 shows the input-output connections to/from power meter.

$$Efficiency = \frac{P_{out}}{P_{in}} = \frac{V_{out} \times I_{out}}{V_{in} \times I_{in}} \tag{D.1}$$

D.2 Higher Efficiency

In Power Electronics systems, the conversion mechanism generates heat as a result of non-ideal components (e.g. switching time of semiconductor devices and element resistances). This means a portion of the input power does not make it to the output of the system and heats up the components. This heat needs to be absorbed and transferred to the environment by a set of heat sinks and fans. If a power converter can be designed with higher efficiency, lower heat dissipation will happen, which not only facilitates the cooling system, but also shrinks the converter size due to the smaller required heat sink and fan. As an example, in Chapter 2 a 3kW resonant power converter is designed and tested with maximum efficiency of 96.5%, which means 109W of power dissipation. If the efficiency can be improved by only

1% (e.g. by employing the synchronous rectifier instead of the diode rectifier), the new power loss for the power converter will be 77W, which means 30% lower heat generation and a 30% smaller cooling system for the new converter.

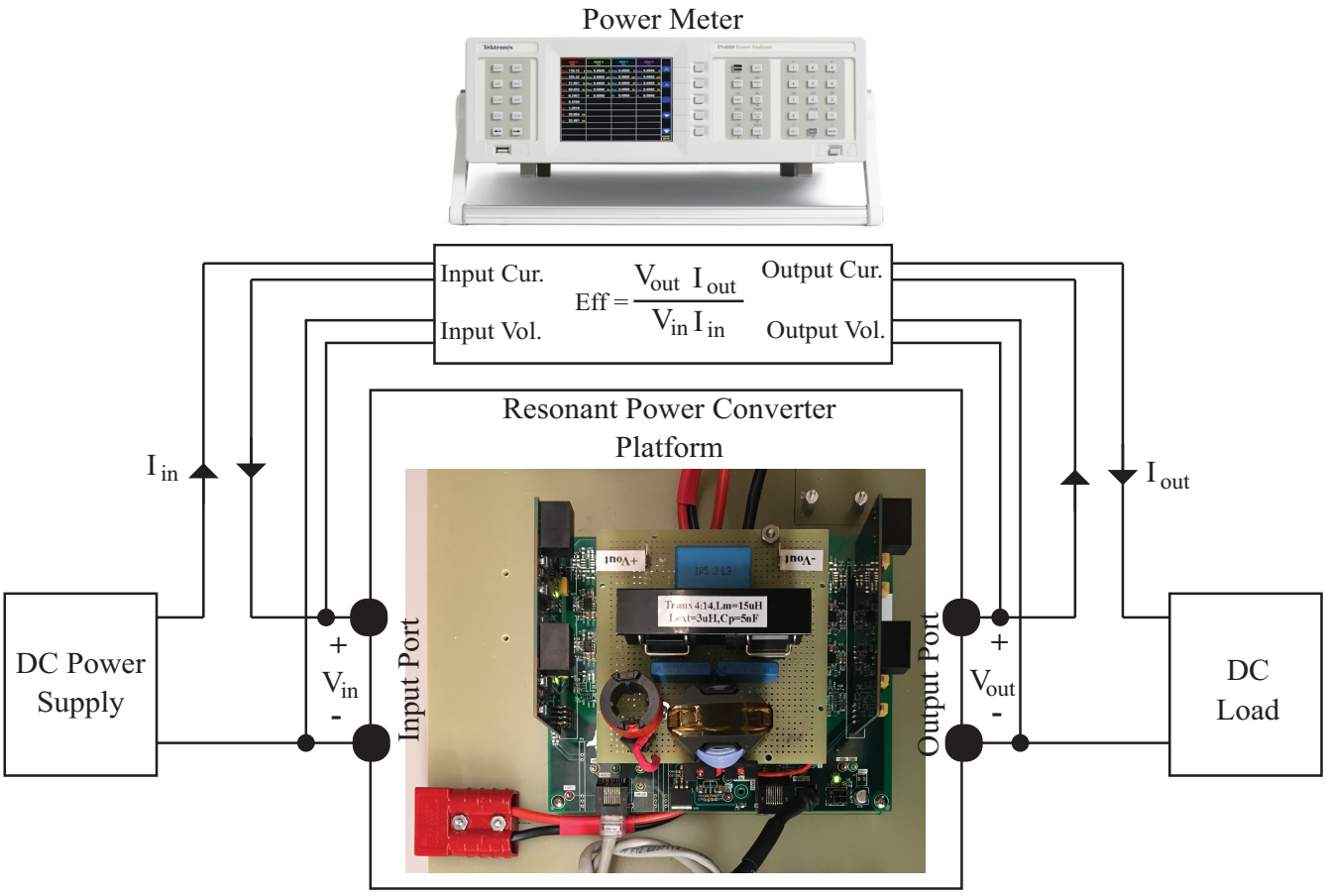

Figure D.1: The prototype input-output connection for the efficiency measurement

Bibliography

[1] N. Shafiei, M. Ordonez, M. Cracium, M. Edington, and C. Botting, "High power llc battery charger: Wide regulation using phase-shift for recovery mode," in *2014 IEEE Energy Conversion Congress and Exposition (ECCE)*, Sept 2014, pp. 2037–2042.

[2] N. Shafiei, M. Ordonez, M. Craciun, C. Botting, and M. Edington, "Burst mode elimination in high-power llc resonant battery charger for electric vehicles," *IEEE Transactions on Power Electronics*, vol. 31, no. 2, pp. 1173–1188, Feb 2016.

[3] N. Shafiei, M. Ordonez, and W. Eberle, "Output rectifier analysis in parallel and series-parallel resonant converters with pure capacitive output filter," in *2014 IEEE Applied Power Electronics Conference and Exposition - APEC 2014*, March 2014, pp. 9–13.

[4] N. Shafiei and M. Ordonez, "Improving the regulation range of ev battery chargers with l3c2 resonant converters," *IEEE Transactions on Power Electronics*, vol. 30, no. 6, pp. 3166–3184, June 2015.

[5] N. Shafiei, M. Ordonez, C. Botting, M. Craciun, and M. Edington, "Fourth order l3c resonant converter for wide output voltage regulation," in *2015 IEEE Applied Power Electronics Conference and Exposition (APEC)*, March 2015, pp. 1467–1471.

[6] N. Shafiei, M. Ordonez, S. R. Cove, M. Craciun, and C. Botting, "Accurate modeling and design of llc resonant converter with planar transformers," in *2015 IEEE Energy Conversion Congress and Exposition (ECCE)*, Sept 2015, pp. 5468–5473.

[7] N. Shafiei, S. A. Arefifar, M. A. Saket, and M. Ordonez, "High efficiency llc converter design for universal battery chargers," in *2016 IEEE Applied Power Electronics Conference and Exposition (APEC)*, March 2016, pp. 2561–2566.

[8] VIA Motors Inc., "Sltrux solar cover for the 2014 via vtrux," 2014, www.viamotors.com/vehicles/soltrux.

[9] M. Yilmaz and P. T. Krein, "Review of battery charger topologies, charging power levels, and infrastructure for plug-in electric and hybrid vehicles," *IEEE Transactions on Power Electronics*, vol. 28, no. 5, pp. 2151–2169, May 2013.

[10] A. Kuperman, U. Levy, J. Goren, A. Zafransky, and A. Savernin, "Battery charger for electric vehicle traction battery switch station," *IEEE Transactions on Industrial Electronics*, vol. 60, no. 12, pp. 5391–5399, Dec 2013.

[11] M. C. Wehrey, "What's new with hybrid electric vehicles," *IEEE Power and Energy Magazine*, vol. 2, no. 6, pp. 34–39, Nov 2004.

[12] Z. Amjadi and S. S. Williamson, "Digital control of a bidirectional dc/dc switched capacitor converter for hybrid electric vehicle energy storage system applications," *IEEE Transactions on Smart Grid*, vol. 5, no. 1, pp. 158–166, Jan 2014.

[13] K. P. Divakarla, S. Nalakath, M. Drennan, R. Ahmed, A. Emadi, and S. Razavi, "Battery characterization and state-of-charge prediction for different journey conditions with the help of the journey mapping concept," in *Industrial Electronics Society, IECON 2015 - 41st Annual Conference of the IEEE*, Nov 2015, pp. 003 683–003 688.

[14] F. Berthold, A. Ravey, B. Blunier, D. Bouquain, S. Williamson, and A. Miraoui, "Design and development of a smart control strategy for plug-in hybrid vehicles including

vehicle-to-home functionality," *IEEE Transactions on Transportation Electrification*, vol. 1, no. 2, pp. 168–177, Aug 2015.

[15] G. Zorpette, "Sun kings cross the outback [solar powered vehicles marathon]," *IEEE Spectrum*, vol. 39, no. 2, pp. 40–46, Feb 2002.

[16] R. R. Ahrabi, H. Ardi, m. elmi, and A. Ajami, "A novel step-up multi-input dc-dc converter for hybrid electric vehicles application," *IEEE Transactions on Power Electronics*, vol. PP, no. 99, pp. 1–1, 2016.

[17] I. O. Lee and G. W. Moon, "Half-bridge integrated zvs full-bridge converter with reduced conduction loss for electric vehicle battery chargers," *IEEE Transactions on Industrial Electronics*, vol. 61, no. 8, pp. 3978–3988, Aug 2014.

[18] E. Chemali, M. Preindl, P. Malysz, and A. Emadi, "Electrochemical and electrostatic energy storage and management systems for electric drive vehicles: State-of-the-art review and future trends," *IEEE Journal of Emerging and Selected Topics in Power Electronics*, vol. 4, no. 3, pp. 1117–1134, Sept 2016.

[19] S. H. Ryu, D. H. Kim, M. J. Kim, J. S. Kim, and B. K. Lee, "Adjustable frequency duty-cycle hybrid control strategy for full-bridge series resonant converters in electric vehicle chargers," *IEEE Transactions on Industrial Electronics*, vol. 61, no. 10, pp. 5354–5362, Oct 2014.

[20] S. Barcellona, F. Ciccarelli, D. Iannuzzi, and L. Piegari, "Modeling and parameter identification of lithium-ion capacitor modules," *IEEE Transactions on Sustainable Energy*, vol. 5, no. 3, pp. 785–794, July 2014.

[21] M. Bhatt, W. G. Hurley, and W. H. Wolfle, "A new approach to intermittent charging

of valve-regulated lead-acid batteries in standby applications," *IEEE Transactions on Industrial Electronics*, vol. 52, no. 5, pp. 1337–1342, Oct 2005.

[22] W. G. Hurley, Y. S. Wong, and W. H. Wolfle, "Self-equalization of cell voltages to prolong the life of vrla batteries in standby applications," *IEEE Transactions on Industrial Electronics*, vol. 56, no. 6, pp. 2115–2120, June 2009.

[23] A. Nourai, B. P. Martin, and D. R. Fitchett, "Testing the limits [electricity storage technologies]," *IEEE Power and Energy Magazine*, vol. 3, no. 2, pp. 40–46, March 2005.

[24] Trojan Battery Company, "Deep-cycle batteries users guide," 2013, www.trojanbattery.com.

[25] F. Musavi, M. Craciun, D. S. Gautam, W. Eberle, and W. G. Dunford, "An llc resonant dc-dc converter for wide output voltage range battery charging applications," *IEEE Transactions on Power Electronics*, vol. 28, no. 12, pp. 5437–5445, Dec 2013.

[26] F. Musavi, M. Craciun, D. S. Gautam, and W. Eberle, "Control strategies for wide output voltage range llc resonant dc dc converters in battery chargers," *IEEE Transactions on Vehicular Technology*, vol. 63, no. 3, pp. 1117–1125, March 2014.

[27] J. Deng, S. Li, S. Hu, C. C. Mi, and R. Ma, "Design methodology of llc resonant converters for electric vehicle battery chargers," *IEEE Transactions on Vehicular Technology*, vol. 63, no. 4, pp. 1581–1592, May 2014.

[28] M. Pahlevaninezhad, P. Das, J. Drobnik, P. K. Jain, and A. Bakhshai, "A novel zvzcs full-bridge dc/dc converter used for electric vehicles," *IEEE Transactions on Power Electronics*, vol. 27, no. 6, pp. 2752–2769, June 2012.

[29] H. Wang, S. Dusmez, and A. Khaligh, "Maximum efficiency point tracking technique for llc -based pev chargers through variable dc link control," *IEEE Transactions on Industrial Electronics*, vol. 61, no. 11, pp. 6041–6049, Nov 2014.

[30] Fairchild Semiconductor Corporation, "An-9721 li-ion battery charging basics, featuring the fan5400/fan 5420 family of pwm battery chargers," 2010, fairchild Semiconductor Corporation, Rev. 1.0.0.

[31] F. Musavi, M. Craciun, D. Gautam, M. Edington, W. Eberle, and W. G. Dunford, "Control strategies for a llc multi-resonant dc-dc converter in battery charging applications," in *Applied Power Electronics Conference and Exposition (APEC), 2013 Twenty-Eighth Annual IEEE*, March 2013, pp. 1804–1811.

[32] F. Musavi, M. Craciun, M. Edington, W. Eberle, and W. G. Dunford, "Practical design considerations for a llc multi-resonant dc-dc converter in battery charging applications," in *2012 Twenty-Seventh Annual IEEE Applied Power Electronics Conference and Exposition (APEC)*, Feb 2012, pp. 2596–2602.

[33] M. Pahlevaninezhad, P. Das, J. Drobnik, G. Moschopoulos, P. K. Jain, and A. Bakhshai, "A nonlinear optimal control approach based on the control-lyapunov function for an ac/dc converter used in electric vehicles," *IEEE Transactions on Industrial Informatics*, vol. 8, no. 3, pp. 596–614, Aug 2012.

[34] M. Pahlevaninezhad, P. Das, J. Drobnik, P. K. Jain, and A. Bakhshai, "A zvs interleaved boost ac/dc converter used in plug-in electric vehicles," *IEEE Transactions on Power Electronics*, vol. 27, no. 8, pp. 3513–3529, Aug 2012.

[35] Y. J. Lee, A. Khaligh, and A. Emadi, "Advanced integrated bidirectional ac/dc and dc/dc converter for plug-in hybrid electric vehicles," *IEEE Transactions on Vehicular Technology*, vol. 58, no. 8, pp. 3970–3980, Oct 2009.

[36] A. Khaligh, A. M. Rahimi, and A. Emadi, "Modified pulse-adjustment technique to control dc/dc converters driving variable constant-power loads," *IEEE Transactions on Industrial Electronics*, vol. 55, no. 3, pp. 1133–1146, March 2008.

[37] R. Erickson and D. Maksimovic, *Fundamentals of Power Electronics*, 2nd edition, Ed. Norwell, MA, USA: Kluwer, 2001.

[38] R. Hou and A. Emadi, "Applied integrated active filter auxiliary power module for electrified vehicles with single-phase onboard chargers," *IEEE Transactions on Power Electronics*, vol. PP, no. 99, pp. 1–1, 2016.

[39] Z. Sun, F. Peng, P. Magne, and A. Emadi, "A phase shifted full bridge converter with zcs synchronous rectifier for auxiliary power units," in *IECON 2014 - 40th Annual Conference of the IEEE Industrial Electronics Society*, Oct 2014, pp. 2945–2951.

[40] P. O'Neill, J. Zhang, and W. G. Hurley, "A phase-shifted full-bridge zvs dc/dc converter for wireless charging of electric vehicles," in *Power Engineering Conference (UPEC), 2015 50th International Universities*, Sept 2015, pp. 1–5.

[41] R. Hou and A. Emadi, "Dual active bridge-based full-integrated active filter auxiliary power module for electrified vehicle applications with single-phase onboard chargers," in *2016 IEEE Applied Power Electronics Conference and Exposition (APEC)*, March 2016, pp. 1300–1306.

[42] R. Hou, P. Magne, B. Bilgin, and A. Emadi, "A topological evaluation of isolated dc/dc converters for auxiliary power modules in electrified vehicle applications," in *2015 IEEE Applied Power Electronics Conference and Exposition (APEC)*, March 2015, pp. 1360–1366.

[43] D. S. Gautam, F. Musavi, M. Edington, W. Eberle, and W. G. Dunford, "An automotive onboard 3.3-kw battery charger for phev application," *IEEE Transactions on Vehicular Technology*, vol. 61, no. 8, pp. 3466–3474, Oct 2012.

[44] D. S. Gautam, F. Musavi, W. Eberle, and W. G. Dunford, "A zero-voltage switching full-bridge dc–dc converter with capacitive output filter for plug-in hybrid electric vehicle battery charging," *IEEE Transactions on Power Electronics*, vol. 28, no. 12, pp. 5728–5735, Dec 2013.

[45] M. Pahlevaninezhad, S. Eren, P. K. Jain, and A. Bakhshai, "Self-sustained oscillating control technique for current-driven full-bridge dc/dc converter," *IEEE Transactions on Power Electronics*, vol. 28, no. 11, pp. 5293–5310, Nov 2013.

[46] B. Gu, C. Y. Lin, B. Chen, J. Dominic, and J. S. Lai, "Zero-voltage-switching pwm resonant full-bridge converter with minimized circulating losses and minimal voltage stresses of bridge rectifiers for electric vehicle battery chargers," *IEEE Transactions on Power Electronics*, vol. 28, no. 10, pp. 4657–4667, Oct 2013.

[47] T. Mishima, K. Akamatsu, and M. Nakaoka, "A high frequency-link secondary-side phase-shifted full-range soft-switching pwm dc dc converter with zcs active rectifier for ev battery chargers," *IEEE Transactions on Power Electronics*, vol. 28, no. 12, pp. 5758–5773, Dec 2013.

[48] D. C. Marian K. Kazimierczuk, *Resonant Power Converters*, 2nd Edition, Ed. Wiley-IEEE Press, 2011.

[49] R. L. Steigerwald, "A comparison of half-bridge resonant converter topologies," *IEEE Transactions on Power Electronics*, vol. 3, no. 2, pp. 174–182, Apr 1988.

[50] C. H. Chang, E. C. Chang, and H. L. Cheng, "A high-efficiency solar array simulator implemented by an llc resonant dc dc converter," *IEEE Transactions on Power Electronics*, vol. 28, no. 6, pp. 3039–3046, June 2013.

[51] H. Wang and A. Khaligh, "Comprehensive topological analyses of isolated resonant converters in pev battery charging applications," in *Transportation Electrification Conference and Expo (ITEC), 2013 IEEE*, June 2013, pp. 1–7.

[52] H. Hu, X. Fang, F. Chen, Z. J. Shen, and I. Batarseh, "A modified high-efficiency llc converter with two transformers for wide input-voltage range applications," *IEEE Transactions on Power Electronics*, vol. 28, no. 4, pp. 1946–1960, April 2013.

[53] J.-S. Kim, G.-Y. Choe, H.-M. Jung, B.-K. Lee, Y.-J. Cho, and K.-B. Han, "Design and implementation of a high-efficiency on- board battery charger for electric vehicles with frequency control strategy," in *2010 IEEE Vehicle Power and Propulsion Conference*, Sept 2010, pp. 1–6.

[54] H. S. Kim, J. W. Baek, M. H. Ryu, J. H. Kim, and J. H. Jung, "The high-efficiency isolated ac dc converter using the three-phase interleaved llc resonant converter employing the y-connected rectifier," *IEEE Transactions on Power Electronics*, vol. 29, no. 8, pp. 4017–4028, Aug 2014.

[55] T. Jiang, J. Zhang, X. Wu, K. Sheng, and Y. Wang, "A bidirectional llc resonant converter with automatic forward and backward mode transition," *IEEE Transactions on Power Electronics*, vol. 30, no. 2, pp. 757–770, Feb 2015.

[56] J. W. Kim and G. W. Moon, "A new llc series resonant converter with a narrow switching frequency variation and reduced conduction losses," *IEEE Transactions on Power Electronics*, vol. 29, no. 8, pp. 4278–4287, Aug 2014.

[57] X. Fang, H. Hu, Z. J. Shen, and I. Batarseh, "Operation mode analysis and peak gain approximation of the llc resonant converter," *IEEE Transactions on Power Electronics*, vol. 27, no. 4, pp. 1985–1995, April 2012.

[58] J. Channegowda, V. K. Pathipati, and S. S. Williamson, "Comprehensive review and comparison of dc fast charging converter topologies: Improving electric vehicle plug-to-wheels efficiency," in *2015 IEEE 24th International Symposium on Industrial Electronics (ISIE)*, June 2015, pp. 263–268.

[59] J. Zhang, W. G. Hurley, and W. H. Wlfle, "Design of the planar transformer in llc resonant converters for micro-grid applications," in *2014 IEEE 5th International Symposium on Power Electronics for Distributed Generation Systems (PEDG)*, June 2014, pp. 1–7.

[60] M. Almardy and A. K. S. Bhat, "A comparison of three-phase high-frequency transformer isolated lcc and lcl-type dc-dc resonant converter topologies," in *2015 9th International Conference on Power Electronics and ECCE Asia (ICPE-ECCE Asia)*, June 2015, pp. 1513–1520.

[61] X. Fang, H. Hu, F. Chen, U. Somani, E. Auadisian, J. Shen, and I. Batarseh, "Efficiency-oriented optimal design of the llc resonant converter based on peak gain placement," *IEEE Transactions on Power Electronics*, vol. 28, no. 5, pp. 2285–2296, May 2013.

[62] S. A. Singh, N. A. Azeez, and S. S. Williamson, "A new single-stage high-efficiency photovoltaic(pv)/grid-interconnected dc charging system for transportation electrification," in *Industrial Electronics Society, IECON 2015 - 41st Annual Conference of the IEEE*, Nov 2015, pp. 005 374–005 380.

[63] X. Fang, H. Hu, L. Chen, A. Amirahmadi, J. Shen, and I. Batarseh, "Operation analysis and numerical approximation for the llc dc-dc converter," in *2012 Twenty-Seventh Annual IEEE Applied Power Electronics Conference and Exposition (APEC)*, Feb 2012, pp. 870–876.

[64] B. H. Lee, M. Y. Kim, C. E. Kim, K. B. Park, and G. W. Moon, "Analysis of llc resonant converter considering effects of parasitic components," in *INTELEC 2009 - 31st International Telecommunications Energy Conference*, Oct 2009, pp. 1–6.

[65] S. Zhao, J. Xu, and O. Trescases, "Burst-mode resonant llc converter for an led luminaire with integrated visible light communication for smart buildings," *IEEE Transactions on Power Electronics*, vol. 29, no. 8, pp. 4392–4402, Aug 2014.

[66] W. Feng, F. C. Lee, and P. Mattavelli, "Optimal trajectory control of llc resonant converters for led pwm dimming," *IEEE Transactions on Power Electronics*, vol. 29, no. 2, pp. 979–987, Feb 2014.

[67] L. Zhang, W. G. Hurley, and W. H. Wlfle, "A new approach to achieve maximum power point tracking for pv system with a variable inductor," *IEEE Transactions on Power Electronics*, vol. 26, no. 4, pp. 1031–1037, April 2011.

[68] M. Das and V. Agarwal, "Design and analysis of a high-efficiency dc dc converter with soft switching capability for renewable energy applications requiring high voltage gain," *IEEE Transactions on Industrial Electronics*, vol. 63, no. 5, pp. 2936–2944, May 2016.

[69] L. Mller and J. W. Kimball, "High gain dc dc converter based on the cockcroft walton multiplier," *IEEE Transactions on Power Electronics*, vol. 31, no. 9, pp. 6405–6415, Sept 2016.

[70] W. Li and X. He, "Review of nonisolated high-step-up dc/dc converters in photovoltaic

grid-connected applications," *IEEE Transactions on Industrial Electronics*, vol. 58, no. 4, pp. 1239–1250, April 2011.

[71] X. Hu and C. Gong, "A high voltage gain dc dc converter integrating coupled-inductor and diode capacitor techniques," *IEEE Transactions on Power Electronics*, vol. 29, no. 2, pp. 789–800, Feb 2014.

[72] G. Wu, X. Ruan, and Z. Ye, "Nonisolated high step-up dc dc converters adopting switched-capacitor cell," *IEEE Transactions on Industrial Electronics*, vol. 62, no. 1, pp. 383–393, Jan 2015.

[73] X. Hu and C. Gong, "A high gain input-parallel output-series dc/dc converter with dual coupled inductors," *IEEE Transactions on Power Electronics*, vol. 30, no. 3, pp. 1306–1317, March 2015.

[74] Y. Tang, D. Fu, T. Wang, and Z. Xu, "Hybrid switched-inductor converters for high step-up conversion," *IEEE Transactions on Industrial Electronics*, vol. 62, no. 3, pp. 1480–1490, March 2015.

[75] G. Carli and S. S. Williamson, "Technical considerations on power conversion for electric and plug-in hybrid electric vehicle battery charging in photovoltaic installations," *IEEE Transactions on Power Electronics*, vol. 28, no. 12, pp. 5784–5792, Dec 2013.

[76] S. A. Singh and S. S. Williamson, "Comprehensive review of pv/ev/grid integration power electronic converter topologies for dc charging applications," in *Transportation Electrification Conference and Expo (ITEC), 2014 IEEE*, June 2014, pp. 1–5.

[77] Underwrites Laboratories Inc., "Ul60950: Safety of information technology equipment," 2000, third edition.

[78] Underwrites Laboratories, "Ul1741: Inverters, converters, controllers and interconnection system equipment for use with distributed energy resources," 2010.

[79] M. A. Rezaei, K. J. Lee, and A. Q. Huang, "A high-efficiency flyback micro-inverter with a new adaptive snubber for photovoltaic applications," *IEEE Transactions on Power Electronics*, vol. 31, no. 1, pp. 318–327, Jan 2016.

[80] Y. C. Hsieh, M. R. Chen, and H. L. Cheng, "An interleaved flyback converter featured with zero-voltage transition," *IEEE Transactions on Power Electronics*, vol. 26, no. 1, pp. 79–84, Jan 2011.

[81] Y. Shi, R. Li, Y. Xue, and H. Li, "Optimized operation of current-fed dual active bridge dc dc converter for pv applications," *IEEE Transactions on Industrial Electronics*, vol. 62, no. 11, pp. 6986–6995, Nov 2015.

[82] Y. H. Kim, S. C. Shin, J. H. Lee, Y. C. Jung, and C. Y. Won, "Soft-switching current-fed push pull converter for 250-w ac module applications," *IEEE Transactions on Power Electronics*, vol. 29, no. 2, pp. 863–872, Feb 2014.

[83] F. Evran and M. T. Aydemir, "Isolated high step-up dc dc converter with low voltage stress," *IEEE Transactions on Power Electronics*, vol. 29, no. 7, pp. 3591–3603, July 2014.

[84] N. Naghizadeh and S. S. Williamson, "A comprehensive review of power electronic converter topologies to integrate photovoltaics (pv), ac grid, and electric vehicles," in *Transportation Electrification Conference and Expo (ITEC), 2013 IEEE*, June 2013, pp. 1–6.

[85] M. Cacciato, A. Consoli, R. Attanasio, and F. Gennaro, "Soft-switching converter

with hf transformer for grid-connected photovoltaic systems," *IEEE Transactions on Industrial Electronics*, vol. 57, no. 5, pp. 1678–1686, May 2010.

[86] U. R. Prasanna, A. K. Rathore, and S. K. Mazumder, "Novel zero-current-switching current-fed half-bridge isolated dc/dc converter for fuel-cell-based applications," *IEEE Transactions on Industry Applications*, vol. 49, no. 4, pp. 1658–1668, July 2013.

[87] B. York, W. Yu, and J. S. Lai, "An integrated boost resonant converter for photovoltaic applications," *IEEE Transactions on Power Electronics*, vol. 28, no. 3, pp. 1199–1207, March 2013.

[88] W. J. Cha, Y. W. Cho, J. M. Kwon, and B. H. Kwon, "Highly efficient microinverter with soft-switching step-up converter and single-switch-modulation inverter," *IEEE Transactions on Industrial Electronics*, vol. 62, no. 6, pp. 3516–3523, June 2015.

[89] M. Kasper, M. Ritz, D. Bortis, and J. W. Kolar, "Pv panel-integrated high step-up high efficiency isolated gan dc-dc boost converter," in *Telecommunications Energy Conference 'Smart Power and Efficiency' (INTELEC), Proceedings of 2013 35th International*, Oct 2013, pp. 1–7.

[90] T. LaBella and J. S. Lai, "A hybrid resonant converter utilizing a bidirectional gan ac switch for high-efficiency pv applications," *IEEE Transactions on Industry Applications*, vol. 50, no. 5, pp. 3468–3475, Sept 2014.

[91] D. Vinnikov, A. Chub, E. Liivik, and I. Roasto, "High-performance quasi-z-source series resonant dc-dc converter for photovoltaic module level power electronics applications," *IEEE Transactions on Power Electronics*, vol. PP, no. 99, pp. 1–1, 2016.

[92] H. Hu, X. Fang, Q. Zhang, Z. J. Shen, and I. Batarseh, "Optimal design considerations for a modified llc converter with wide input voltage range capability suitable for pv

applications," in *2011 IEEE Energy Conversion Congress and Exposition*, Sept 2011, pp. 3096–3103.

[93] Y. J. Kim and J. Y. Lee, "Full-bridge srt hybrid dc/dc converter for a 6.6-kw ev on-board charger," *IEEE Transactions on Vehicular Technology*, vol. 65, no. 6, pp. 4419–4428, June 2016.

[94] Z. Qu, V. Dayal, J. Dong, R. Sangha, N. Shafiei, S. A. Arefifar, M. Ordonez, M. Craciun, and C. Botting, "Comprehensive power mosfet model for llc resonant converter in renewable energy applications," in *2016 IEEE 7th International Symposium on Power Electronics for Distributed Generation Systems (PEDG)*, June 2016, pp. 1–5.

[95] Z. Fang, T. Cai, S. Duan, and C. Chen, "Optimal design methodology for llc resonant converter in battery charging applications based on time-weighted average efficiency," *IEEE Transactions on Power Electronics*, vol. 30, no. 10, pp. 5469–5483, Oct 2015.

[96] N. Harischandrappa and A. K. S. Bhat, "A fixed-frequency lcl -type series resonant converter with a capacitive output filter using a modified gating scheme," *IEEE Transactions on Industry Applications*, vol. 50, no. 6, pp. 4056–4064, Nov 2014.

[97] J. Deng, C. C. Mi, R. Ma, and S. Li, "Design of llc resonant converters based on operation-mode analysis for level two phev battery chargers," *IEEE/ASME Transactions on Mechatronics*, vol. 20, no. 4, pp. 1595–1606, Aug 2015.

[98] Stat-Ease, "Design-expert software version 10," https://www.statease.com/software.html.

[99] D. H. Kim, M. J. Kim, and B. K. Lee, "An integrated battery charger with high power density and efficiency for electric vehicles," *IEEE Transactions on Power Electronics*, vol. 32, no. 6, pp. 4553–4565, June 2017.

[100] C. C. Hua, Y. H. Fang, and C. W. Lin, "Llc resonant converter for electric vehicle battery chargers," *IET Power Electronics*, vol. 9, no. 12, pp. 2369–2376, 2016.

[101] H. Haga and F. Kurokawa, "Modulation method of a full-bridge three-level llc resonant converter for battery charger of electrical vehicles," *IEEE Transactions on Power Electronics*, vol. 32, no. 4, pp. 2498–2507, April 2017.

[102] P. He and A. Khaligh, "Comprehensive analyses and comparison of 1 kw isolated dc-dc converters for bidirectional ev charging systems," *IEEE Transactions on Transportation Electrification*, vol. 3, no. 1, pp. 147–156, March 2017.

[103] H. Choi, "Analysis and design of llc resonant converter with integrated transformer," in *APEC 07 - Twenty-Second Annual IEEE Applied Power Electronics Conference and Exposition*, Feb 2007, pp. 1630–1635.

[104] Fairchild Semiconductor Corporation, "Half-bridge llc resonant converter design using fsfr-series fairchild power switch," 2007, rev. 1.0.0 10/9/07.

[105] W. Flanagan, *Handbook of Transformer Design and Applications*. McGraw-Hil, 1992.

[106] N. Shafiei, M. Pahlevaninezhad, H. Farzanehfard, A. Bakhshai, and P. Jain, "Analysis of a fifth-order resonant converter for high-voltage dc power supplies," *IEEE Transactions on Power Electronics*, vol. 28, no. 1, pp. 85–100, Jan 2013.

[107] H. Wang, M. Shang, and A. Khaligh, "A psfb-based integrated pev onboard charger with extended zvs range and zero duty cycle loss," *IEEE Transactions on Industry Applications*, vol. 53, no. 1, pp. 585–595, Jan 2017.

[108] J. H. Kim, I. O. Lee, and G. W. Moon, "Analysis and design of a hybrid-type converter for optimal conversion efficiency in electric vehicle chargers," *IEEE Transactions on Industrial Electronics*, vol. 64, no. 4, pp. 2789–2800, April 2017.

[109] D. C. Montgomery, *Design and Analysis of Experiments*, 8th Edition, Ed. Wiley, 2001.

[110] S. R. Cove, M. Ordonez, F. Luchino, and J. E. Quaicoe, "Applying response surface methodology to small planar transformer winding design," *IEEE Transactions on Industrial Electronics*, vol. 60, no. 2, pp. 483–493, Feb 2013.

[111] R. Pagano, S. Abedinpour, A. Raciti, and S. Musumeci, "Efficiency optimization of an integrated wireless power transfer system by a genetic algorithm," in *2016 IEEE Applied Power Electronics Conference and Exposition (APEC)*, March 2016, pp. 3669–3676.

[112] I. Batarseh, "Resonant converter topologies with three and four energy storage elements," *IEEE Transactions on Power Electronics*, vol. 9, no. 1, pp. 64–73, Jan 1994.

[113] A. K. S. Bhat, A. Biswas, and B. S. R. Iyengar, "Analysis and design of (lc)(lc)-type series-parallel resonant converter," *IEEE Transactions on Aerospace and Electronic Systems*, vol. 31, no. 3, pp. 1186–1193, Jul 1995.

[114] V. Belaguli and A. K. S. Bhat, "A hybrid resonant converter operated as a low harmonic rectifier with and without active control," *IEEE Transactions on Power Electronics*, vol. 14, no. 4, pp. 730–742, Jul 1999.

[115] A. K. S. Bhat and R. L. Zheng, "Analysis and design of a three-phase lcc-type resonant converter," *IEEE Transactions on Aerospace and Electronic Systems*, vol. 34, no. 2, pp. 508–519, Apr 1998.

[116] V. Belaguli and A. K. S. Bhat, "Series-parallel resonant converter operating in discontinuous current mode. analysis, design, simulation, and experimental results," *IEEE Transactions on Circuits and Systems I: Fundamental Theory and Applications*, vol. 47, no. 4, pp. 433–442, Apr 2000.

[117] Y. A. Ang, C. M. Bingham, M. P. Foster, D. A. Stone, and D. Howe, "Design oriented analysis of fourth-order lclc converters with capacitive output filter," *IEE Proceedings - Electric Power Applications*, vol. 152, no. 2, pp. 310–322, March 2005.

[118] M. Z. Youssef and P. K. Jain, "Series ndash;parallel resonant converter in self-sustained oscillation mode with the high-frequency transformer-leakage-inductance effect: Analysis, modeling, and design," *IEEE Transactions on Industrial Electronics*, vol. 54, no. 3, pp. 1329–1341, June 2007.

[119] K. M. Cho, Y. D. Kim, I. H. Cho, and G. W. Moon, "Transformer integrated with additional resonant inductor for phase-shift full-bridge converter with primary clamping diodes," *IEEE Transactions on Power Electronics*, vol. 27, no. 5, pp. 2405–2414, May 2012.

[120] H. de Groot, E. Janssen, R. Pagano, and K. Schetters, "Design of a 1-mhz llc resonant converter based on a dsp-driven soi half-bridge power mos module," *IEEE Transactions on Power Electronics*, vol. 22, no. 6, pp. 2307–2320, Nov 2007.

[121] M. Vuki, S. M. Bero, and L. Vuki, "The multiresonant converter steady-state analysis based on dominant resonant process," *IEEE Transactions on Power Electronics*, vol. 26, no. 5, pp. 1452–1468, May 2011.

[122] C. M. Bingham, Y. A. Ang, M. P. Foster, and D. A. Stone, "Analysis and control of dual-output lclc resonant converters with significantleakage inductance," *IEEE Transactions on Power Electronics*, vol. 23, no. 4, pp. 1724–1732, July 2008.

[123] D. Bortis, G. Ortiz, J. W. Kolar, and J. Biela, "Design procedure for compact pulse transformers with rectangular pulse shape and fast rise times," *IEEE Transactions on Dielectrics and Electrical Insulation*, vol. 18, no. 4, pp. 1171–1180, August 2011.

[124] T. Hongmei, F. MancillaDavid, K. Ellis, and E. Muljadi, "A detailed performance model for photovoltaic systems," July 2012, national Renewable Energy Laboratory, USA NREL/JA-5500-54601.

[125] G. M. Masters, *Renewable and Efficient Electric Power Systems.* John Wiley and Sons, NY, 2004.

[126] A. D. Rajapakse and D. Muthumuni, "Simulation tools for photovoltaic system grid integration studies," in *Electrical Power Energy Conference (EPEC), 2009 IEEE*, Oct 2009, pp. 1–5.

[127] Canadian Solar Inc., "Max power cs6x-310p," http://www.canadiansolar.com/na/solar-panels/maxpower.html.

[128] M. Saket, N. Shafiei, and M. Ordonez, "Llc converters with planar transformers: Issues and mitigation," *IEEE Transactions on Power Electronics*, vol. PP, no. 99, pp. 1–1, 2016.

[129] S. R. Cove, M. Ordonez, N. Shafiei, and J. Zhu, "Improving wireless power transfer efficiency using hollow windings with track-width-ratio," *IEEE Transactions on Power Electronics*, vol. 31iei, no. 9, pp. 6524–6533, Sept 2016.

[130] M. Mohammadi, N. Shafiei, and M. Ordonez, "Llc synchronous rectification using coordinate modulation," in *2016 IEEE Applied Power Electronics Conference and Exposition (APEC)*, March 2016, pp. 848–853.

[131] M. A. Saket, N. Shafiei, M. Ordonez, M. Craciun, and C. Botting, "Low parasitics planar transformer for llc resonant battery chargers," in *2016 IEEE Applied Power Electronics Conference and Exposition (APEC)*, March 2016, pp. 854–858.

[132] N. Shafiei, M. A. S. Tokaldani, and M. Ordonez, "Time domain analysis of llc resonant converters in boost mode for battery charger applications," 2015 IEEE Energy Conversion Congress and Exposition (ECCE), 2017, Under Review.

[133] Infineon Technologies AG, "Coolmos benefits in both hard and soft switching smps topologies," 2016, www.infineon.com/coolmos.

[134] G. Lakkas, "Mosfet power losses and how they affect power-supply efficiency," Oct. 2016, texas Instruments.

[135] B. Mammano, "Introduction to resonant power conversion," 2001, unitrode Corporation, Texas Instruments.

[136] Vicor Corporation, "High voltage bus converter module," Feb. 2016, vicorpower.com.